Samuel Marko Hörmann, BSc

# Conductive Coatings for Electromagnetic Interference Shielding of a Time of Flight Sensor

**MASTER'S THESIS**

to achieve the university degree of

Diplom-Ingenieur

Master's degree programme: Technical Physics

submitted to

**Graz University of Technology**

**Peter Hadley**

Univ.-Prof. Ph.D.

Institute of Solid State Physics

Graz, July 2021

# AFFIDAVIT

I declare that I have authored this thesis independently, that I have not used other than the declared sources/resources, and that I have explicitly indicated all material which has been quoted either literally or by content from the sources used. The text document uploaded to TUGRAZonline is identical to the present master's thesis.

Date, Signature

# Abstract

In today's society electromagnetic waves are ever-present. Every electronic device unavoidably emits electromagnetic radiation, because any electronic current acts as its source. However, many such building blocks are integrated in a typical application and, therefore, electromagnetic interference (EMI) shielding is frequently used to make them compatible. In this thesis, an alternative to the heavy, large and expensive separate shielding caps was investigated. By coating the lid of a time of flight sensor with a thin metal layer, the emissions measured in a transverse electromagnetic (TEM) cell were reduced by up to 54 % and 71 % in the two orientations of the device respectively.

The high shielding effectiveness (SE) was traced back to its conductivity, which is confirmed by state-of-the-art literature. The effects of apertures and grounding were researched via trials with copper tape and simulations with Ansys HFSS. It was observed that the SE depends crucially on the quality of the electrical connection between the coating and the ground plane in the integrated circuit (IC) of the sensor. Importantly, even with apertures the shielding was successful. Furthermore, it was determined that if the grounding is only partial along one axis, only the TEM cell spectrum of one orientation is attenuated effectively. Multiple materials from dedicated suppliers and a sputtered layer were compared. Their shielding capabilities were tested in transmission line measurements with coated plates and their conductivity was rated by determining the resistance over the lid. A definite ranking of the coated lids via the TEM cell measurements was not possible because the grounding set a lower limit for the spectra. Moreover, the TEM cell measurements were compared to a magnetic dipole source based on the Fourier transform of the vertical cavity surface emitting laser (VCSEL) current. The response of the TEM cell measurement system to a bondwire source was mapped over the frequency range. The coupling was more than 17 times higher for one orientation. Additionally, by jittering the VCSEL current it was concluded that its EMI is only measured in one orientation. These findings indicate that the EMI emitted can be modeled by dipoles in the far field, as developed by Pan et al. [12]. A hypothesis for the shielding mechanism was developed: It was proposed that for the shielding to be effective, a closed current loop with an opposing equivalent dipole moment must possible in the shield.

This work proves the feasibility of the convenient and easily integrateable EMI shielding by a thin deposition film and enables next generation sensors to utilize and improve the established design. Importantly, the grounding must be enhanced by enabling more contacts between the lid and the IC.

# Kurzfassung

In der heutigen Gesellschaft sind elektromagnetische Wellen allgegenwärtig. Jedes elektronische Bauteil emittiert unvermeidlich elektromagnetische Strahlung, da jeder elektrische Strom als Quelle wirkt. In einer typischen Anwendung sind jedoch unzählige solche Komponenten eingebaut und daher wird oftmals auf Abschirmung der elektromagnetischen Interferenz (EMI) zurückgegriffen, um sie untereinander kompatibel zu machen. In dieser Arbeit wurde eine Alternative zu den schweren, großen und teuren Abschirmungsaufsätzen untersucht. Durch das Beschichten des Gehäuses eines TOF (englisch: time of flight) -Sensors mit einem dünnen, metallischen Film wurden die Emissionen, die in einer transversal elektromagnetischen (TEM) Zelle gemessen wurden, um bis zu 54 % und 71 % in den zwei Orientierungen reduziert.

Diese hohe Abschirmungseffektivität (SE, englisch: shielding effectiveness) wurde auf die Leitfähigkeit der Materialien zurückverfolgt. Das wurde durch aktuelle Literatur auch bestätigt. Die Effekte der Aperturen und Erdung wurden über Versuche mit Kupferband und Simulationen mit Ansys HFSS erforscht. Es wurde festgestellt, dass die SE entscheidend von der Qualität der Verbindung zwischen Schild und Erdungsschicht im IC (englisch: integrated circuit) des Sensors abhängt. Ein weiteres zentrales Ergebnis ist, dass die Abschirmung auch mit den offenen Aperturen funktioniert. Weiters wurde beobachtet, dass im Falle einer gerichteten Erdung nur das TEM-Zellenspektrum einer Orientierung effektiv gedämpft wird. Unterschiedliche Materialien von spezialisierten Zulieferern und eine gesputterte Schicht wurden verglichen. Ihre Abschirmungsvermögen wurden durch Tests mit beschichteten Platten in einer Übertragungsleitung charakterisiert und ihre Leitfähigkeiten durch die Messung des elektrischen Widerstandes über das Gehäuse bewertet. Eine endgültige Reihung der beschichteten Teile durch die TEM-Zellenmess- ungen war nicht möglich. Es wurde argumentiert, dass die schlechte Erdung ein unteres Limit in den Spektren verursacht. Außerdem wurden die Messungen in der TEM-Zelle mit einer magnetischen Dipolquelle modelliert, deren Emissionen durch eine Fouriertransformation des VCSEL (englisch: vertical cavity surface emitting laser) -Stroms beschrieben wurden. Das Antwortverhalten des Messsystems der TEM-Zelle auf eine Bondwire-Quelle wurde erfasst. Die Kopplung war in einer Orientierung mehr als 17-mal höher. Zusätzlich wurde durch Modifizieren des VCSEL-Stroms geschlussfolgert, dass die zugehörigen Emissionen zum überwiegenden Teil nur in einer Orientierung gemessen werden. Diese Ergebnisse weisen darauf hin, dass die emittierte EMI durch Dipolstrahler im Fernfeld beschrieben werden können, wie von Pan et al. [12] diskutiert. Eine Hypothese für den Schirmmechanismus wurde entwickelt, in der vorgeschlagen

wurde, dass für eine effektive Abschirmung eine geschlossene Stromschleife mit einem entgegengerichteten äquivalenten Dipolmoment im Schild vorhanden sein muss.

Diese Arbeit beweist die Machbarkeit der Abschirmung von EMI durch eine einfach zu integrierende Beschichtung und ermöglicht die folgende Generation von Sensoren das bestehende Design zu nutzen und zu verbessern. Als Kernpunkt müssen mehr Erdungsverbindungen zwischen dem Gehäuse und dem IC bereitgestellt werden.

# Acknowledgements

First and foremost I want to thank my parents for enabling my studies.
I am also boundlessly grateful to my girlfriend Christina for her unwavering support and for changing her life plans to make our studies in Graz a reality.
I am much obliged to my brother Leander and my sister-in-law Sabine for the council they offered.

This thesis was organized by ams-OSRAM AG. They also provided most of the equipment. I want to thank all the people there who were so generous and helpful. Their experience was invaluable. A special thanks belongs to Martin Faccinelli and Harald Etschmaier who supervised and guided me along the path.
Further, I want to thank David Pommerenke who set up the transmission line experiment at the Institute of Electronics at the Graz University of Technology.
Last, but not least, I want to thank my supervisor Peter Hadley for his unfailingly constructive and purposeful advice.

# Contents

# List of Abbreviations

| Abbreviation | Meaning |
|---|---|
| BW | Bondwire |
| DUT | Device under test |
| EM | Electromagnetic |
| EMC | Electromagnetic compatibility |
| EMI | Electromagnetic interference |
| EMR | Electromagnetic radiation |
| EMW | Electromagnetic waves |
| FFT | Fast Fourier transform |
| LCP | Liquid crystal polymer |
| PCB | Printed circuit board |
| SE | Shielding effectiveness |
| SEM | Scanning electron microscope |
| SPAD | Single photon avalanche diode |
| TEM | Transverse electromagnetic |
| TOF | Time of flight |
| VCSEL | Vertical cavity surface emitting laser |
| VIA | Electrical connection through layers in a PCB |

# Chapter 1

# Introduction

Electromagnetic waves are ever-present in today's society. They enable us to build electronic devices and, therefore, interconnect. Furthermore, these devices need to continuously improve and become smaller in the process. This miniaturization exacts many properties of their building blocks. One of them is electromagnetic compatibility (EMC). Every electronic component unavoidably emits electromagnetic radiation, because any time-varying electronic current creates an electromagnetic field. This may be the desired functionality, but if it is not, it is considered electromagnetic pollution of the part's environment. This is undesirable and if it is not controlled, it may interact with other electronics and hamper or ruin their performance, or even destroy them completely.

Thus, any commercial electronic device must meet two demands: Firstly, its emission must be below a threshold, and secondly, it must be able to function in an environment that is electromagnetically polluted, to a certain level. There are standards for this which are well respected by the electronic industry. Generally, manufacturers aim to reduce the emissions before they become a problem in the later stages of the development to avoid costly product design edits.

The most important part is to design the circuits in such a way, that they emit as little as possible. Therefore, current paths should be short and they should not form a large loop to not be essentially equivalent to an antenna. For critical components with large emissions there are tricks to further reduce them, e.g. split paths or combine different ones to stack loops with opposite current flow directions, which ideally causes their electromagnetic fields to interfere destructively and cancel each other out. But if all of that is not enough, the only way to reduce the emissions further is to apply shielding solutions, on which this thesis focuses.

Conventional shields consist of lids that are made by bending sheet metals and are assembled such that they enclose the device of interest. However, this is an expensive approach and increases the final size of the part. Therefore, in this thesis a shield is investigated that is fabricated by depositing a thin film onto the already existing lid of a multi-zone time of flight (TOF) sensor manufactured by ams-OSRAM AG.

The main advantage of the modification presented in this thesis is that it may be easily and cheaply integrated into the present process of manufacturing almost any kind of package, in case the emissions of a device turn out to be too high in the later stages of the development.

## 1.1 General Framework

The lid of TOF sensor that is investigated in this thesis (TMF8821) is depicted in fig. 1.1. The sensor functions on the principle to measure the time it takes for a pulse that is emitted by a vertical cavity surface emitting laser (VCSEL) and reflected by an object to be detected by a single photon avalanche diode (SPAD) array. The TOF is proportional to its distance. The VCSEL generates infrared light with a wavelength of 940 nm. The pulses are emitted with a frequency of 17.7 MHz and have a width of 400 ps to 500 ps. The package is covered by a lid of liquid crystal polymer (LCP). This is to be coated with a thin film that is shielding the electromagnetic interference (EMI) emitted by the driving currents of the sensor's components. The main culprits are the VCSEL driver, the VCSEL charge pump and the SPAD charge pump, as already determined by ams-OSRAM AG during the design engineering. It is important to clarify that it is not the laser light responsible for the EMI, but the electrical currents. Shielding the laser light would not be possible in any case, since it is essential for the functionality of the device.

It is only purposeful to coat the inside of the lid, because the coating step must be conducted before the assembly of the sensor, after which the outside of the sidewalls are cut off. Naturally, there is nothing that opposes the outside of the top side to be coated too, but it is disputable whether this achieves enough shielding to justify the additional coating step. Therefore, the green, hatched areas show the designated areas to be coated. The coating is electrically connected to the ground of the sensor's integrated circuit (IC) at the areas indicated yellow. However, the ground in the IC is split into two separate parts, which each connect to one of the yellow areas on one side and to one ground pin on the other side. In order to facilitate the connection, the deposited film there is left bare, since most coatings are sealed with a resist to eliminate deterioration due to oxidation. The lid is glued onto the substrate via a conductive adhesive that in turn enables the metallic film on the lid to connect to the IC's pads at the yellow areas. A cross section of the sensor and the resulting electrical diagram is shown in fig. 2.3.

The dimensions of the lid are $4.60 \times 2.00 \times 1.18$ mm after cutting. The apertures measure approximately $1 \times 1$ mm. The dimensions stipulate that the coating on the side walls must be below 15 µm such that the sensor can still be assembled.

Typical compliance tests for EMC of sensors like this are conducted in a transverse electromagnetic cell (TEM cell) and this method shall also be used for the main quantification in this work.

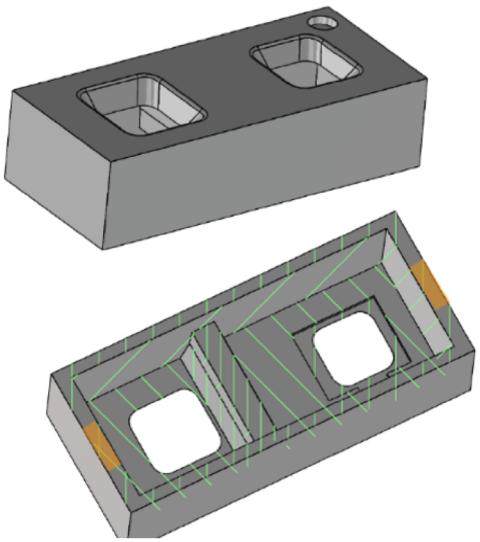

**Figure 1.1:** LCP lid of the time of flight sensor whose electromagnetic interference is to be shielded. The green, hatched areas are designated to be coated and the yellow ones are electrical connections for grounding the deposited film.

## 1.2 Electromagnetic Waves

Electromagnetic waves (EMW) are a physical process by which energy of electromagnetic radiation (EMR or light) is transported through space. By nature, these waves oscillate at a certain frequency. It enables us to classify different wave regimes, ranging from radio waves and microwaves over visible light to gamma rays. As can be seen from these examples, while the waves always act the same, matter reacts very differently, depending on which frequency is irradiated onto it. The frequency of EMI usually ranges no higher than several GHz and thus it classifies as radio or microwaves. The theory in this chapter largely relies on the book *Electromagnetic Waves and Antennas* by Orfanidis [11].

### 1.2.1 Maxwell's Equations

Classical electromagnetism is completely described by Maxwell's equations:

$$\boldsymbol{\nabla} \cdot \boldsymbol{E} = \frac{\rho_{tot}}{\epsilon_0} \tag{1.1a}$$

$$\boldsymbol{\nabla} \cdot \boldsymbol{B} = 0 \tag{1.1b}$$

$$\boldsymbol{\nabla} \times \boldsymbol{E} = -\frac{\partial \boldsymbol{B}}{\partial t} \tag{1.1c}$$

$$\boldsymbol{\nabla} \times \boldsymbol{B} = \mu_0 \boldsymbol{J_{tot}} + \mu_0 \epsilon_0 \frac{\partial \boldsymbol{E}}{\partial t} \tag{1.1d}$$

Here $\boldsymbol{E}$ is the electric field strength, $\boldsymbol{B}$ the magnetic flux density, $\rho_{tot}$ the total electric charge density, $\boldsymbol{J_{tot}}$ the total electric current density, $\epsilon_0$ the vacuum permittivity and $\mu_0$ the vacuum permeability. In accordance to the standard

notation bold symbols signify vectorial quantities in this thesis and the non-bold form of the same symbol means its euclidean norm. In the presence of EMW matter gets electrically and magnetically polarized. Linear, homogeneous and isotropic matter can be described by

$$\boldsymbol{P} = \epsilon_0 \chi_E \boldsymbol{E} \tag{1.2a}$$
$$\boldsymbol{M} = \chi_M \boldsymbol{H} \tag{1.2b}$$
$$\boldsymbol{D} = \epsilon_0 \boldsymbol{E} + \boldsymbol{P} = \epsilon_0 (1 + \chi_E) \boldsymbol{E} = \epsilon_0 \epsilon_r \boldsymbol{E} = \epsilon \boldsymbol{E} \tag{1.2c}$$
$$\boldsymbol{B} = \mu_0 (\boldsymbol{H} + \boldsymbol{M}) = \mu_0 (1 + \chi_M) \boldsymbol{H} = \mu_0 \mu_r \boldsymbol{H} = \mu \boldsymbol{H} \tag{1.2d}$$

where $\boldsymbol{P}$ is the electric polarization, $\boldsymbol{M}$ the magnetization, $\chi_E$ and $\chi_M$ the respective susceptibilities. We have also defined the electric flux density $\boldsymbol{D}$ and the magnetic field strength $\boldsymbol{H}$. $\epsilon_r$, $\epsilon$, $\mu_r$ and $\mu$ are the relative permittivity, permittivity, relative permeability and permeability respectively. $\chi_E$, $\epsilon_r$ or $\epsilon$ describe the materials electric behavior and $\chi_M$, $\mu_r$ or $\mu$ its magnetic behavior.

In this sense, the Maxwell's equations may be reformulated:

$$\boldsymbol{\nabla} \cdot \boldsymbol{D} = \rho \tag{1.3a}$$
$$\boldsymbol{\nabla} \cdot \boldsymbol{B} = 0 \tag{1.3b}$$
$$\boldsymbol{\nabla} \times \boldsymbol{E} = -\frac{\partial \boldsymbol{B}}{\partial t} \tag{1.3c}$$
$$\boldsymbol{\nabla} \times \boldsymbol{H} = \boldsymbol{J} + \frac{\partial \boldsymbol{D}}{\partial t} \tag{1.3d}$$

$\rho$ is the external or free charge density and $\boldsymbol{J}$ is the external or free current density. This just means that they don't include the bound charges (polarization charges) and currents (polarization currents).

$\epsilon$ and $\mu$ are macroscopic descriptions of the matter, i.e. they describe the average spacial response of a unit volume of the material. However, how this response actually comes to be, is not described. The interested reader is referred to the Ewald–Oseen extinction theorem, e.g. found in [11].

### Wave Equation in Vacuum

In the absence of sources, i.e. $\rho = J = 0$ the Maxwell's equations take on the form

$$\boldsymbol{\nabla} \cdot \boldsymbol{E} = 0 \tag{1.4a}$$
$$\boldsymbol{\nabla} \cdot \boldsymbol{B} = 0 \tag{1.4b}$$
$$\boldsymbol{\nabla} \times \boldsymbol{E} = -\frac{\partial \boldsymbol{B}}{\partial t} \tag{1.4c}$$
$$\boldsymbol{\nabla} \times \boldsymbol{B} = \mu_0 \epsilon_0 \frac{\partial \boldsymbol{E}}{\partial t} \tag{1.4d}$$

which are symmetric. That there are no sources basically means empty space or vacuum. Thus, $\boldsymbol{D} = \epsilon_0 \boldsymbol{E}$ and $\boldsymbol{B} = \mu_0 \boldsymbol{H}$. Applying $\boldsymbol{\nabla}\times$ to eqs. (1.4c) and (1.4d) and using the equality $\boldsymbol{\nabla} \times \boldsymbol{\nabla} \times \boldsymbol{V} = \boldsymbol{\nabla}(\boldsymbol{\nabla} \cdot \boldsymbol{V}) - \nabla^2 \boldsymbol{V}$ for an

arbitrary, differentiable vector field $\boldsymbol{V}$ allows us to insert eqs. (1.4a) and (1.4b), which yields the uncoupled wave equations

$$\nabla^2 \boldsymbol{E} = \mu_0 \epsilon_0 \frac{\partial^2 \boldsymbol{E}}{\partial t^2} \tag{1.5a}$$

$$\nabla^2 \boldsymbol{B} = \mu_0 \epsilon_0 \frac{\partial^2 \boldsymbol{B}}{\partial t^2} \tag{1.5b}$$

This justifies the name electromagnetic waves. Of course, this particular derivation is only valid in empty space, but we will soon see that an effort can be made also in matter that results in wave equations for the field quantities.

#### Power

The power transported by an electromagnetic field is described by the Poynting vector:

$$\boldsymbol{P} = \boldsymbol{E} \times \boldsymbol{H} \tag{1.6}$$

#### Harmonic Time Dependence

The four electromagnetic field quantities are variables of space and time, i.e. (exemplary conducted with the D-field):

$$\boldsymbol{D} = \boldsymbol{D}(\boldsymbol{r}, t)$$

In a first step we assume harmonic time dependence with the angular frequency $\omega$:

$$\boldsymbol{D}(\boldsymbol{r}, t) = \boldsymbol{D}(\boldsymbol{r}) \mathrm{e}^{\mathrm{i}\omega t} \tag{1.7}$$

Note that this is defining a sign convention. Sometimes the time dependence is defined with a minus sign in the exponent, changing the sign of the imaginary part of $\epsilon$, $\mu$ and similarly derived quantities. Doing this for all field quantities, inserting them into the Maxwell's equations (eq. (1.3)) and executing the derivatives yields:

$$\boldsymbol{\nabla} \cdot \boldsymbol{D} = \rho \tag{1.8a}$$

$$\boldsymbol{\nabla} \cdot \boldsymbol{B} = 0 \tag{1.8b}$$

$$\boldsymbol{\nabla} \times \boldsymbol{E} = -\mathrm{i}\omega \boldsymbol{B} \tag{1.8c}$$

$$\boldsymbol{\nabla} \times \boldsymbol{H} = \boldsymbol{J} + \mathrm{i}\omega \boldsymbol{D} \tag{1.8d}$$

### 1.2.2 Models of Real Media

In the above description of the polarization and magnetization the argument has not been specified implying $\boldsymbol{D}(\boldsymbol{r}, t) = \epsilon \boldsymbol{E}(\boldsymbol{r}, t)$ and $\boldsymbol{B}(\boldsymbol{r}, t) = \mu \boldsymbol{H}(\boldsymbol{r}, t)$ with $\epsilon$ and $\mu$ being constants. But that is not the case for real media. The

reason being that the polarization and magnetization cannot response *instantaneously* to the field quantities that create them. To take this into account we have to use the convolutional and causally constitutive relationship

$$\boldsymbol{D}(\boldsymbol{r},t) = \int_{-\infty}^{t} \epsilon(t-t')\boldsymbol{E}(\boldsymbol{r},t')dt' \tag{1.9}$$

i.e. we have to consider that all previous values of the field affects the polarization and thus the flux at the current time. We can do this by specifying that $\epsilon$ is a function of time. The eq. (1.9) may be inspected in a much easier way by transforming it into the frequency domain via a Fourier transform (with the definition given in eq. (A.1)), which yields (for the derivation refer to eq. (A.2)):

$$\boldsymbol{D}(\boldsymbol{r},\omega) = \epsilon(\omega)\boldsymbol{E}(\boldsymbol{r},\omega) \tag{1.10}$$

We can see that the electric flux may then be calculated like we wrote in the first place, i.e. by a simple multiplication. However, $\epsilon$ is now frequency dependent. A medium that exhibits this property is called *dispersive*. An analogue relationship can be computed for the magnetic flux.

### Drude Metal

A simple model for a metal can be formulated by specifying a differential equation for the conduction electrons. In the Drude model the electrons are assumed to behave classically and unbound, i.e. there is no force that strives to drive them back to their atoms, which is an appropriate model for a metal:

$$m_e \frac{\partial v(\boldsymbol{r},t)}{\partial t} = -\frac{m_e}{\tau} v(\boldsymbol{r},t) - eE(\boldsymbol{r},t) \tag{1.11}$$

The electrons with mass $m_e$, charge $e$ and drift velocity $v$ are driven by the electric field. Thus, they are accelerated until their drift velocity becomes so high that the dampening term, which is characterized by the average scattering time $\tau$, balances the force due to the E-field. We are only interested in the norm of the vectorial quantities involved.

Several material parameters including their frequency dependency may then be calculated based on this differential equation by inserting the harmonic time dependence and we use this model to evaluate the conductivity $\sigma$ by substituting the drift velocity by the current density

$$\boldsymbol{J}(\boldsymbol{r},t) = -ne\boldsymbol{v}(\boldsymbol{r},t) \tag{1.12}$$

with electron density $n$. Inserting the harmonic time dependence of the E-field, we also know our solution must also be harmonic with the same frequency. The equation thus becomes

$$-\frac{m_e}{ne}\frac{d}{dt}\left[J(\boldsymbol{r})e^{\mathrm{i}\omega t}\right] = \frac{m_e}{ne\tau}J(\boldsymbol{r})e^{\mathrm{i}\omega t} - eE(\boldsymbol{r})e^{\mathrm{i}\omega t} \tag{1.13}$$

After differentiating, the exponentials cancel and we rearrange:

$$\frac{m_e}{ne\tau}\left(1+\mathrm{i}\omega\tau\right)J(\boldsymbol{r}) = eE(\boldsymbol{r})$$

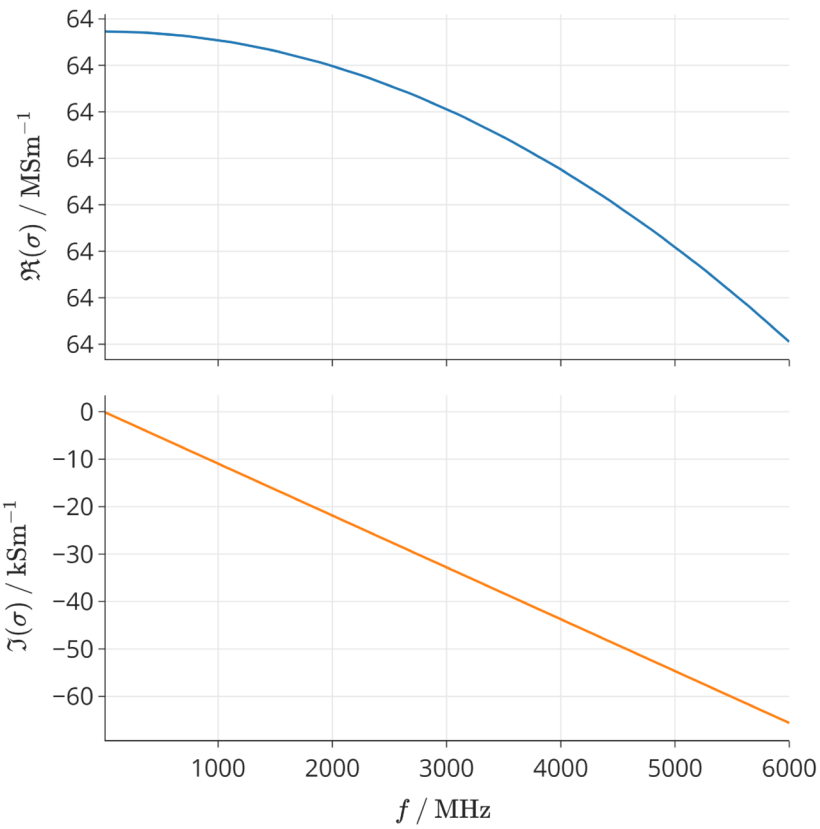


**Figure 1.2:** Complex and frequency dependent conductivity for copper ($\tau = 2.7 \times 10^{-14}\,\mathrm{s}$, $n = 8.47 \times 10^{28}\,\mathrm{m}^{-3}$) calculated according to eq. (1.15).

where we see that the quantities are frequency dependent. The conductivity in a metal is assumed to follow Ohm's law:

$$\sigma(\omega) = \frac{\boldsymbol{J}(\boldsymbol{r}, \omega)}{\boldsymbol{E}(\boldsymbol{r}, \omega)} \tag{1.14}$$

which leads to:

$$\sigma(\omega) = \frac{ne^2\tau}{m_e} \frac{1 - \mathrm{i}\tau\omega}{1 + (\tau\omega)^2} = \sigma_0 \frac{1 - \mathrm{i}\tau\omega}{1 + (\tau\omega)^2} \tag{1.15}$$

with the DC-conductivity $\sigma_0 = ne^2\tau/m_e = ne\mu$ that is connected to the electron mobility $\mu$. The conductivity for copper was computed with typical values and is depicted in fig. 1.2. It can be observed that the conductivity is approximately real and constant, i.e. identical to $\sigma_0$, in this range. This approximation is valid for $\omega \ll \tau^{-1}$, which is approximately $\omega \ll 3.7 \times 10^{13}\,\mathrm{Hz}$ for copper.

### 1.2.3 Plane Waves

Plane waves are the most simple form of waves and generally defined as

$$A(\boldsymbol{r}, t) = F(\boldsymbol{n} \cdot \boldsymbol{r} - ct) + G(\boldsymbol{n} \cdot \boldsymbol{r} + ct) \tag{1.16}$$

where $F$ propagates with velocity $c$ in the direction $\boldsymbol{n}$ and $G$ in the opposite direction. We call $F$ the forward-traveling wave and $G$ the backward-traveling

wave. Any differentiable function like this fulfills the wave equation. Due to its linearity we can decompose the general form into a superposition of *harmonic plane waves* by singling out the spectral components of frequency $\omega$ that each are solutions as well:

$$A(\boldsymbol{r}, t) = Ae^{\mathrm{i}(\omega t \mp \boldsymbol{k}\cdot\boldsymbol{r})} \tag{1.17}$$

with the wave vector $\boldsymbol{k}$ and amplitude $A$. The measure that remains is to find the values $\boldsymbol{k}$ that solve the wave equations.

For the moment we assume an infinite, and as before, a linear, homogeneous and isotropic medium. We may then reformulate Maxwell's equations once again for one harmonic plane wave by replacing $\boldsymbol{\nabla}$ with $\mp\mathrm{i}\boldsymbol{k}$ for the forward- and backward-traveling wave respectively and we also use Ohm's law to eliminate the current:

$$\mp\mathrm{i}\boldsymbol{k}\cdot\boldsymbol{D} = \rho \tag{1.18a}$$
$$\mp\mathrm{i}\boldsymbol{k}\cdot\boldsymbol{B} = 0 \tag{1.18b}$$
$$\mp\mathrm{i}\boldsymbol{k}\times\boldsymbol{E} = -\mathrm{i}\omega\boldsymbol{B} \tag{1.18c}$$
$$\mp\mathrm{i}\boldsymbol{k}\times\boldsymbol{H} = \sigma(\omega)\boldsymbol{E} + \mathrm{i}\omega\boldsymbol{D} \tag{1.18d}$$

As long as we don't add any superficial charges into the metal, the free charge density can be set to zero in the above version of the Maxwell's equations. Therefore, we almost have them in a symmetrical form again if it wasn't for the conductivity's term. We could then, once more, transform them into wave equations. Consequentially, we make the ansatz to substitute the E-field back in place of the D-field, allowing us to factor it out in the last equation:

$$\mp\mathrm{i}\boldsymbol{k}\times\boldsymbol{H} = \left[\sigma(\omega) + \mathrm{i}\omega\epsilon(\omega)\right]\boldsymbol{E} \tag{1.19}$$

We introduce a new *total permittivity*

$$\epsilon_{tot}(\omega) = \epsilon(\omega) - \mathrm{i}\frac{\sigma(\omega)}{\omega} \tag{1.20}$$

that casts eq. (1.18d) into the same shape as for vacuum:

$$\mp\mathrm{i}\boldsymbol{k}\times\boldsymbol{H} = \mathrm{i}\omega\epsilon_{tot}(\omega)\boldsymbol{E} \tag{1.21}$$

To get the allowed values for $\boldsymbol{k}$ we multiply with $\mathrm{i}\boldsymbol{k}\times$ and insert eq. (1.18c):

$$\mp\mathrm{i}\boldsymbol{k}\times(\mathrm{i}\boldsymbol{k}\times\boldsymbol{H}) = \mp k^2\boldsymbol{H} = \mathrm{i}\omega\epsilon_{tot}\mathrm{i}\boldsymbol{k}\times\boldsymbol{E} = \mathrm{i}\omega\epsilon_{tot}\left(\pm\mathrm{i}\omega\boldsymbol{B}\right) = \mp\omega^2\epsilon_{tot}\mu\boldsymbol{H} \tag{1.22}$$

$\mp\boldsymbol{H}$ cancels and we see that

$$k(\omega) = \omega\sqrt{\epsilon_{tot}(\omega)\mu(\omega)} \tag{1.23}$$

which is fully determined by the material properties. Therefore, $k$ itself is one. We see that it is both directly and indirectly depending on the frequency. This relationship between $k$ and $\omega$ is called the *dispersion relation*, which also applies to visible light and optics where, depending on the medium, one has different expressions for $\mu, \epsilon_{tot}$. It fully dictates how harmonic plane waves behave in the presence of matter. However, any wave can be decomposed into

harmonic plane waves, therefore it is the only material property of relevance when it comes to electromagnetism, since it encompasses several effects, as we will see in the following section.

From eq. (1.22) we also can deduce the relation which reverses eq. (1.21):

$$\boldsymbol{H} = \pm\frac{1}{\mu(\omega)\omega}\boldsymbol{k}(\omega)\times\boldsymbol{E} = \pm\sqrt{\frac{\epsilon_{tot}(\omega)}{\mu(\omega)}}\hat{\boldsymbol{k}}\times\boldsymbol{E} \tag{1.24}$$

where $\hat{\boldsymbol{k}}$ is the normalized wave vector and simply points into the direction of propagation.

Knowing eq. (1.17) and eq. (1.24) we can fully define a harmonic plane wave in terms of its forward- and backward-traveling components

$$\boldsymbol{E}(\boldsymbol{r}) = \boldsymbol{E}_+(\boldsymbol{r}) + \boldsymbol{E}_-(\boldsymbol{r}) = \boldsymbol{E_{0+}}(\omega)e^{-\mathrm{i}\boldsymbol{k}\cdot\boldsymbol{r}} + \boldsymbol{E_{0-}}(\omega)e^{\mathrm{i}\boldsymbol{k}\cdot\boldsymbol{r}} \tag{1.25a}$$

$$\begin{aligned}\boldsymbol{H}(\boldsymbol{r}) &= \boldsymbol{H}_+(\boldsymbol{r}) + \boldsymbol{H}_-(\boldsymbol{r})\\ &= \sqrt{\frac{\epsilon_{tot}(\omega)}{\mu(\omega)}}\hat{\boldsymbol{k}}\times\left[\boldsymbol{E_{0+}}(\omega)e^{-\mathrm{i}\boldsymbol{k}\cdot\boldsymbol{r}} - \boldsymbol{E_{0-}}(\omega)e^{\mathrm{i}\boldsymbol{k}\cdot\boldsymbol{r}}\right]\end{aligned} \tag{1.25b}$$

by specifying their amplitudes $\boldsymbol{E_{0+}}$ and $\boldsymbol{E_{0-}}$ respectively, the wave vector $\boldsymbol{k}$ and the material properties. In this equation it is instructive to write the position argument explicitly.

An alternative formalism may be applied where in addition to $k$ we use $\eta = \sqrt{\frac{\mu}{\epsilon_{tot}}}$ to fully eliminate $\mu, \epsilon_{tot}$ in eqs. (1.18c) and (1.18d). $\eta$ is often referred to as the fraction between the electric and magnetic fields. This is to be understood as the fraction between their vector norms. However, this is only true if there is either a forward- or a backward-traveling wave alone and not for a superposition as we can see from eq. (1.25)

$$\|\boldsymbol{H}\| = \|\boldsymbol{H_{0\pm}}\| = \left\|\pm\frac{1}{\eta}\hat{\boldsymbol{k}}\times\boldsymbol{E_{0\pm}}\right\| = \frac{1}{\eta}\|\boldsymbol{E_{0\pm}}\| = \frac{1}{\eta}\|\boldsymbol{E}\| \tag{1.26a}$$

$$\begin{aligned}\|\boldsymbol{H}\| = \|\boldsymbol{H_{0+}} + \boldsymbol{H_{0-}}\| &= \left\|\frac{1}{\eta}\hat{\boldsymbol{k}}\times(\boldsymbol{E_{0+}} - \boldsymbol{E_{0-}})\right\|\\ &\neq \frac{1}{\eta}\|\boldsymbol{E_{0+}} + \boldsymbol{E_{0-}}\| = \frac{1}{\eta}\|\boldsymbol{E}\|\end{aligned} \tag{1.26b}$$

because of the minus sign. On the other hand, if only the incident wave is given this can be used to calculate the corresponding forward- or backward-traveling H-wave from the E-field.

In summary, we have the set of material parameters and equations that allow us to calculate the wave vector and the corresponding harmonic plane waves for the electric and the magnetic fields, where in favor of compactness we omitted writing the frequency argument explicitly:

$$\boxed{\begin{aligned} k &= \omega\sqrt{\epsilon_{tot}\mu} && \text{(1.27a)}\\ \eta &= \sqrt{\frac{\mu}{\epsilon_{tot}}} && \text{(1.27b)}\\ \boldsymbol{E}(\boldsymbol{r}) &= \boldsymbol{E_{0+}}\boldsymbol{e}^{-\mathrm{i}\boldsymbol{k}\cdot\boldsymbol{r}} + \boldsymbol{E_{0-}}\boldsymbol{e}^{\mathrm{i}\boldsymbol{k}\cdot\boldsymbol{r}} && \text{(1.27c)}\\ \boldsymbol{H}(\boldsymbol{r}) &= \frac{1}{\eta}\hat{\boldsymbol{k}} \times \left[\boldsymbol{E_{0+}}\boldsymbol{e}^{-\mathrm{i}\boldsymbol{k}\cdot\boldsymbol{r}} - \boldsymbol{E_{0-}}\boldsymbol{e}^{\mathrm{i}\boldsymbol{k}\cdot\boldsymbol{r}}\right] && \text{(1.27d)} \end{aligned}}$$

**Approximation for non-magnetic, good conductors**

For non-magnetic materials $\mu(\omega) \approx \mu_0$. Additionally, in good conductors, e.g. typical metals, the conductivity's contribution predominates over the permittivity's and, since it is approximately $\sigma(\omega) \approx \sigma_0$, $\epsilon_{tot}(\omega) \approx -\mathrm{i}\frac{\sigma_0}{\omega}$ is a good approximation and it follows that

$$k(\omega) \approx \omega\sqrt{-\mathrm{i}\frac{\sigma_0}{\omega}\mu_0} = \sqrt{\frac{\mu_0\sigma_0\omega}{2}}(1-\mathrm{i}) \tag{1.28}$$

### 1.2.4 Absorption, Reflection and Transmission

Inspecting the spacial term $A(\boldsymbol{r}) = Ae^{-\mathrm{i}\boldsymbol{k}\cdot\boldsymbol{r}}$ of a harmonic plane wave we can conclude many effects from the wave vector. For simplification and without loss of generality we assume that the wave travels through the origin, such that $A(\boldsymbol{r}) = Ae^{-\mathrm{i}kr}$. As we have seen, $k$ can become complex. Materials that have such an imaginary wave vector are called *lossy*, because the imaginary part is responsible for *absorption* of electromagnetic power: With

$$k(\omega) = \beta(\omega) - \mathrm{i}\alpha(\omega) \tag{1.29}$$

it follows that

$$A(\boldsymbol{r}) = Ae^{-\mathrm{i}kr} = Ae^{-\alpha r}e^{-\mathrm{i}\beta r} \tag{1.30}$$

and the amplitude of the wave decays exponentially with the traveled distance as quantified by $\alpha$. Expressing the inverse $\delta = \alpha^{-1}$ we have a measure for the distance after which the wave's amplitude decayed to the fraction $1/e \approx 36.8\,\%$ and it is named *skin depth*. $\beta$ describes the non-lossy behavior of the material. Investigating eq. (1.28) we recognize that

$$\delta = \frac{1}{\alpha} = \frac{1}{\beta} = \sqrt{\frac{2}{\mu_0\sigma_0\omega}} \tag{1.31}$$

This leads to a skin depth that drops off with the square root of the frequency as can be seen in fig. 1.3. Using this, eq. (1.31) may be simplified:

$$k = \frac{1}{\delta}(1-\mathrm{i}) \tag{1.32}$$

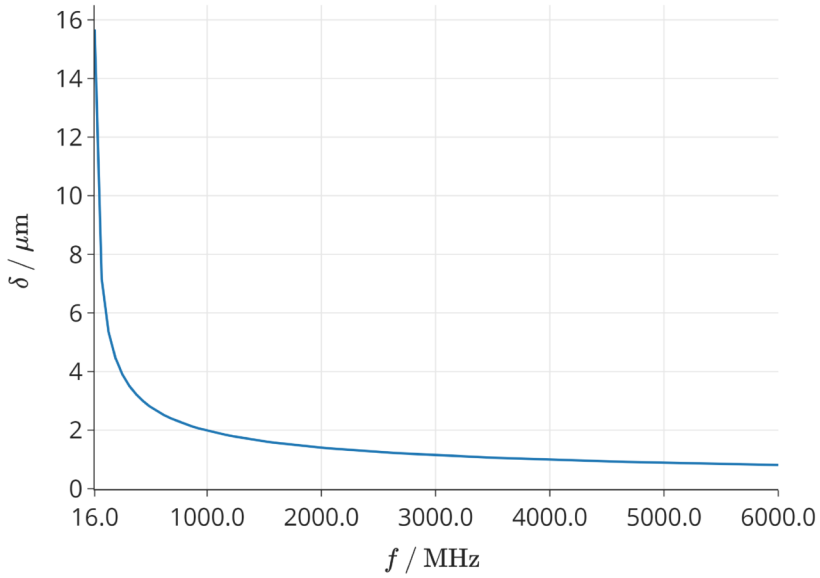


**Figure 1.3:** Skin depth for copper ($\tau = 2.7 \times 10^{-14}\,\mathrm{s}$, $n = 8.47 \times 10^{28}\,\mathrm{m}^{-3}$) calculated according to eq. (1.31).

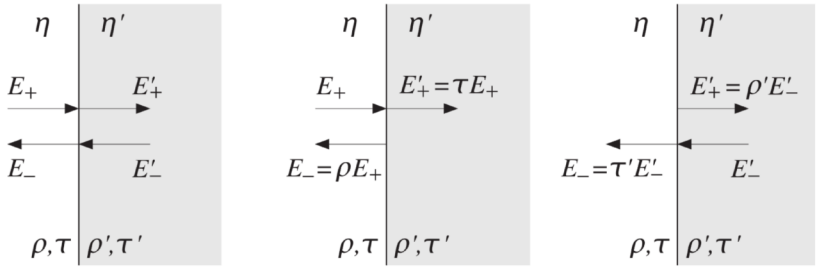


**Figure 1.4:** Electric fields at a planar interface of two optically different materials. Taken from [11].

### Interfaces

At an interface between two optically different materials the wave vector changes abruptly. This has the effect that a part of the electromagnetic power is reflected and the rest is transmitted from the first medium into the second. This leads to the potential complication that at both sides of the interface there are three fields present (incident, reflected and transmitted), because there could be an incident wave from both sides, and the total field is a superposition (see fig. 1.4). To correctly match the electric fields at both sides of a planar interface, there are rules for the perpendicular and parallel (with respect to the interface) components of the electric and magnetic field that can be derived from the Maxwell's equations. A detailed description may be found in [6, 11].

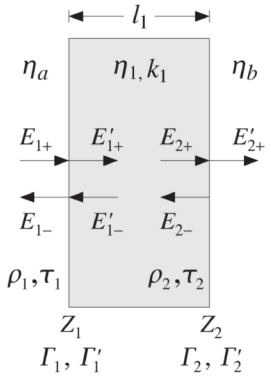


**Figure 1.5:** Electric fields at a planar slab of material. Taken from [11].

### Slab

In our context, however, the interesting geometry is a slab of material with a finite thickness into which an electromagnetic field is irradiated from one side. Because there are two interfaces reflection occurs an infinite number of times. With the approach in [11] this can be included fundamentally and need not be considered separately. The resulting equations allow us to calculate the fields, but here to be able to compute the fraction of transmitted, reflected and absorbed power w.r.t. the incident power is sufficient:

$$\eta_a = \eta_b = \sqrt{\frac{\mu_0}{\epsilon_0}} \qquad \eta_1 = \sqrt{\frac{\mu}{\epsilon_{tot}}} \tag{1.33a}$$

$$\rho_1 = \frac{\eta_1 - \eta_a}{\eta_1 + \eta_a} \qquad \rho_2 = \frac{\eta_b - \eta_1}{\eta_b + \eta_1} \tag{1.33b}$$

$$\tau_1 = 1 + \rho_1 \qquad \tau_2 = 1 + \rho_2 \tag{1.33c}$$

$$T_{slab} = \frac{\tau_1 \tau_2 e^{-\mathrm{i}kl}}{1 + \rho_1 \rho_2 e^{-2\mathrm{i}kl}} \qquad \Gamma_{slab} = \frac{\rho_1 + \rho_2 e^{-\mathrm{i}kl}}{1 + \rho_1 \rho_2 e^{-2\mathrm{i}kl}} \tag{1.33d}$$

$$\frac{P_t}{P_{in}} = |T_{slab}|^2 \qquad \frac{P_r}{P_{in}} = |\Gamma_{slab}|^2 \tag{1.33e}$$

$$\frac{P_a}{P_{in}} = 1 - |T_{slab}|^2 - |\Gamma_{slab}|^2 \tag{1.33f}$$

The variables are named in accordance with fig. 1.5. $\rho_i$ and $\tau_i$ relate to the amount that is reflected and transmitted respectively at the interface $i$, while $T_{slab}$ and $\Gamma_{slab}$ encompass the whole slab.

### Polarization and Oblique Incidence

If the plane waves are incident with an angle that is not 90° with respect to the surface, i.e. oblique, the field solutions further depend on the polarization.

### 1.2.5 Near- and Far-Field

So far we have exclusively talked about plane waves, however, EMR may only be treated as such if the observation point is sufficiently distant from the source. If it is not, this approximation is not justified. We speak of the *near-field*, *far-field* and the *Fresnel-field*. The latter is the transition region in between. Conditions may be stated to distinguish the far-field [11]:

$$r \gg l \qquad \text{and} \qquad r \gg \lambda \tag{1.34}$$

with $r, l, \lambda$ being the observation point, characteristic length scale of the source and the wavelength respectively. In the context of this thesis, $r$ is in the order of cm, $l$ mm and the source's fundamental frequency is 17.7 MHz which corresponds to a wavelength of 16.9 m in air. It is therefore obvious that we may not make the convenient approximations of the far-field and we need to consider the characteristics of the source.

The source of interest in our case is an electric circuit (current loop) of intricate geometry that supplies the current to the time of flight sensor in pulses. The time domain property is therefore obvious, but may be mapped into the frequency domain by viewing the pulse's Fourier transform. After eliminating this issue, the current loop can be crudely approximated by a harmonically oscillating magnetic dipole, or rather a superposition thereof. Hence, a model for the EMI of the IC may be formed. This was conducted in chapter 5.

Arnoldus and Berg investigated dipole radiation and its energy transport in the near-field of an electric dipole in the proximity of a layer of material in [1]. They found solutions of the fields as an integral representation for each point in space. For this purpose, the dipole field was decomposed into a superposition of plane waves via Weyl's representation. Computation and theory, therefore, are quite involved, even for this basic geometry, and from this it may be concluded that the better approach is to simulate the fields. I used the software Ansys HFSS (see chapter 4).

### 1.2.6 Dipole and Multipole Radiation

Orfanidis [11] derived a description of the full fields caused by an oscillating electric dipole with its moment $\boldsymbol{p}$

$$\boldsymbol{E}(\boldsymbol{r}) = \frac{1}{\epsilon_0}\left(\mathrm{i}k + \frac{1}{r}\right)\left[\frac{3\hat{\boldsymbol{r}}(\hat{\boldsymbol{r}}\cdot\boldsymbol{p}) - \boldsymbol{p}}{r}\right] G(\boldsymbol{r}) + \frac{k^2}{\epsilon_0}\hat{\boldsymbol{r}}\times(\boldsymbol{p}\times\hat{\boldsymbol{r}})\, G(\boldsymbol{r}) \tag{1.35a}$$

$$\boldsymbol{H}(\boldsymbol{r}) = \mathrm{i}\omega\left(\mathrm{i}k + \frac{1}{r}\right)(\boldsymbol{p}\times\hat{\boldsymbol{r}})\, G(\boldsymbol{r}) \tag{1.35b}$$

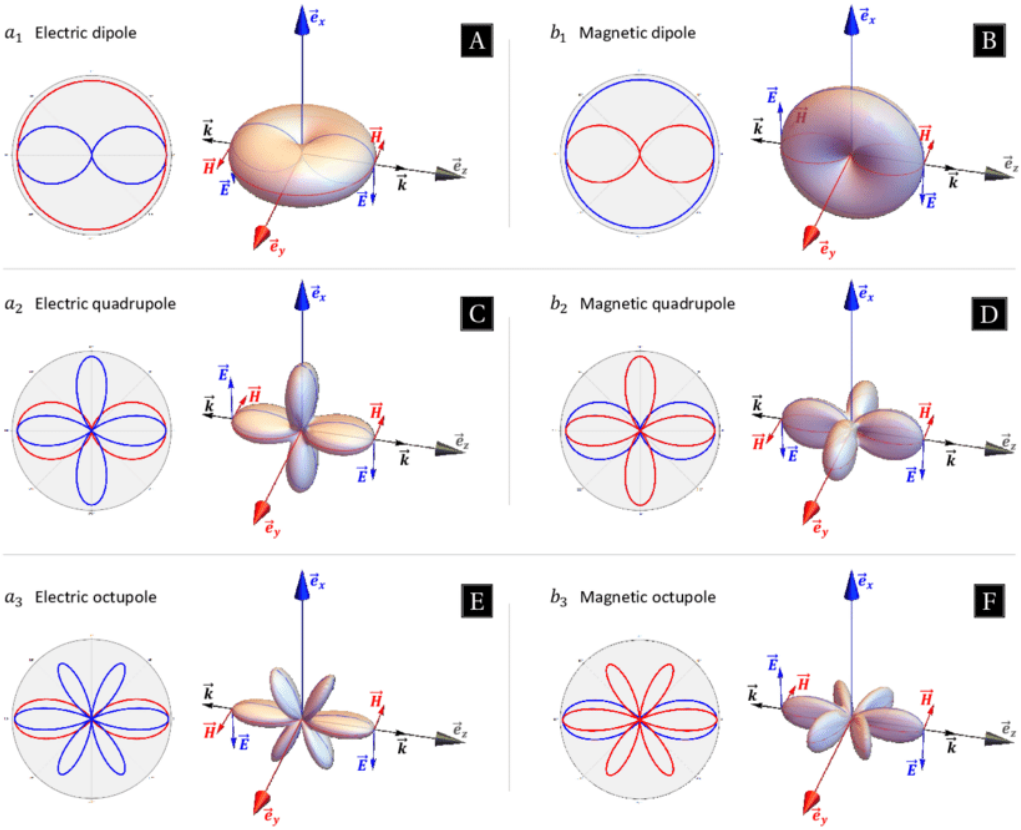


**Figure 1.6:** Radiation pattern and far field magnitudes of a dipole, quadrupole and octopole. Taken from [4].

and by a magnetic dipole with its moment $\boldsymbol{m}$

$$\boldsymbol{E}(\boldsymbol{r}) = \mathrm{i}\omega\mu_0 \left(\mathrm{i}k + \frac{1}{r}\right)(\hat{\boldsymbol{r}} \times \boldsymbol{m})\, G(\boldsymbol{r}) \tag{1.36a}$$

$$\boldsymbol{H}(\boldsymbol{r}) = \left(\mathrm{i}k + \frac{1}{r}\right)\left[\frac{3\hat{\boldsymbol{r}}(\hat{\boldsymbol{r}} \cdot \boldsymbol{m}) - \boldsymbol{m}}{r}\right] G(\boldsymbol{r}) + k^2 \hat{\boldsymbol{r}} \times (\boldsymbol{m} \times \hat{\boldsymbol{r}})\, G(\boldsymbol{r}) \tag{1.36b}$$

where $G$ is their Green's function

$$G(\boldsymbol{r}) = \frac{e^{-\mathrm{i}kr}}{4\pi r} \tag{1.37}$$

These equations include the near and far fields. The latter are characterized by their $\frac{1}{r}$ dependence.

The radiation pattern, i.e. the intensity of the far field components, can be calculated by averaging the magnitude of their Poynting vector over one oscillation period. Generally, the EMR of an arbitrary current distribution is calculated via a multipole expansion. As the name suggests, it includes higher orders than the dipole. Figure 1.6 shows the radiation pattern of a dipole, quadrupole and octopole. We recognize, that a dipole does not emit (far field) radiation in the same direction as its direction of oscillation. Usually, only the first, i.e. the dipole, contribution is kept and the higher orders are neglected.

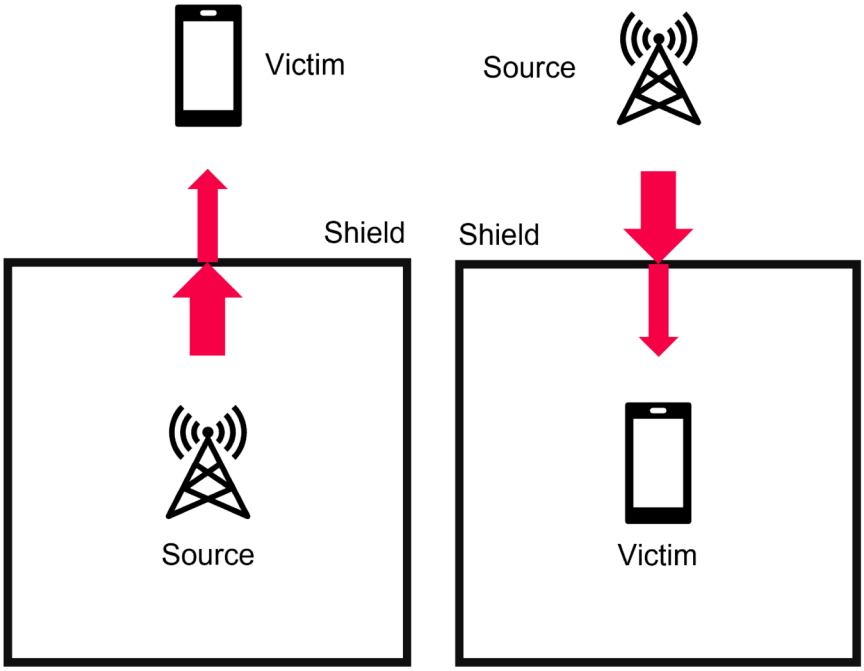


**(a)** Electromagnetic compatibility

**(b)** Electromagnetic immunity

**Figure 1.7:** Schematic of EMI shielding. The task of EMI shields is to minimize transmittance of EMR. This can be done in both ways, with either the victim or the source inside the shield.

## 1.3 Electromagnetic Interference

Electromagnetic interference (EMI) is the mechanism by which EMR originating from the source device disrupts the victim device. In this thesis we work in the setting that the device of interest acts as source and we want to reduce its emission of EMR. However, because every device simultaneously acts as source and victim the relation is bidirectional. Thus, reducing emission also reduces incidence.

The reason why EMI occurs in the first place is that any current acts as the driving quantity in eq. (1.1) that causes energy to be radiated out with a certain frequency. The amount emitted depends on the magnitude and frequency of the driving current, on the geometry of the circuit and also, to some extent, on the environment due to back-coupling. This is considered by circuit design from the start. However, EMI shielding increasingly becomes of interest by the scientific community and industry alike, driven by miniaturization and high-frequency applications.

### 1.3.1 Shielding

To reduce EMI we can apply shielding solutions by enclosing the device or region of space that is of interest with a box or other kind of geometry. The most common applications that we use in day-to-day life are coaxial cables,

microwave ovens and so on. Fundamentally, shields are slabs of materials as in fig. 1.5 that strive to keep EMR out- or inside, as illustrated in fig. 1.7. Mathur and Raman [10] give a comprehensive overview about the principle of EMI shielding, appropriate measurement techniques and the literature which is scattered in different fields of research.

In [20] Williams discusses the effect of seams and apertures and concludes that scrupulous care needs to be taken to avoid them as much as possible, otherwise they completely determine the emission of EMR. Consequently, apertures such as the ones in our sensor that take up a significant area may cause the shielding to be in vain. This needs to be studied in detail and the effect of the apertures needs to be determined.

Considering the physical mechanisms that EMW in matter are subject to (see section 1.2.4), it follows that we can minimize transmittance by maximizing absorption and/or reflection. In the case of a device that is enclosed by a shield, reflected power needs to be absorbed eventually by some material inside the shield.

The standard material for shields are metals, because their enormous conductivity primarily gives rise to reflection, as governed by eq. (1.33). Secondarily, recalling eq. (1.31) we see that the field is attenuated exponentially within a metal by absorption. Only the remaining part is transmitted into the outer region of the shield.

Using a solid metal shield based on reflection is quite a simple approach, even though an effective one. A structure is investigated in [7] which might well be considered the best for EMI shielding, since it makes use of both mechanisms. It consists of three layers: the matching, absorption and reflection layer. The matching layer guides the EMW into the absorption layer suppressing the reflection that would occur without it. There it is absorbed and (most of) the remaining part is reflected by the third layer. However, this structure's dimensions are of the order of mm and cannot directly be adapted to the maximal total thickness of 15 µm necessary in our context. It might be interesting to investigate the possibility of shielding solutions based on absorption with this thickness in the future, but it is disregarded in the following work.

Wanasinghe et al. review the state of the art shielding solutions using metals in [17]. They mainly treat novel materials such as foams and fiber composites that rely on multiple reflection inside the coatings, which increases the total length the EMR has to travel. Thus, more EMR is absorbed. By doing so, they are able to reduce the density of the material, but this increases the volume. They also argue that for shielding with thin films, solid metals work best. Watanabe et al. examine thin, multi-layered structures to improve EMI shielding with a focus on the magnetic field in [19]. They apply the same principle as before, i.e. increasing multiple internal reflection.

Novel advanced materials are consequently developed and investigated as well. A promising category are the 2D MXenes reviewed in [8]. They offer very high shielding capabilities at low thicknesses by combining a high conductivity with a large surface area to increasingly facilitate absorption mechanisms on top of reflection.

These papers give a well-founded starting point for specifying the shielding coating. In this light, the thesis will cover solid metals adapted on the availability of commercial, specialized shielding materials.

#### Shielding Effectiveness

The shielding effectiveness (SE) is a measure of the amount of power $P$ that is shielded in one EMI measurement with respect to another at a certain frequency:

$$SE(\omega) := 10 \log \frac{P_{ref}(\omega)}{P(\omega)} = 20 \log \frac{V_{ref}(\omega)}{V(\omega)} \tag{1.38}$$

It always relates two different materials, configurations, devices, etc. By always using the same reference several can be compared at once. This approach is very handy, since all factors that are the same in both measurements are canceled out. They may even vary over frequency. If the measurement system is linear, we may also use the voltage $V$ instead of the power.

## 1.4 Overview

As was mentioned before, the objective of this thesis is to investigate the EMI shielding achievable by a conductive coating with a maximum thickness of 15 µm that is deposited onto the sensor's lid. Furthermore, multiple materials and thicknesses shall be tested. The coatings were defined and observed in chapter 2.

We have seen above that the conductivity is expected to be the only relevant material characteristic for EMI shielding. Due to the sensor design and the split ground which is connected over the lid and the conductive adhesive as in fig. 2.3, a resistance that is correlated to the deposition's conductivity can be measured between the two ground pins of the assembled sensor. This was conducted in section 2.2.

In chapter 3 the TEM cell measurement system was characterized and applied to measuring the EMI of the TOF sensor. First, several shielding aspects such as the impact of the apertures and the grounding were examined by manually applying copper tape onto the outside of the lids in section 3.4. Secondly, the main performance evaluation of the deposited coatings with the TEM cell was done in section 3.5. Their shielding capabilities over frequency were illustrated and an overall ranking was conducted.

Additionally, a simplified simulation with the EM suite Ansys HFSS was set up in chapter 4, which aimed to mirror the trial with the copper tape and replicate the findings "theoretically".

In chapter 5 a physical model was built. For the emissions of the sensor in the TEM cell, the theory discussed in [12] was reasoned to be appropriate. Because the shielding takes place in the near field, a hypothetical model was proposed and a measurement was set up that allowed for making a prediction for the EMI measurements in the TEM cell due to the VCSEL current.

Finally, a supplementary material characterization method with respect to EMI shielding was done in chapter 6. There, a transmission line set up was built to measure the transmission spectrum of plates that were coated with the same materials as the lids. This allowed us to eliminate the system effects which necessarily occur when the whole sensor is operating.

# Chapter 2

# Depositions

In this chapter, the coatings deposited onto the lid of the TOF sensor in fig. 1.1 for the purpose of EMI shielding are described and investigated. For an overview of the coatings refer to table 2.1. As outlined in chapter 1, the best materials for constructing a thin EMI shield are metals. This is also explained in [10, 20]. Due to their huge conductivity, they reflect the overwhelming part of irradiated EMR below the plasma frequency, which for copper is approximately $2.61 \times 10^{15}$ Hz and for other metals it is also of this order. A layer-based structure including materials such as ferrites or carbon black which absorb EMR like in [7] are, unfortunately, most likely too thick for the application here. There are a host of structures for metals that differ from the solid bulk material which can also be employed for EMI shielding in applications for which weight is a limiting factor (see [17]). More exotic materials such as the MXenes investigated in [8] further attempt to fill this demand. In essence, materials trying to reduce the weight focus more on surface effects than volume effects. E.g. porous structures introduce multiple air-material interfaces which have more absorbing surface dipoles and enable multiple reflection which in turn increases the distance light has to travel, resulting in more absorption. The same strategy may be adapted to solid metals like in [19]. A layered structure of different metals creates interfaces of optically different materials which increases the total travel distance of EMR. It may also get absorbed inside the metal, not just reflected to and fro. Hence, the latter structure would also be worthwhile to examine. However, this was not considered here.

For these reasons, the coatings used are all solid bulk metals, which is of course relative and subject to restrictions of the coating processes. One coating was sputtered by me, which is documented in section 2.1. The other coatings were deposited by external companies. They employed different coating processes and/or materials, which naturally result in different micro-structures and potentially different SE. The manufacturers are anonymized and assigned unique letters. For the remaining evaluation the naming convention will combine the coating letter(s) and the thickness, i.e. A10 is the coating A with the nominal thickness of 10 µm. Naturally, SPUT denotes the sputtered coating.

The spray coating and the sputtering processes are straight forward. Manufacturer B employed inkjet printing to deposit a metal organic decomposition

**Table 2.1:** Coatings for EMI shielding of the TOF sensor.

| Coating | Material | Process | Thickness / µm |
|---|---|---|---|
| A | - | Spray coating | 5 / 10 |
| B | Silver MOD ink | Inkjet printing | 3 / 6 / 10 |
| C | - | Spray coating | 3 / 6 / 12 |
| SGP | Silver-coated copper | Spray coating | 15 |
| SPUT | Platin-palladium | Sputtering | 4 |
| U | Uncoated | - | - |

(MOD) ink on the product, which should provide the advantage that the thin film is more homogeneous with a higher conductivity. That is because for the spray coating, metal particles are only suspended in a carrier liquid. MOD, on the other hand, brings the metal in solution. After both processes, the liquid is removed by curing. The sputtering immediately creates a solid film, which should be highly conductive. However, it is an expensive technology when outsourced.

Two sample types were coated: The LCP lids which are evaluated in the TEM cell (chapter 3), and $30 \times 30 \times 1\,\text{mm}$ LCP plates which are used in the transmission line measurements (see chapter 6). Depositing a film onto a 2D structure like the plates is much easier than onto a 3D lid, because it is expected that the deposition rate depends on the projected area with respect to the deposition direction. This usually causes different thicknesses. The grounding quality of the coated lids in the assembled devices and a ranking in terms of the conductivity of the material was assessed via the resistance measurement in section 2.2. The thickness and grounding of the coatings were investigated via cross sections in appendix B.

The sensors were assembled in two batches. The first one contained U and SGP, which is why some of the evaluation is restricted to these. In the second one were A, B and SPUT. This can have an impact on assembly related properties, such as the resistance due to the conductive adhesive.

## 2.1 Sputtering

The sputtered coating was fabricated with the sputter coater in fig. 2.1 (Cressington, 208HR) and a platinum-palladium target (Cressington, P0128). The setup is designed for short depositions of a few nm on samples that are to be examined in a scanning electron microscope (SEM). The chamber is evacuated with a pre-vacuum pump and a turbo-molecular pump and supplied with argon gas via an adjustable leak valve. Unfortunately, the quartz oscillator was not calibrated and instead the thickness was directly determined from the deposition time. For this calibration, a silicon wafer was used as substrate, because it is easy to handle in that the wafer can be broken along the crystal axes if it first notched slightly with a diamond-tipped tool. The coated piece

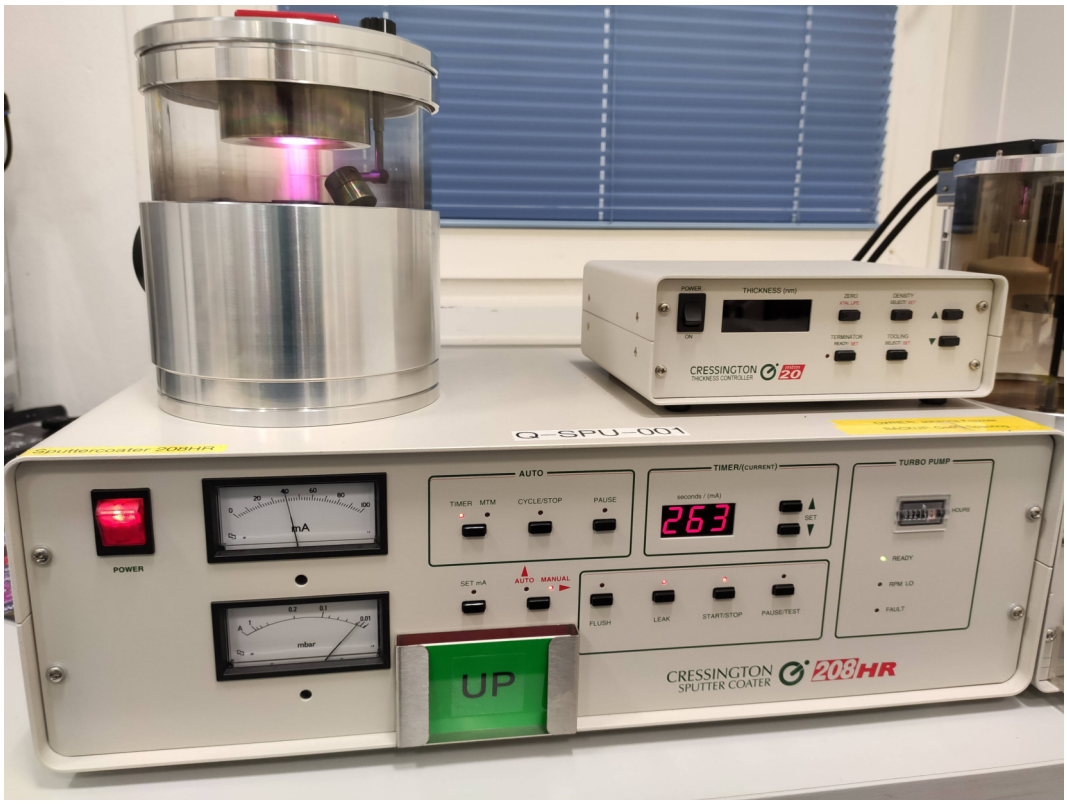


**Figure 2.1:** Sputter coater

is then broken again in the middle and one piece is vertically mounted inside the SEM to measure the thickness. These trials resulted in the estimation that 25 min of sputtering with a current of 40 mA and 0.03 mbar chamber pressure deposits approximately 1.4 µm to 1.6 µm onto the silicon. However, the deposition rate is highly dependent on the partial and total pressures inside the vacuum chamber. During the experiment problems occurred in that the Ar partial pressure needed to be increased significantly for the plasma to ignite after renewing the sputter target. In theory, a higher Ar pressure decreases the deposition rate and increases diffuse deposition, which should be favorably to also coat the sidewalls of the lid. This issue was later resolved by reassembling and cleaning the coater. It is therefore plausible that after this routine the deposition rate changed. Hence, it was instead decided to move onto the LCP lids and planar samples immediately, because they need to be analyzed in any case. However, the feasibility of creating such a thick film with the existing sputter coater was demonstrated.

The LCP lids and 11 × 11 mm plate were coated in the same conditions: 40 mA and 0.03 mbar for 20 min. The thicknesses were determined by a focused ion beam (FIB) equipment, resulting in $(500 \pm 150)$ nm which is significantly less than expected. This illustrates that it is hard to get reproducible coatings with the deposition system. There are many factors that cause the discrepancy in deposition rates, e.g. the achievable vacuum pressure, the partial argon pressure, the position of the samples inside the coater (central or off-center) or the sputtering current. For future trials on this setup it would therefore be highly recommended to calibrate and use the quartz oscillator, because it

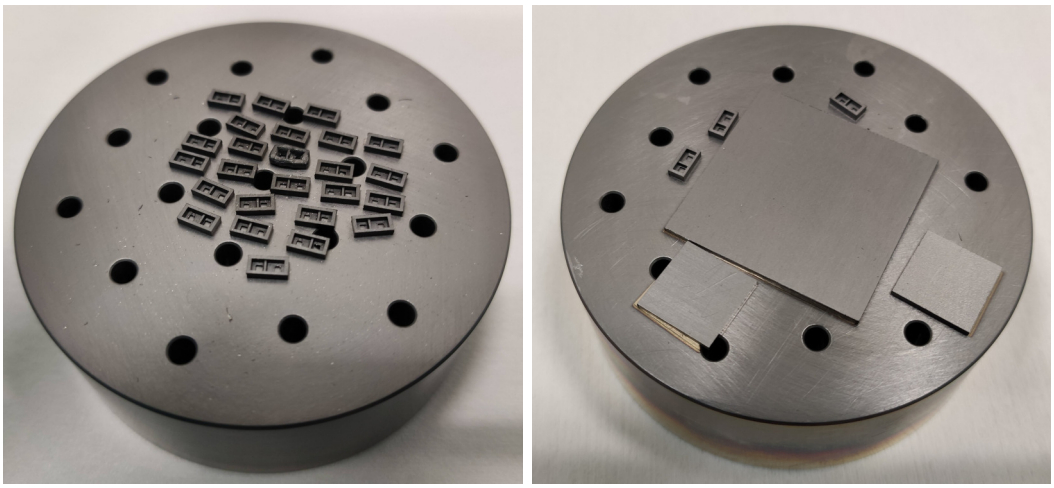

**(a)** Lids **(b)** Plates

**Figure 2.2:** Sputtered LCP lids for the shielding of the TOF sensor and plates for the transmission line measurements.

would record changing deposition rates.

Finally, new sputtered LCP lids were coated with 80 mA and 0.02 mbar for 10 min to get a higher coating thickness. After this time the argon pressure was increased to 0.05 mbar, because the central LCP lid deformed, possibly due to a concentrated, directional metal particle stream onto it creating intense heat. The higher pressure should achieve a more diffuse process to spread the heat transfer. The deposition was continued for 50 min, i.e. 60 min in total. The resulting lids are depicted in fig. 2.2a. For this final batch of lids and plates the thickness was determined via cross-sections documented in appendix B.

For studies pursuing the sputtering of the shielding coatings, it would be best to switch the setup to one that is better suited for the desired thicknesses. We saw that it is possible with the current coater, but the inconsistencies in the setup do not allow for a steady process. A first improvement would be to calibrate and use the quartz thickness monitor. However, because the shielding of the deposited film was not effective (as we will see in chapters 3 and 6), other sputter target materials should be used. Since most of the other coatings contain silver, that would be an obvious choice. As was mentioned before, sputtering is usually known to lead to highly dense and conductive coatings. Therefore, it is expected that with the right setup and material a good shielding film can be produced.

## 2.2 Resistances

As discussed in section 1.1, a resistance can be measured between the two ground pins in the assembled devices, which shows us if the coating on the lid is well connected to them or if it is floating. This is depicted in the diagram in fig. 2.3. There are two parallel resistances: the conductive adhesive and the coated lid. The conductive adhesive always connects the two ground pins and

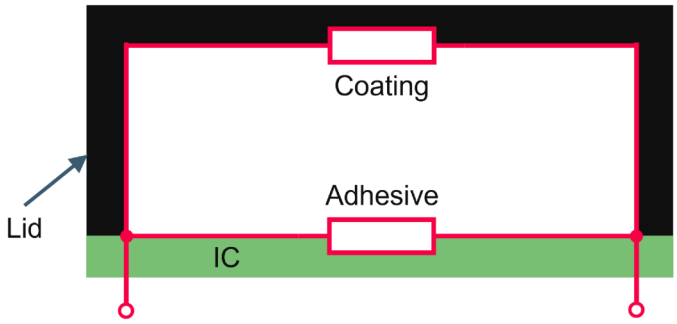


**Figure 2.3:** Schematical cross section and electrical diagram for the resistance between the two ground pins of the assembled TOF sensor.

therfore the uncoated sensors also possess a resistance. The total resistance is reduced if the coating leads to a lower partial resistance. Because that depends on the material conductivity and on the thickness of the layer, we can observe trends for the different coatings and rank them in that regard via a statistical analysis of their resistances. From chapter 1 we know that the conductivity of the material should be the only important property. Hence, the shielding capabilities can be characterized in this way. The adhesive has a conductivity which is low enough such that the pins are not always shorted and a meaningful value can be measured, but also high enough to ensure the grounding of the lid when the adhesive thickness is small.

The assembled sensors were contacted using a prober (Karl Suss, PM 8). The setup is depicted in fig. 2.4. To contact the ground pins four needles held by mounts were pressed onto them. These can be connected to the multimeter (Agilent, 34401A) via the connections on the mounts. The purpose of the 4-wire-measurement is to eliminate the contact resistance that would ordinarily occur with two wires. Because that is in the order of the resistance between the pins, this would have compromised the measurement.

The resistances are shown in the violin plot fig. 2.5. In this graph only sensors with a resistance lower than 2 Ω are depicted, which confines the analysis to devices that do not have an issue with the conductive adhesive. That value was extracted from the uncoated devices. It is unexpected that any device has a higher resistance than the uncoated lids, because a parallel resistance cannot increase the total one. That implicates that the sensors, for which that is the case, have an issue with the assembly that also impacted the resistance due to the conductive adhesive. Thus, this is a problematic of the assembly which can also sever the grounding of the lids. Therefore, it is meaningless to consider these sensors for a study about the coatings.

The coatings are ordered by their mean value. The uncoated sensor (U) is setting a benchmark. We can see that the sputtered lids clearly have a higher resistance. Hence, there must be something wrong with the assembly for these devices. That can still be connected to the coating, if it impacts the assembly process. The remaining outsourced depositions divide into two groups, within which they are hard to rank. Coating B definitely leads to higher resistances, than A and SGP. The 10 µm thick coatings of A and B also improve the situation compared to their 5 µm and 6 µm thick versions. Unfortunately,

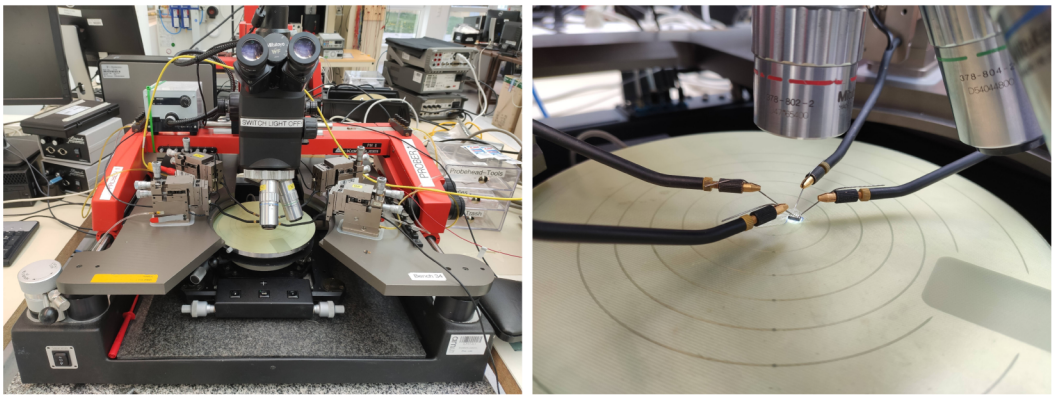

**(a)** Prober **(b)** Needles

**Figure 2.4:** Setup for the 4-wire resistance measurements of the assembled TOF sensors.

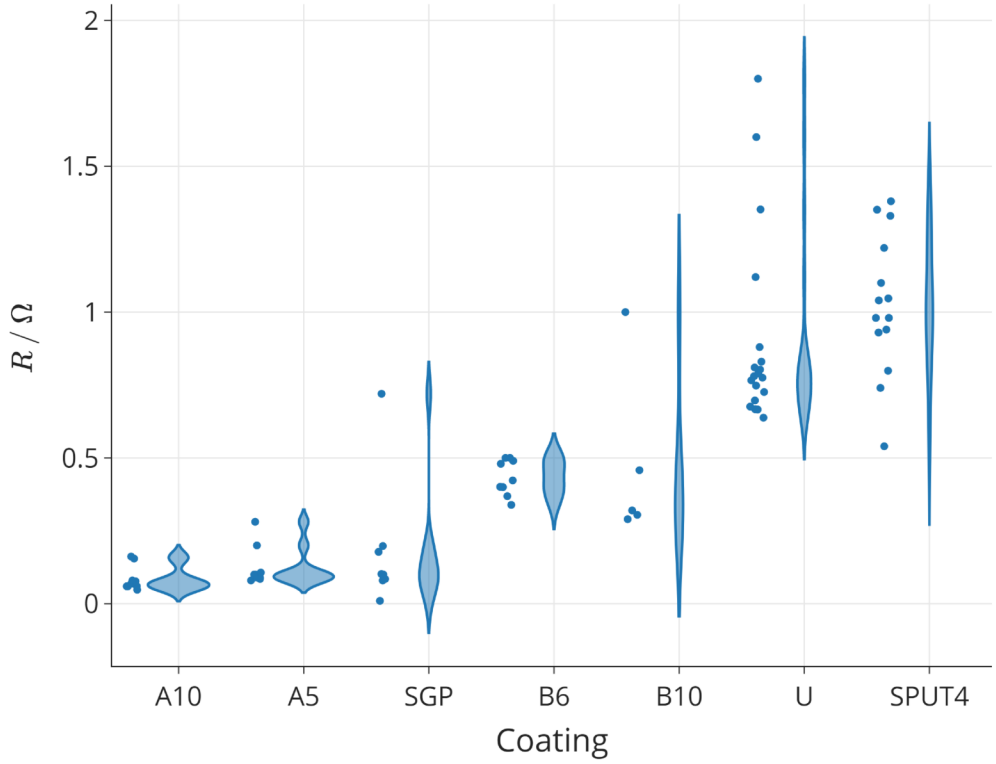


**Figure 2.5:** Violin plot of the resistances of the assembled TOF sensors measured between their two ground pins with a 4-wire setup. Only resistances below 2 Ω and thus only well grounded devices are considered.

there are many outliers, probably due to the assembly process, which makes a transparent ranking of the depositions difficult. Nevertheless, we expect based on these measurements that coatings A and SGP to shield better than B, and that the sputtered sensors only show a diminishing improvement.

The experiments indicate that the conductivity of the coatings was not the limiting factor in determining the shielding effectiveness, since based on the resistance measurements there should be a clear ranking of the coating materials possible. In chapter chapter 3 it is argued that the connection of the lid to the ground is impeding it. In chapters 4 and 5 it is explained that the directional manner in which the lids are grounded is the reason why mainly one of the orientation spectra of the TEM cell is attenuated.

# Chapter 3

# TEM Cell

In this chapter, the results of the transverse electromagnetic (TEM) cell measurements of the time of flight (TOF) sensor are evaluated. The corresponding setup, its limitations and the evaluation strategy are described. The device is in a first study shielded by manually applying a copper tape on the outside of the lid and various configurations are tried and aspects such as grounding and apertures are investigated. Further, the sensors shielded by the coated lids with the depositions described in chapter 2 are analyzed.

## 3.1 Setup

A TEM cell is a setup for measuring EMI emissions (see fig. 3.1). In essence, it is a transmission line that has coaxial cable connectors on both sides. On one side the measurement device is connected and the other side is terminated with a $50\,\Omega$ termination impedance. In between the central conductor is a stripline and the sidewalls are flared up, such that it has a constant impedance of $50\,\Omega$. A part of the sidewall is a window into which the device under test (DUT) is mounted with its PCB. The DUT emits EMR that couples the outer and inner conductors and a signal propagates into the coaxial cable and to the EMI test receiver. This TEM cell with the stripline is also called a micro TEM cell due to its small form factor or just stripline. The PCB which was used to mount and electrically connect the sensor in these measurements (EMI board) is depicted in fig. 3.2. The DUT (with its EMI board) can be inserted in four orientations into the TEM cell, such that it still seals: 0°, 90°, 180° and 270°. In principle, the setup was according to the standard [3], with a different frequency range. The sensor was powered by the power supply and operated by the Raspberry Pi, which was connected to a PC via USB and to the EMI board via an extension. The Raspberry Pi was controlled by a driver and a Windows software running on a host-PC. The EMI test receiver was controlled by a Python program. The setup is summarized in table 3.1.

The EMI test receiver can be operated in different modes and with various parameters. Here it was used as a spectrum analyzer which means that a frequency range was scanned and the measured voltage was recorded resulting

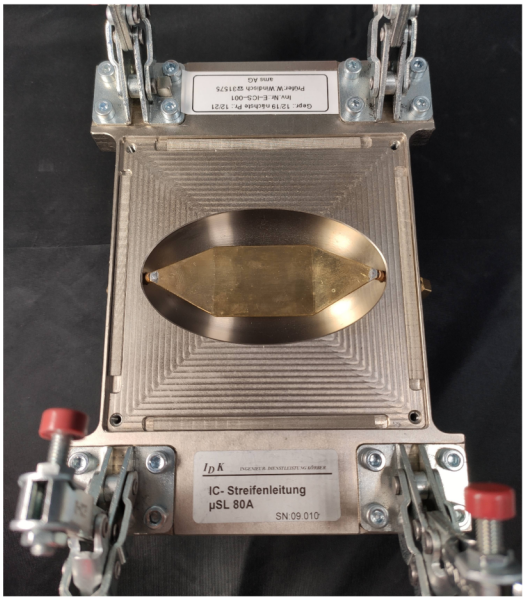


**(a)** Open TEM cell

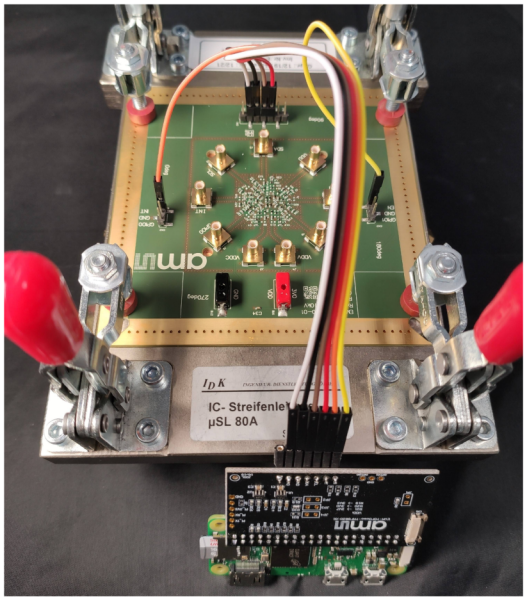


**(b)** TEM cell with PCB, DUT (inside) and Raspberry Pi

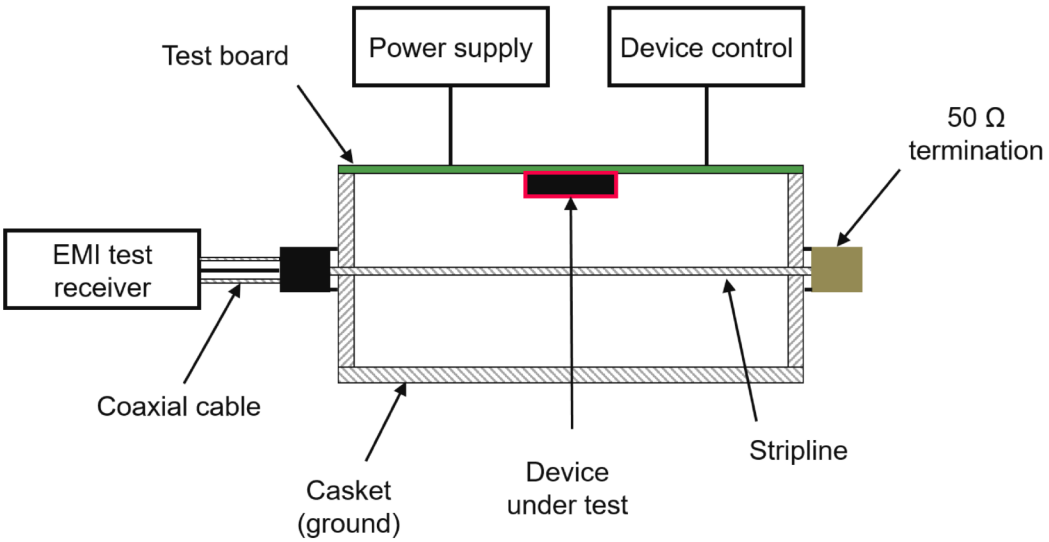


**(c)** Schematic

**Figure 3.1:** Setup with the TEM cell used for measuring EMI emissions.

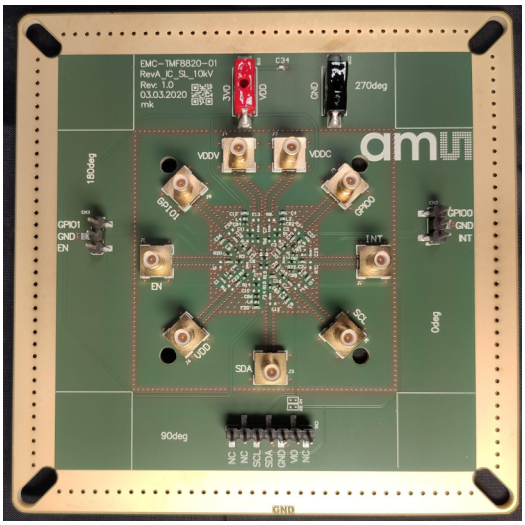


**(a)** Top side

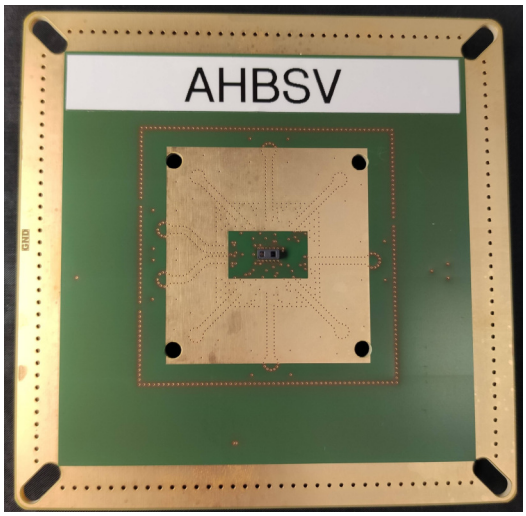


**(b)** Bottom side

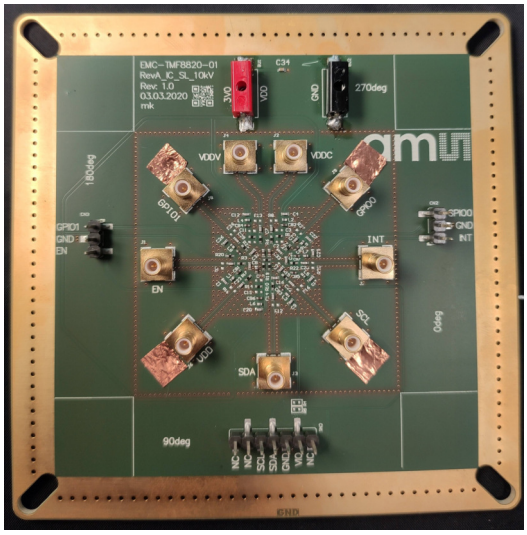


**(c)** Closed Holes

**Figure 3.2:** EMI board used for TEM cell measurements. (a): Top view. (b): Bottom view. (c): The holes are sealed with the copper tape to prevent EMR from entering from the outside.

**Table 3.1:** Experimental setup for measuring the EMI of the TOF sensor in the TEM cell according to IEC 61967-2.

| Device | Manufacturer | Type | Description |
|---|---|---|---|
| EMI test receiver | Rohde & Schwarz | ESRP7 | Frequency range: 9 kHz to 7 GHz |
| TEM cell | Ingenieur-Dienstleister Koerber | $\mu$SL 80A | Terminated with a 50 Ω impedance. |
| Raspberry Pi | Raspberry Pi Foundation | Zero W | |
| Raspberry Pi extension | ams-OSRAM AG | | |
| EMI board | | | |
| TOF sensor | ams-OSRAM AG | TMF8821 | |
| Raspberry Pi Software | ams-OSRAM AG | TMF882X EVM | |
| Raspberry Pi driver | ams-OSRAM AG | | |
| Coaxial cable | | | Connects TEM Cell to EMI test receiver |

in a spectrum. For each orientation of the DUT in the TEM cell there is an associated spectrum. The frequency range was split into two subranges and the resolution was set as in the usual EMI measurements recommended by the CISPR 16-1-1 standard [13]. The test receiver offers the ability to record in the time-domain, immediately convert to digital values and apply a FFT to greatly reduce the overall duration of a sweep. Initially, the measurement time was set too low, such that parts of the spectrum falsely appeared to be around the noise level. After increasing the measurement time, this issue was resolved. The reason for that is discussed in [9].

A typical measurement result is plotted in fig. 3.3, where an uncoated sensor was used. We see that the spectra consist of densely packed peaks, with only noise in between. Further, we recognize that their height varies and also their width, which is apparent when zooming in. Their frequency ranges from kHz to GHz where they decay eventually. This is the consequence of the electrical currents. Because of their periodicity, they can be mapped from being a function of time to being a function of frequency, where only the multiples of the fundamental frequency have nonzero values. In the case of the VCSEL current it is 17.7 MHz, as was mentioned in section 1.1. This can be investigated more closely by conducting a FFT, which we see in fig. 5.6. Because of the linearity of the system, we know that the current can only excite EMI at frequencies that itself possesses and the intensity should be proportional to the square of the amplitude, i.e. the Fourier coefficients. The

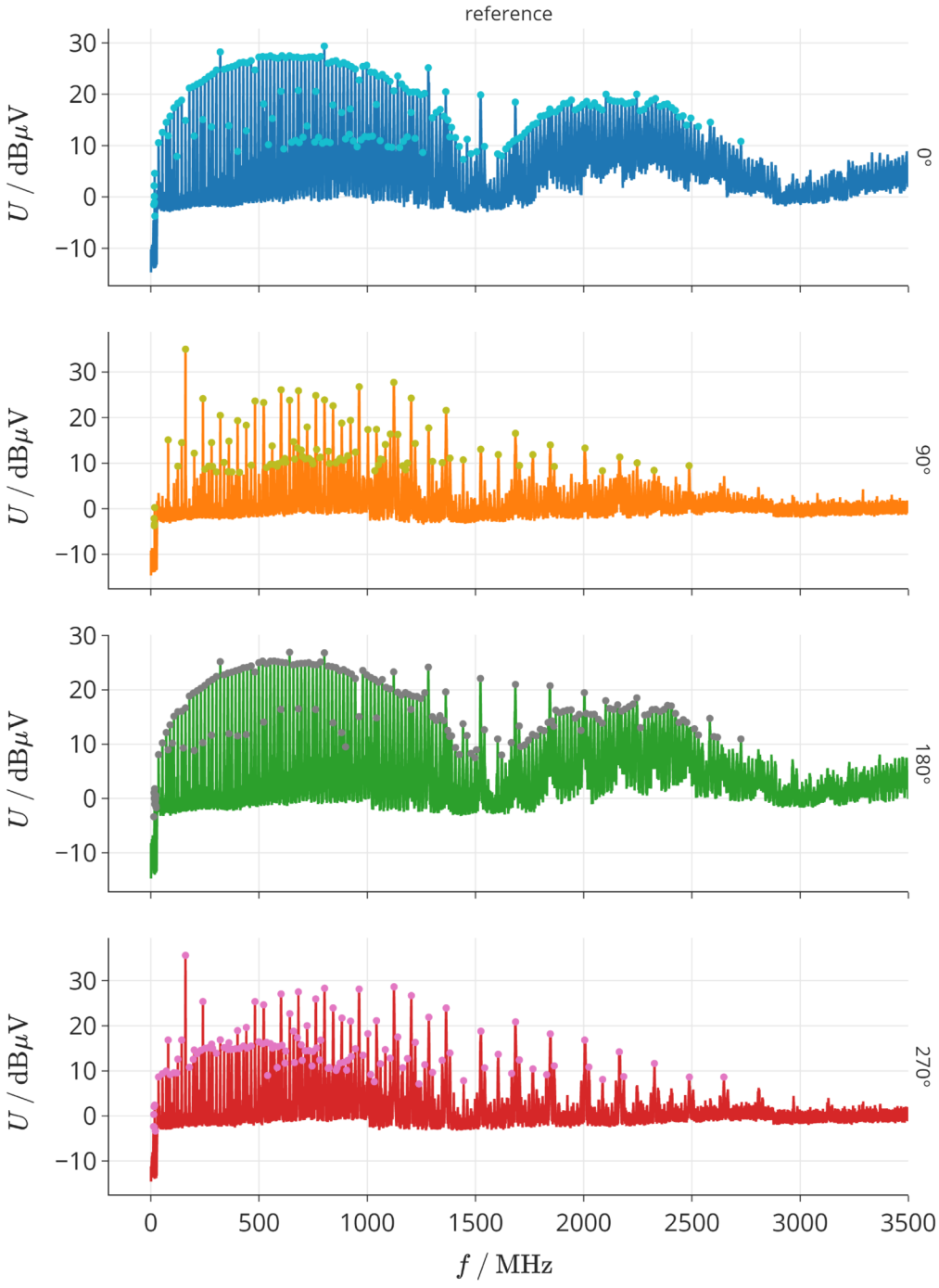


**Figure 3.3:** Typical spectra with highlighted peaks of different orientation from the TOF sensor measured in the TEM cell.

first statement was confirmed in section 5.1.1, while the second is not yet proven. However, the general trend at least should follow the magnitude of the FFT. In the complete sensor, however, there are many electrical components whose Fourier coefficients all superpose, which explains the array of peaks in fig. 3.3. Since we are mostly interested in reducing the magnitude of the larger peaks, it is insightful to investigate their general properties in more detail, which is conducted in section 3.2.

At first, the spectra were recorded between 15 kHz to 4 GHz. However, below 1 MHz peaks appear in the spectrum that were traced back to the Raspberry Pi by comparing two spectra of different test modes (see fig. 3.4), where this time the frequency axis was plotted logarithmically to be able to see the lower frequency range. In the left column the sensor was inactive and nothing was connected to the EMI board, but it was still mounted in the TEM cell and connected to the test receiver, naturally. In the right column the sensor was also inactive, i.e. the power supply was disconnected, while the Raspberry Pi was plugged in. An important note is that before disconnecting the power, the sensor was active once, i.e. the power supply and the Raspberry Pi were both connected and operating, which may have had an effect. It is immediately apparent that this had a major impact on the spectrum in this frequency range. Above 3.5 GHz the spectra of the device in operation decrease in magnitude significantly and becomes comparable to the noise level, because the TEM cell is designed to measure below that value. Thus, it was determined to observe a frequency range between 1 MHz and 3.5 GHz for an optimal quality and ease of assessment, while keeping the range 15 kHz to 4 GHz in the measurements for consistency.

The final parameters that were used for the measurements in this thesis can be found in table 3.2. An attenuation of 0 dB was used to maximize the signal to noise ratio and the remaining ones were discussed above.

**Table 3.2:** Settings for the EMI test receiver for the TEM cell measurements.

| **Start** / MHz | **Stop** / MHz | **Res.** / kHz | **Time** / ms | **Atten.** / dB |
|---|---|---|---|---|
| 0.015 | 30 | 9 | 300 | 0 |
| 30 | 4000 | 120 | 50 | 0 |

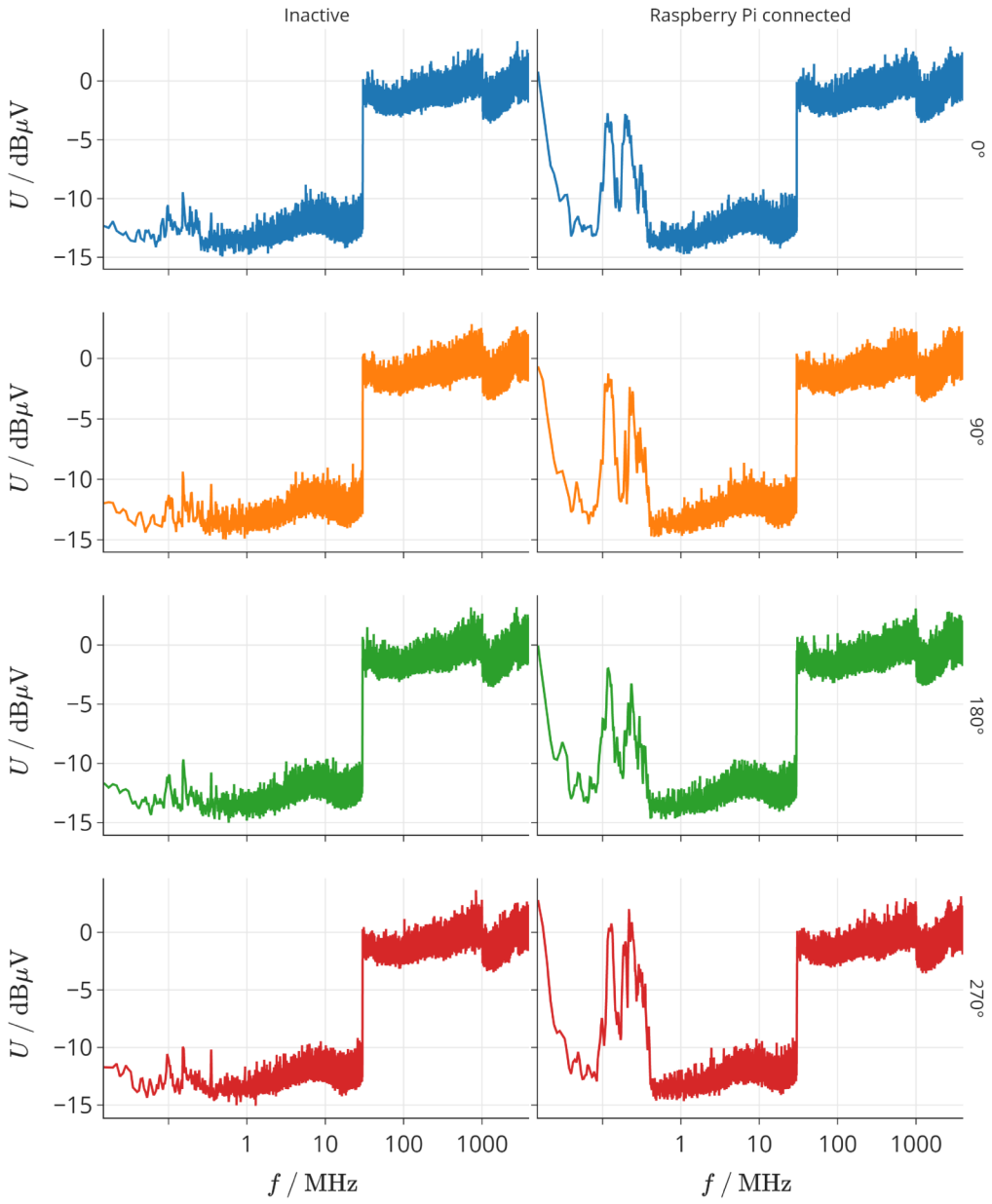


**Figure 3.4:** TEM cell measurements of the inactive TOF sensor. Left: Nothing connected to the EMI board at all. Right: With operating Raspberry Pi, which is connected to the EMI board and the PC.

## 3.2 Precision and Repeatability

The repeatability of the TEM cell measurement was demonstrated in figs. 3.5 and 3.6. Measuring the sensor's EMI emissions in the TEM cell five times per orientation without altering the setup in-between at all yielded slightly different spectra. This manifested in a choppy peak form and a varying peak position (frequency). The peaks of the five repeatability TEM cell measurements were statistically analyzed in fig. 3.7, where the mean and the standard deviation of the matched peaks' SE is plotted together with one of the spectra. Note that this evaluation was conducted in linear voltage scale and the peaks in the different spectra where matched, i.e. the closest peaks were broadcasted onto the same frequency in order to avoid the shift we see in fig. 3.6. This will be elaborated more in the next section. We see that the peaks line up very consistently with the single plotted spectrum, which is validated by the small standard deviation. 90 % of the standard deviation over frequency stays below 2 µV, so we can safely assume that as an overall measurement error estimate of the peak height in the observed frequency range. By extension, this error is assumed not just for the peaks, but for all values, as is they are expected to behave similarly and the exact peak form is not of interest.

In fig. 3.8 the mean width and the mean frequency shift of the peaks in the repeatability measurement are depicted. We see that they increase significantly with frequency. Hence, any algorithm which incorporates the peak width in any way should consider that. In principle, that also includes the peak-detection algorithm itself. However, we see from the spectra and in more detail if one observes them at higher zoom levels that most of the correct peaks are detected, even at higher frequencies. Therefore, it was not altered.

Considering the spectra and the statistical evaluation shown in this section, we can see that the measurements of the 0°/90° and the 180°/270° orientations are respectively equivalent due to the symmetry of the TEM cell. Hence, only the 0° and 90° spectra will be used for the remaining evaluation. In chapter 5 the same observation is made based on a single bondwire antenna.

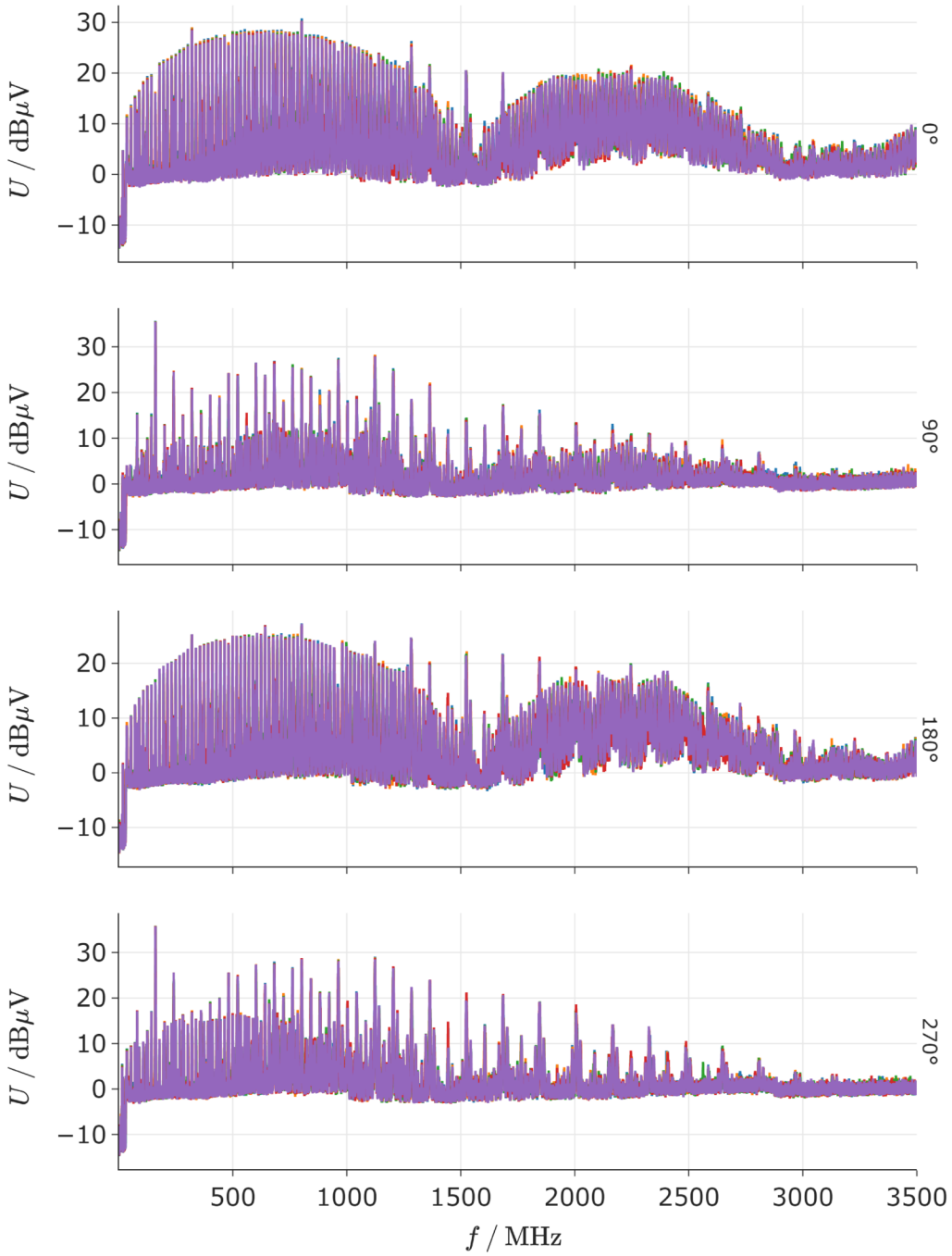


**Figure 3.5:** Repeatability TEM cell measurements of the TOF sensor without shielding. For each orientation five spectra were recorded.

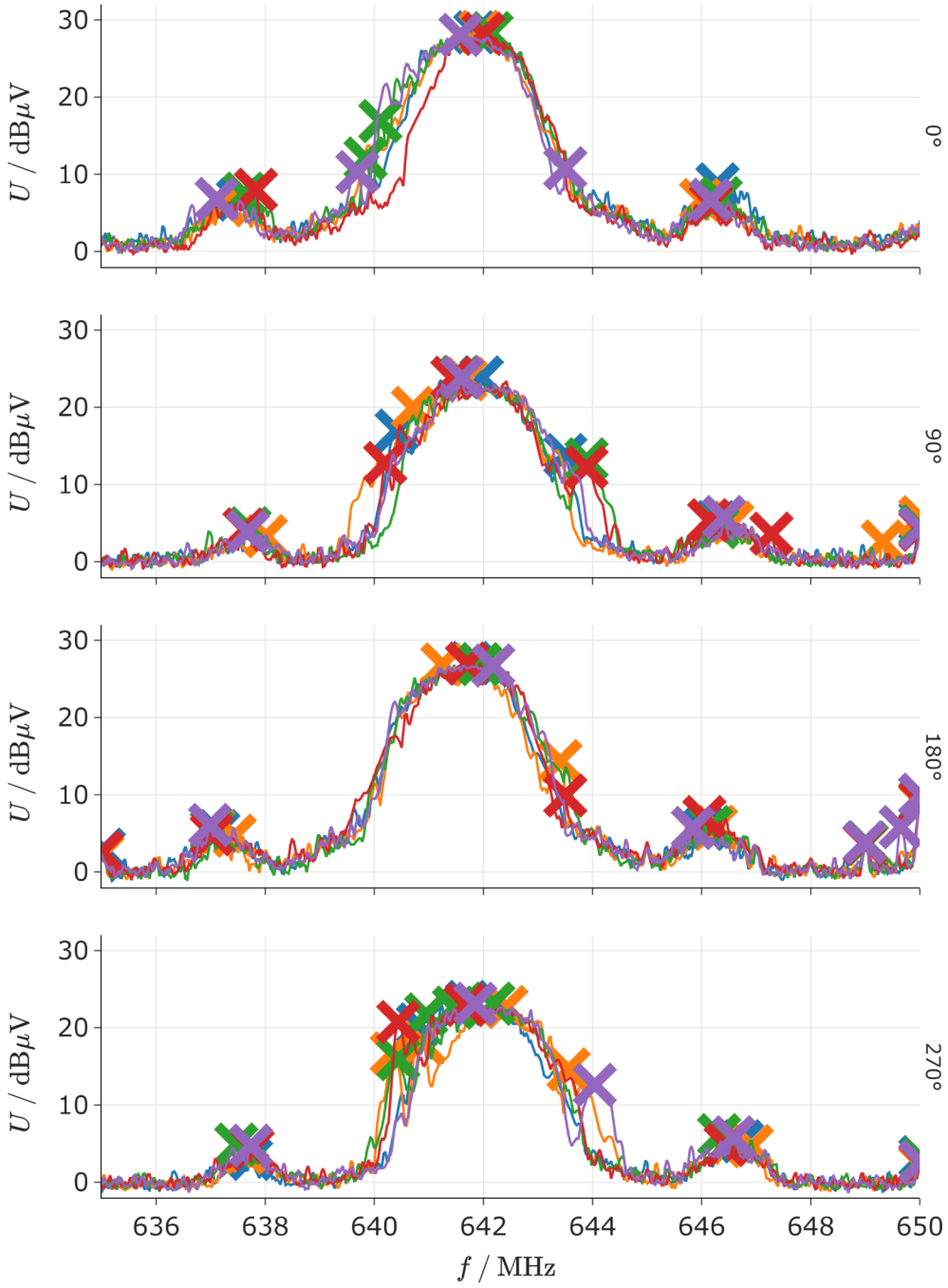


**Figure 3.6:** Spectra with detected peaks in the repeatability TEM cell measurements of the TOF sensor without shielding. For each orientation five spectra were recorded.

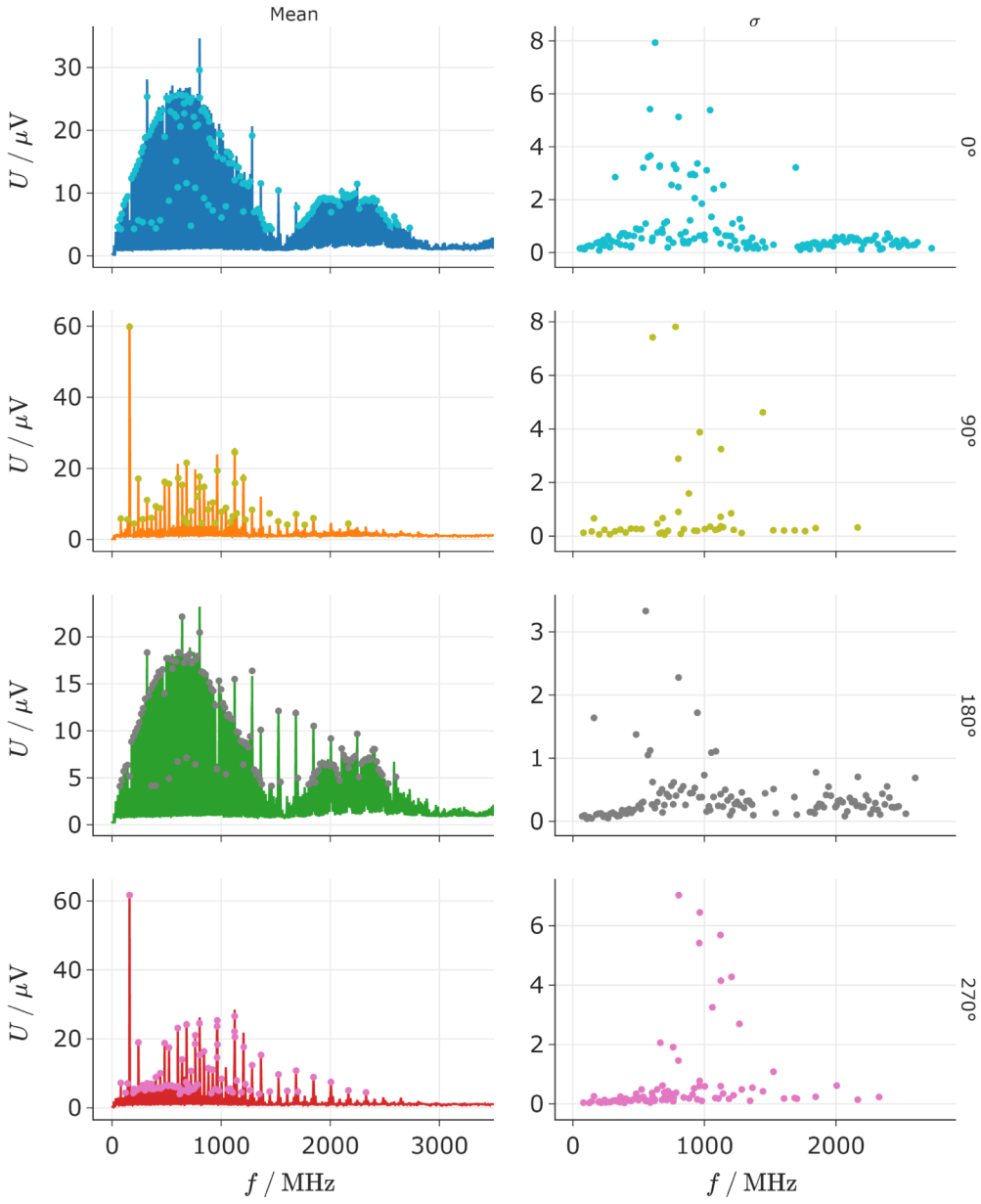


**Figure 3.7:** Statistical evaluation of frequency of the peaks in the repeatability TEM cell measurements (fig. 3.5) of the TOF sensor without shielding. For each orientation five spectra were recorded.

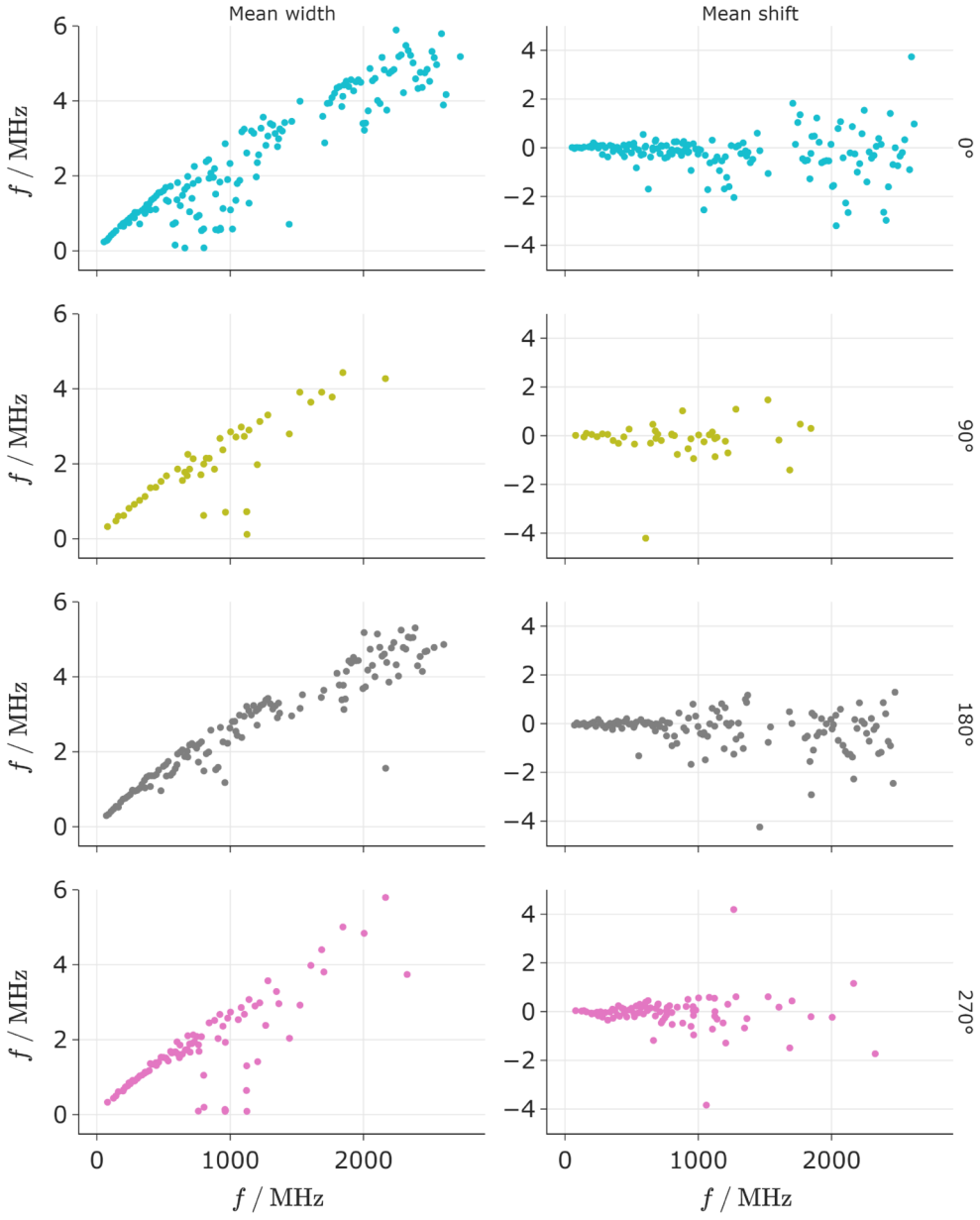


**Figure 3.8:** Mean width and frequency shift of the peaks in the repeatability TEM cell measurements (fig. 3.5) of the TOF sensor without shielding.

## 3.3 Shielding Evaluation Strategy

The obvious, because most desirably, approach to calculate the SE as a function of frequency would be to subtract the spectra in dB µV (if the measured quantity is also logarithmic, the division in eq. (1.38) becomes a subtraction). However, because the data is slightly offset and noisy as discussed above, this yields attenuations that are noisy themselves and range between −10 dB to 10 dB for measurements of completely identical configurations. The random frequency shift becomes especially bothersome at higher frequencies where the peaks are wider. This property is a limitation of the test receiver. It was attempted to smooth the data before and after subtraction, but that did not yield reliable results either. Furthermore, it was extensively experimented with the test receiver's parameters (see table 3.2) in a systematic fashion by recording two spectra, subtracting these and evaluating the magnitude of the "noise" in the resulting spectrum, but no combination could stabilize the detected peak form. In the course of that the available detectors of the test receiver were also investigated. The average and quasi-peak detectors somewhat mitigated this issue, but they could not eliminate it completely. Moreover, avoiding the maximum peak detector is contradictory to the objective, since this is the one commonly used for compliance testing.

To correct for the frequency shift, it was attempted to alter the approach to match the peaks and project them onto the same frequency. Using one spectra as reference spectrum, the closest peaks, which have to be within a maximum distance of 10 % of the mean of both peak frequencies, were matched and projected onto the frequency of the reference's peak. This was not done in fig. 3.6, but it would cause the peaks marked with an x to be at the exact same frequency. It was already used for the statistical analysis above. The heights of the matched peaks are then subtracted resulting in the SE. The legitimacy of this data processing is supported by the fact that the ultimate objective in this thesis is to reduce the maximum peak height of TEM cell measurements. The frequency shift that is omitted must be manually investigated for sensitive frequency bands using the complete spectra.

Another strategy to process the spectra is to fit the outline of the spectrum, which inherently mostly considers the largest peaks, depending on the accuracy factor and the length scale of the fitting function. The, probably, most simple one is to fit the detected, sparse peaks with a spline. However, that failed owing to the property that the peaks can jump many orders of magnitude from frequency to frequency and also from device to device, especially when also shielded sensors are measured.

Furthermore, the variation of the fundamental frequency is an additional severe factor impacting the spectra of two different devices. This arises, because the electrical components have varying resistors, inductors and capacitors. The error can be different for each of them leading to parts of the resulting spectrum being shifted differently. Hence, it is not easily possible to scale the frequency range to counteract it. This issue could be counteracted by trimming the sensors, i.e. calibrating them with external, adjustable components such that they behave the same fundamental frequency. On top of that,

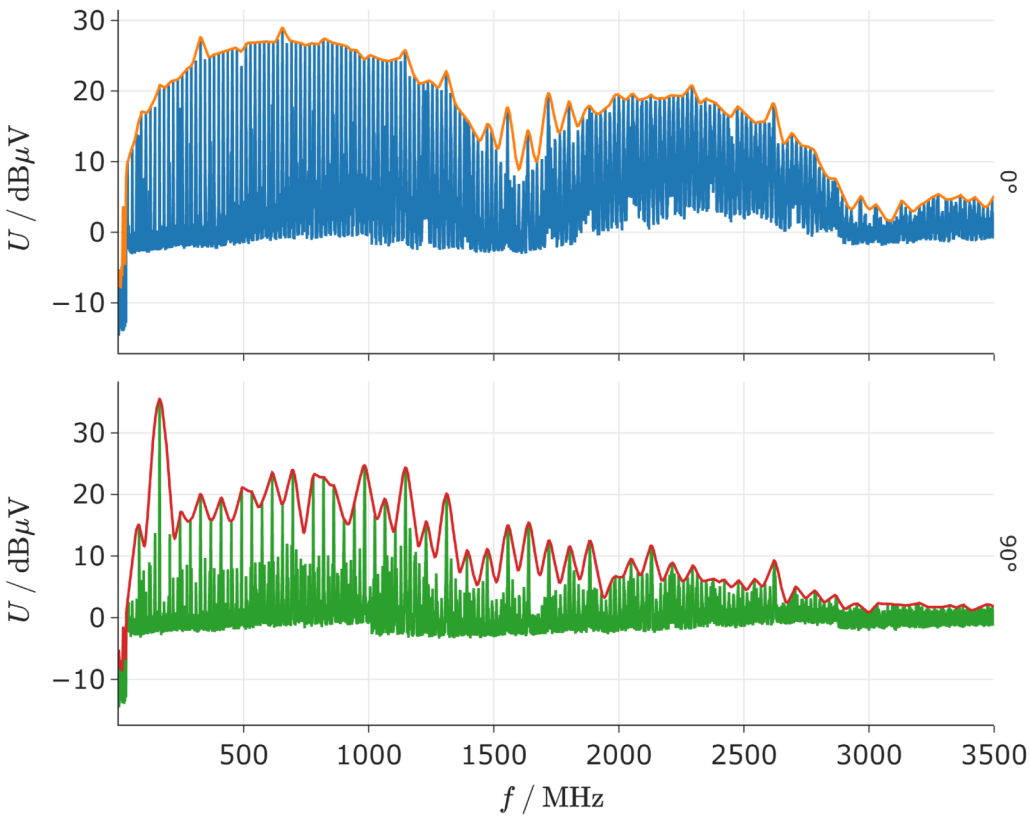


**Figure 3.9:** ALS envelope of a TEM cell spectrum of an uncoated TOF sensor.

more variations due to the inhomogeneity of the depositions of the shielded lids (see appendix B) are to be expected. These factors all combine and render it unfeasible to calculate the SE as a function of frequency, especially for two different sensors.

Fortunately, two more robust algorithms are described in [2, 23]. They are designed to correct the baseline of optical spectra, but by multiplying the spectra with $-1$ their peaks can be fit with this regression. They both feature a smoothing and a precision factor, where the smoothing parameter serves as the aforementioned characteristic length. The asymmetric least squares (ALS) method approximates the peaks more "naturally", whereas the adaptive iteratively reweighted penalized least squares (AIRPLS) yields "pointy" envelopes. Both work well for the regression of the spectra. It is also advantageous that the spectra may be supplied to them unmodified without the need to detect the peaks first, as was necessary with splines.

It was decided to use the ALS algorithm with its optimized implementation in Python taken from [15] and listed in appendix C.1. An envelope of an uncoated sensor is plotted in fig. 3.9. The parameters were chosen such that the larger peaks are included with a small increase in width. They also can be found in appendix C.1.

One worthwhile try would be to fit both the reference and the new measurement with an envelope and subtract them again to get the SE. However,

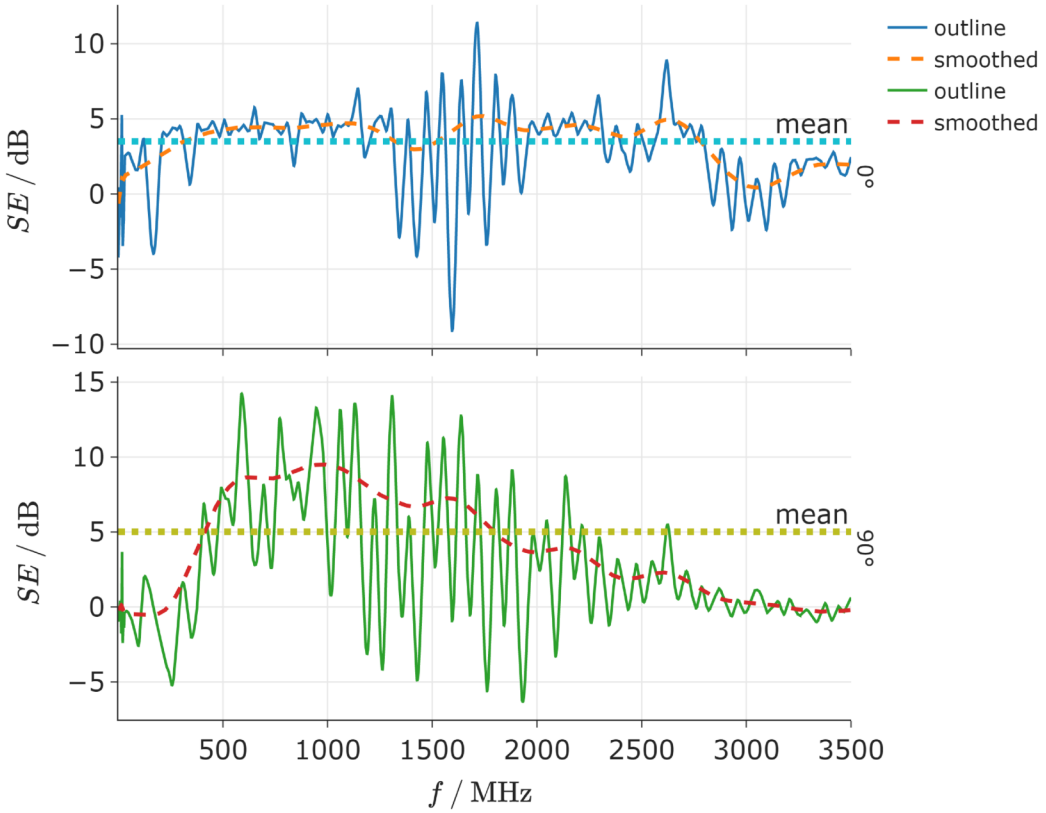


**Figure 3.10:** Example SE of a coated lid of the TOF sensor based on an ALS envelope of the TEM cell measurements.

the same problem as above remains. Nevertheless, this attempt was conducted and an example using a coated and an uncoated device is plotted in fig. 3.10. These SE spectra are very hard to interpret because of the oscillations that arise due to slightly shifted peaks. A smoothed line can also be seen in this image, which was calculated by convolving its SE with a Gaussian kernel in linear scale. Hence, some frequency information where the configuration is shielding well is extracted, on a problematic basis however.

Because computing the SE as a function of frequency proved so difficult due to the frequency shift of the EMI test receiver and the electrical variation of the sensors, a simpler and thus more robust approach was chosen. This consists of two parts: First, to evaluate the shielding over frequency the envelopes are computed with the ALS algorithm and plotted for visual comparison. Secondly, to rank the different coatings the integral of the spectrum is calculated, where it is normalized to an equivalent voltage by dividing the integral with the frequency range:

$$\bar{U} = \frac{1}{f_b - f_a} \int_{f_a}^{f_b} U(\omega) d\omega \tag{3.1}$$

Since this evaluations is of comparative nature, the noise that is also integrated is not an important factor. In fact, the offset due to the background noise can be compensated by evaluating its equivalent voltage from the measurement of an inactive device and subtracting it. It was calculated to be $(0.90 \pm 0.05)\,\mu\mathrm{V}$.

Additional to the whole integral ranging from 1 MHz to 3500 MHz this versatile measure can be computed for any frequency range, such as those mentioned in section 1.4. However, because the sensitive frequency ranges are very small, e.g. for GPS/Galileo/GLONASS they are in the order of MHz, the frequency shifts in the EMI spectra may cause peaks to randomly fall in or out of them. Hence, it was decided to omit their evaluation. For future studies, it would be interesting to investigate whether the SE shows distinct values in these ranges for different shielding coatings.

## 3.4 Copper Tape

For a first estimation about how much shielding can be achieved given the limitations due to the sensor, i.e. coating thickness, apertures and geometry, a copper tape (Advance Tapes, AT526) was applied on the outside of the device's lid. The tape consists of a copper coating with a thickness of $(35 \pm 2)$ µm and an electrically conducting adhesive of $(15 \pm 2)$ µm on a substrate, where the latter is peeled off. The cross section is imaged in fig. 3.11a. In the following part of this section various configurations (see fig. 3.11) are tried to test the impact of:

- Maximum achievable shielding by completely encasing the sensor in a large sheet of the tape
- Apertures
- Grounding
- EMI radiated by the EMI test board

Just as outlined in the above section (section 3.3), the envelopes of the TEM cell spectra are plotted in fig. 3.12 for the shielding evaluation. We see that already the envelopes of the references, which are two different unmodified sensors, do not agree, sometimes by several dB. This is a manifestation of the electrical variation already discussed. Therefore, only general trends and large differences can be deduced. Furthermore, once the emissions get close to the noise level, it is impossible to quantify them further. This critical level lies between 2 dB and 5 dB, as can be observed in the spectra and envelopes.

**The copper sheet** is representing ideal conditions. It encloses the sensor completely (see fig. 3.11b). This avoids any gaps between individual copper pieces and can be easily grounded on the EMI board by just sticking it onto its metallic area, but of course in this configuration the sensor cannot operate as intended. Nevertheless, it provides an impression of the maximum achievable shielding, even though it can be outperformed by the second cutout, likely because of the grounding.

Next, the apertures were cut out of the copper sheet (see fig. 3.11c) without other modifications to show us the effect of the apertures. However, it can be

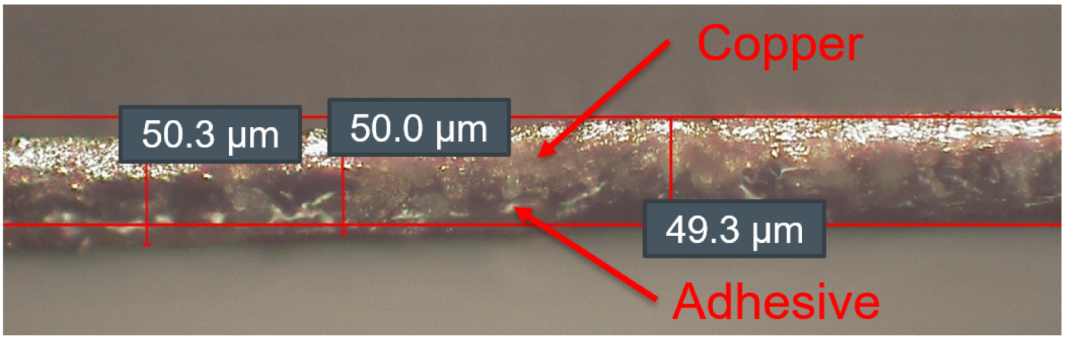


**(a)** Cross section of the copper tape.

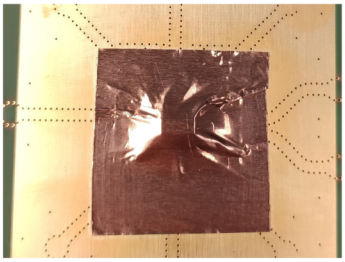

**(b)** Copper sheet, closed

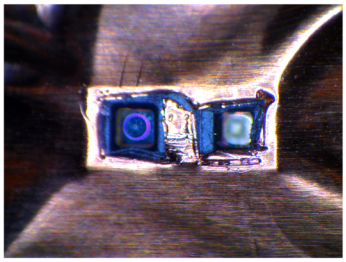

**(c)** Copper sheet, open

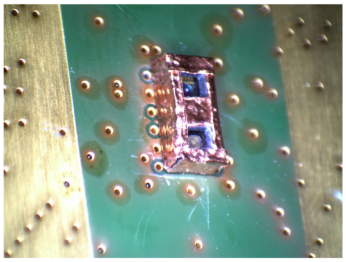

**(d)** Composite, open

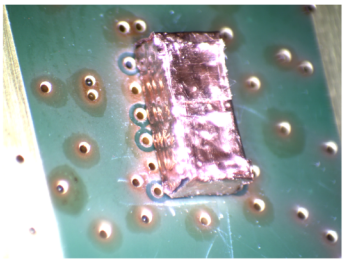

**(e)** Composite, closed

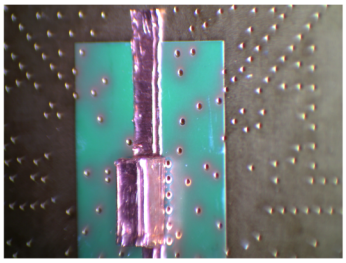

**(f)** Cutout 1, closed, grounded

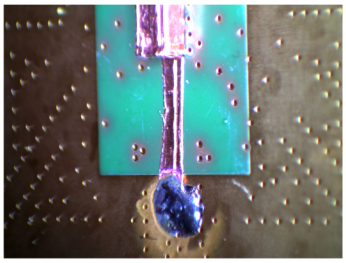

**(g)** Cutout 1, closed, soldered

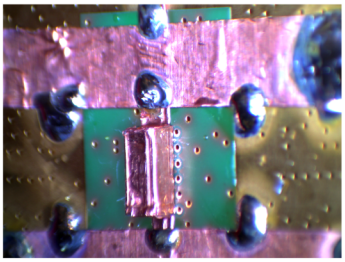

**(h)** Cutout 1, closed, soldered 2

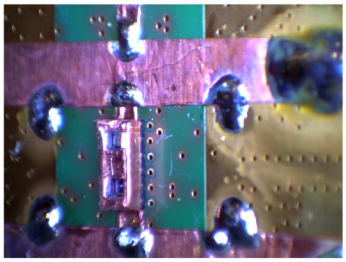

**(i)** Cutout 1, open, soldered 2

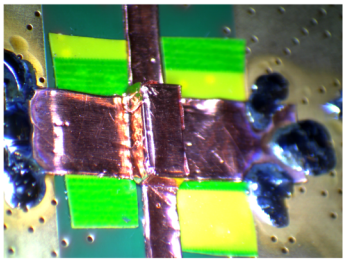

**(j)** Cutout 2, closed

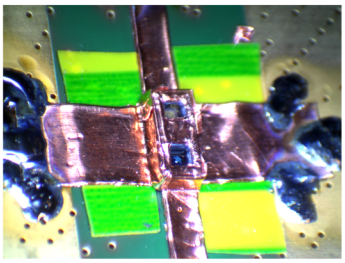

**(k)** Cutout 2, open

**Figure 3.11:** Copper tape for EMI shielding of a TOF sensor assembled in various configurations.

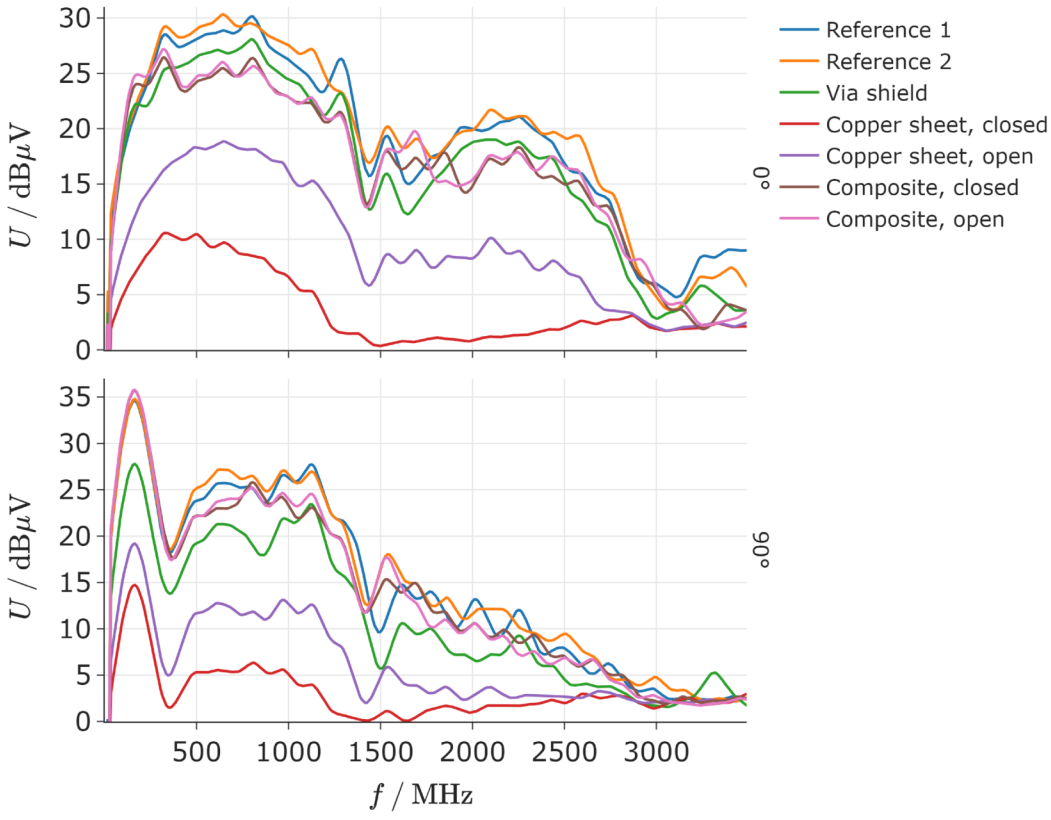


**(a)** Sheets and composite

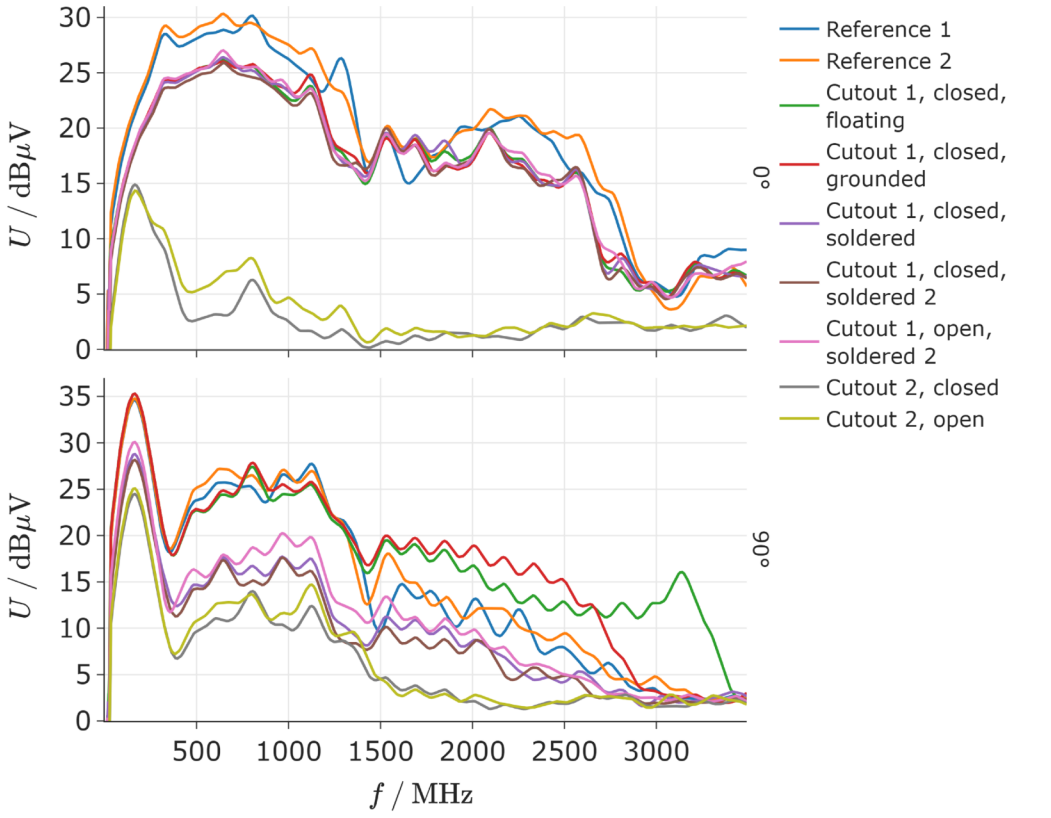


**(b)** Cutouts

**Figure 3.12:** Envelope of the TEM cell spectra of the TOF sensor shielded with copper tape in different configurations.

seen that the copper sheet between the apertures was ruptured on one side when removing the cutouts and their rectangular outline was not retained in the copper tape. It is obvious that opening the apertures has a major negative impact on the shielding, but there is still a significant attenuation retained when compared to the reference spectrum.

**The VIA shield** is an additional configuration not shown in fig. 3.11. It is a plane copper sheet that is applied over the green area of the EMI board with a slot for the sensor and it is supposed to shield the EMI radiated by the currents flowing in the board to the device. Since this has an obvious shielding effect, we can conclude that a certain portion of the TEM cell spectra are due to the currents outside of the device, which then also cannot be shielded by coating its lid.

**The composite structure** has the tape overlapping pieces on the top and on the sidewalls of the sensor, sparing out the apertures but also creating gaps between the vertical edges of the lid, as depicted in fig. 3.11d. The tape was not grounded, i.e. it remained floating. The conductivity between the pieces was measured with a multimeter and small needle probes. However, it was found to be so poor that it was necessary to use diode-check function instead of the resistance-measurement mode and even that did not result in proper conductivity between all parts of the applied copper. The envelopes show us that there now is a disparity between the 0° and the 90° degree spectra. While in the 0° orientation there is a recognizable shielding for most of the frequency range, this is only the case between 500 MHz and 1500 MHz.

Then, small pieces of the tape were applied covering the two apertures overlapping to small extent with the ones on the sensor's top (fig. 3.11e) to see if there is any improvement by closing the apertures. The copper remained floating and the conductivity was poor as well. The resulting envelope is hard to distinguish from the one of the open configuration, indicating that another factor is predominating, which likely is the lack of grounding.

**The first cutout** eliminates the influence of the electrical connection between individual copper pieces but retaining the closer fit to the lid, because a single piece was cut out of the copper tape and folded over the sensor. At first, the apertures were closed and the grounding was investigated. A larger strip leads on the top of the EMI board's surface to the bare metal for grounding (fig. 3.11f). The electrical connection to the EMI board's ground was checked with the multimeter again and this time also confirmed. We see that again there is a difference between the spectra. While in the 0° spectrum all configurations with the first cutout are close together, in the 90° orientation this is completely different. If, the copper tape is floating or only grounded via the conductive adhesive, there is even an increase EMI above 1500 MHz. Once, the cutout is soldered onto the test board (fig. 3.11g), however, the shielding becomes effective. Extending the soldering with the configuration fig. 3.11h, does not improve the situation notably. The emissions increase recognizably

but marginally if the apertures are cut out again as in fig. 3.11i.

**The second cutout** allows us to investigate the grounding further. It is depicted in figs. 3.11j and 3.11k. Because the orientation-dependent shielding of the first cutout could root in the directional manner it was grounded, the second cutout was therefore grounded and soldered on all four sides. In order to electrically isolate the signal pins which have vias in the near vicinity of the lid, those were covered with an insulating tape on top of which the copper tape can then be put safely. Furthermore, the seams on the vertical (w.r.t. the EMI board) edges were mostly eliminated by facilitating an overlap by folding additional copper tape pieces over them. The resulting shielding is exceptional. The EMI spectrum is mostly suppressed below noise level. It is also improving the 0° spectrum, which the first cutout could not. This is a strong indication, that if the grounding is done in a directional manner, the orientations are effected differently. Because the first cutout did so, while the second cutout was grounded on all four sides, the envelopes develop accordingly. The same effect occurs in the simulation (see chapter 4). Naturally, the overlapping edges could also impact this observation.
A direct comparison between these configurations and the copper sheet is plotted in fig. 3.13. It is evident, that the second cutout outperforms even the copper sheet in the 0° orientation and is on par with the open copper sheet in the 90° spectrum. It is unclear, how this is possible, since a large copper sheet as above should attenuate better than an (necessarily) imperfect cutout. Perhaps, the copper sheet must also be soldered onto the test board to improve the grounding on the cutout's level. Another possible explanation could be that the grounding of the cutout is simply better, because it is provided a better current path, e.g. closer to the surface of the test board, or that the emissions from the test board, which were seen to have an effect from the VIA shield, are counteracted better because of the proximate and parallel grounding strips.


**Figure 3.13:** Envelope of the TEM cell spectra of the TOF sensor shielded with copper tape in the configurations with the copper sheet and cutout 2.

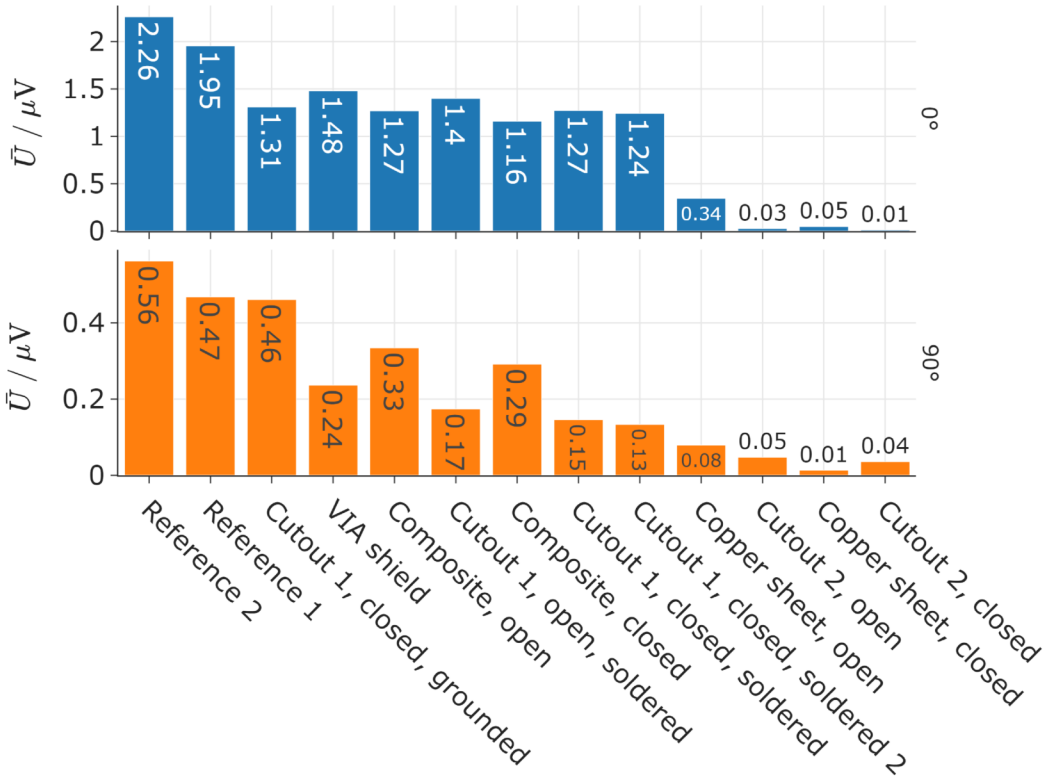


**Figure 3.14:** Equivalent voltage of the TEM cell spectra of the TOF sensor shielded with the copper tape in various configurations.

## 3.5 Coated Lids

In this section, the results of the TOF sensor that was shielded with the conductive coatings on the surface of its lid are discussed. The depositions are described in Chapter 2. The evaluation is according to section 3.3 and analogous to section 3.4.

First, the only SGP coating was considered. It was chosen to investigate the impact of the grounding quality on the TEM cell spectra, since it was the first coating to be available due to the assembly of the devices. In order to analyze this, devices with a large spread of resistances (see fig. 2.5) are used. As shown in figs. 1.1 and 2.3, the grounding of the sensor is only along the long axis. Hence, it is comparable to the first cutout from figs. 3.11f to 3.11i.

The envelopes are plotted in fig. 3.15 and the equivalent voltages in fig. 3.16. Identical to before, we see that the directional grounding causes the 0° spectrum to align regardless of the grounding quality and the 90° spectrum to separate into two groups of well and badly grounded devices. Devices can easily be assigned to one or the other group by their resistances. If they have a resistance that is significantly below the resistances of the uncoated sensors, the grounding is sufficient. Again, the badly grounded ones show an increase in EMI as compared to the references. Unfortunately, the performance of the well grounded ones is by far not as good as for the second cutout of the copper tape configurations (figs. 3.11j and 3.11k). This is a strong indication that the coated lids exhibit a limit in this order, either because of the grounding design or because of the coating thickness.

Secondly, all depositions were analyzed. For each material and thickness one to three devices with the lowest resistances of their group were measured. The envelopes are depicted in fig. 3.17 and the equivalent voltages in fig. 3.18. It is apparent, that it is impossible to distinguish between the individual coatings from the envelopes, apart from the sputtered coating SPUT4. Hence, it seems that the limit which was just mentioned is reached for the outsourced depositions. By extension, we cannot assess the effect of the coating thickness. This problematic is likely due to the grounding design.

Therefore, future investigations should be conducted on sensors with a structure that allow for grounding the coatings on as many places as possible and also try to reduce the electrical resistance of the conductive adhesive that is between them. It is highly likely that these two factors lift the limit to the level we see in the envelopes of the well grounded outsourced depositions.

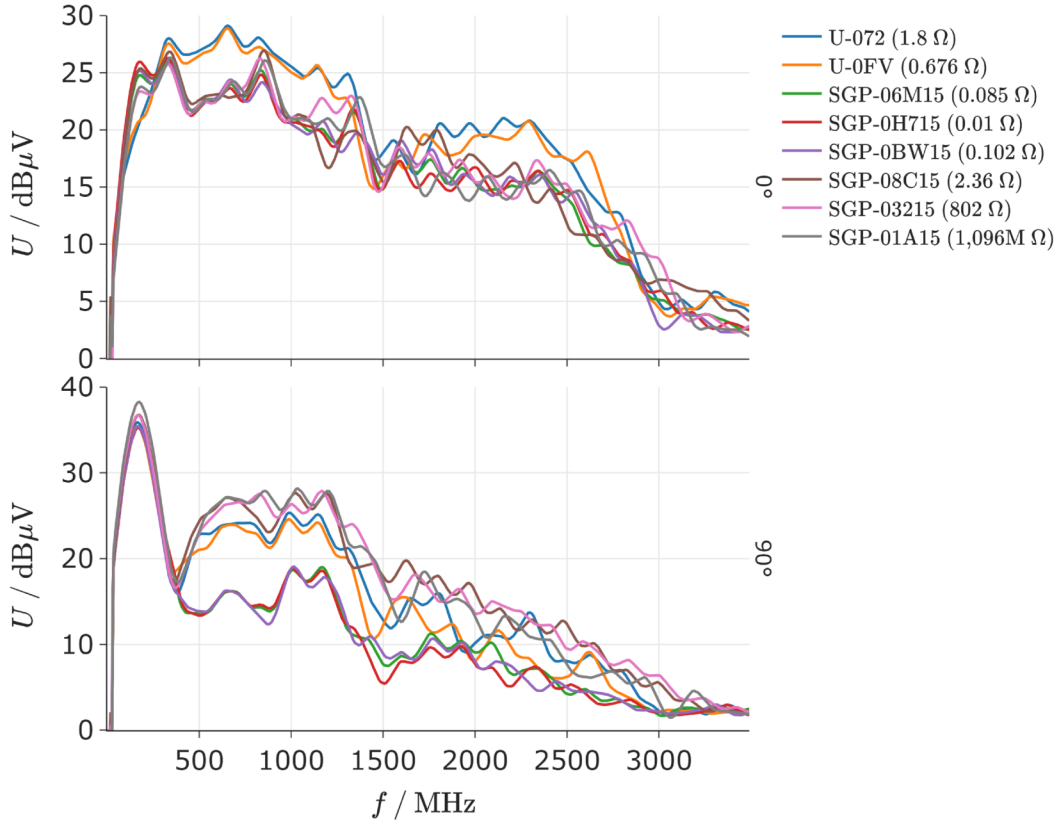


**Figure 3.15:** Envelope of the TEM cell spectra of the TOF sensor shielded with the SGP coating on its lid.

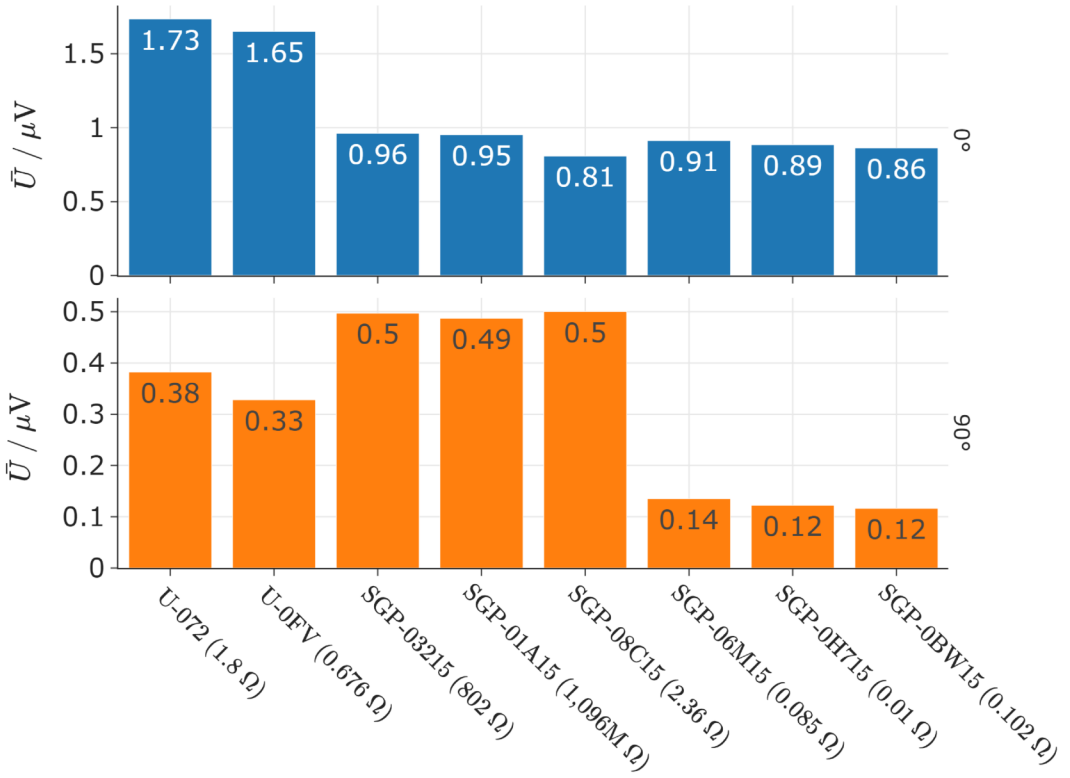


**Figure 3.16:** Equivalent voltage of the TEM cell spectra of the TOF sensor shielded with the SGP coating on its lid.

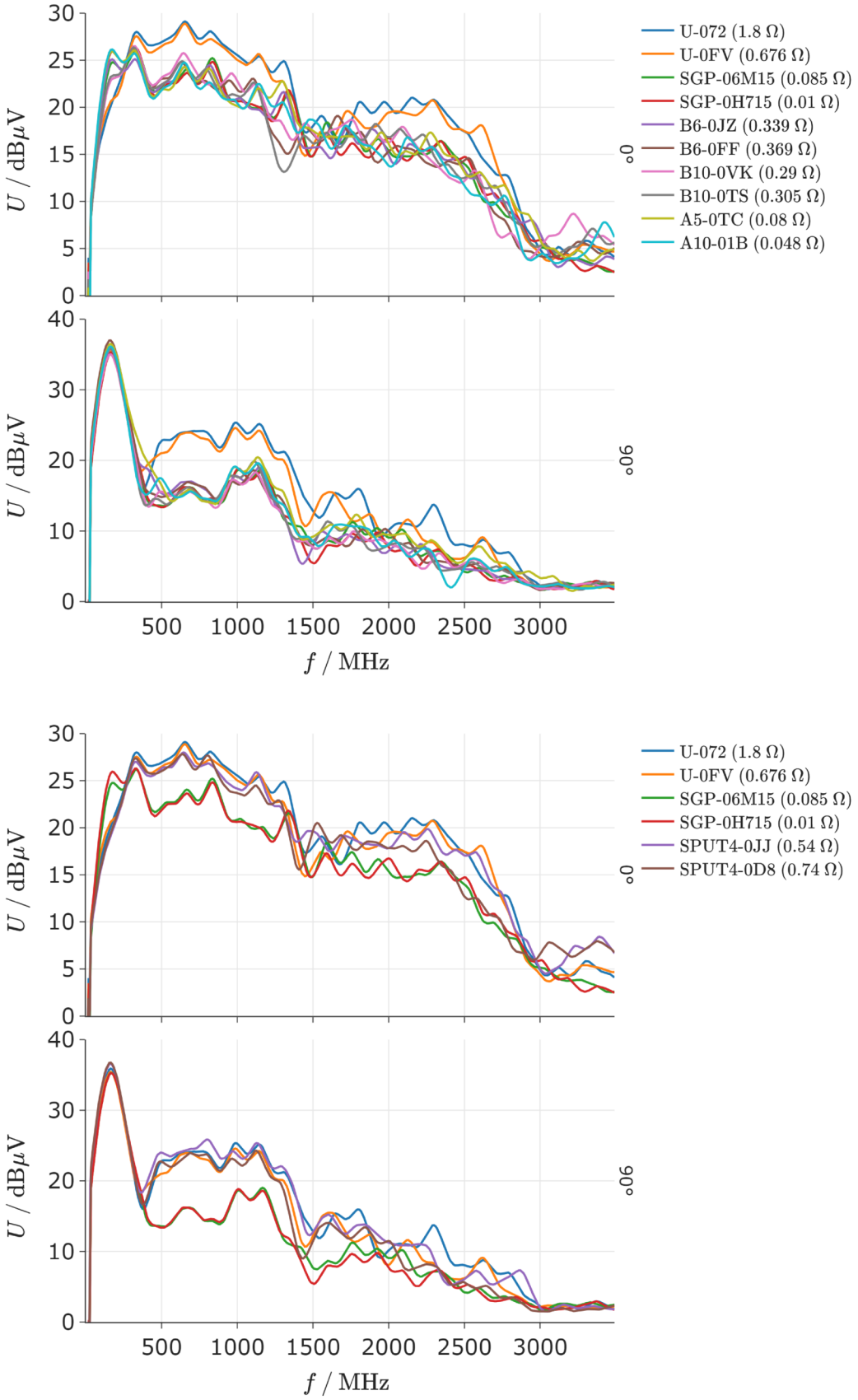


**Figure 3.17:** Envelope of the TEM cell spectra of the TOF sensor shielded with the conductive coatings on its lid. The sputtered coating is plotted separately.

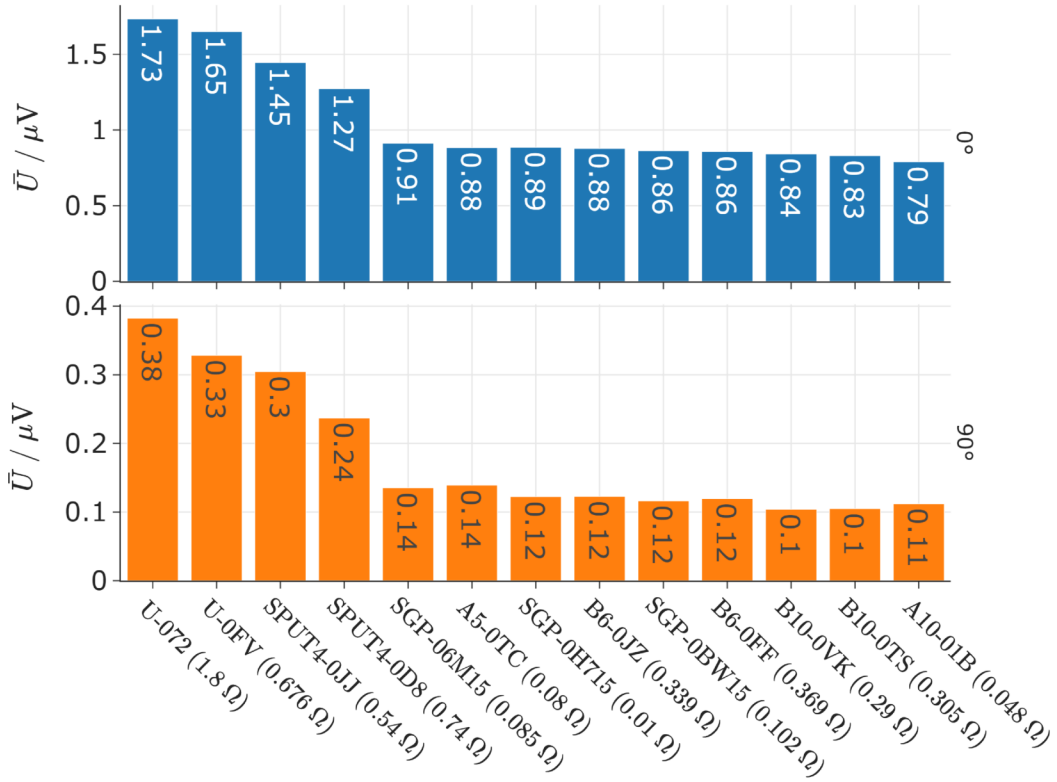


**Figure 3.18:** Equivalent voltage of the TEM cell spectra of the TOF sensor shielded with the conductive coatings on its lid.

## 3.6 Jittering the VCSEL Current

The sensors offer the possibility to jitter the VCSEL current. This means that the frequency with which the individual laser pulses are emitted is randomly varied. From section 1.1 we know that for non-jittered devices it is 17.7 MHz. From this process we expect that the frequency components of the current are smeared out and distribute over wider and thus smaller peaks in the TEM cell spectrum. The resulting spectra are plotted in fig. 3.19. We immediately see that it mainly affects the 0° spectrum, where it is indeed the case that the EMI is much more distributed. The large peaks become smaller and the measured value is now above the noise floor everywhere. The 90° spectrum is largely unaffected. This is an important observation, because only the VCSEL current is jittered. We can thus conclude that the VCSEL emissions are predominantly in the 0° and 180° spectra.

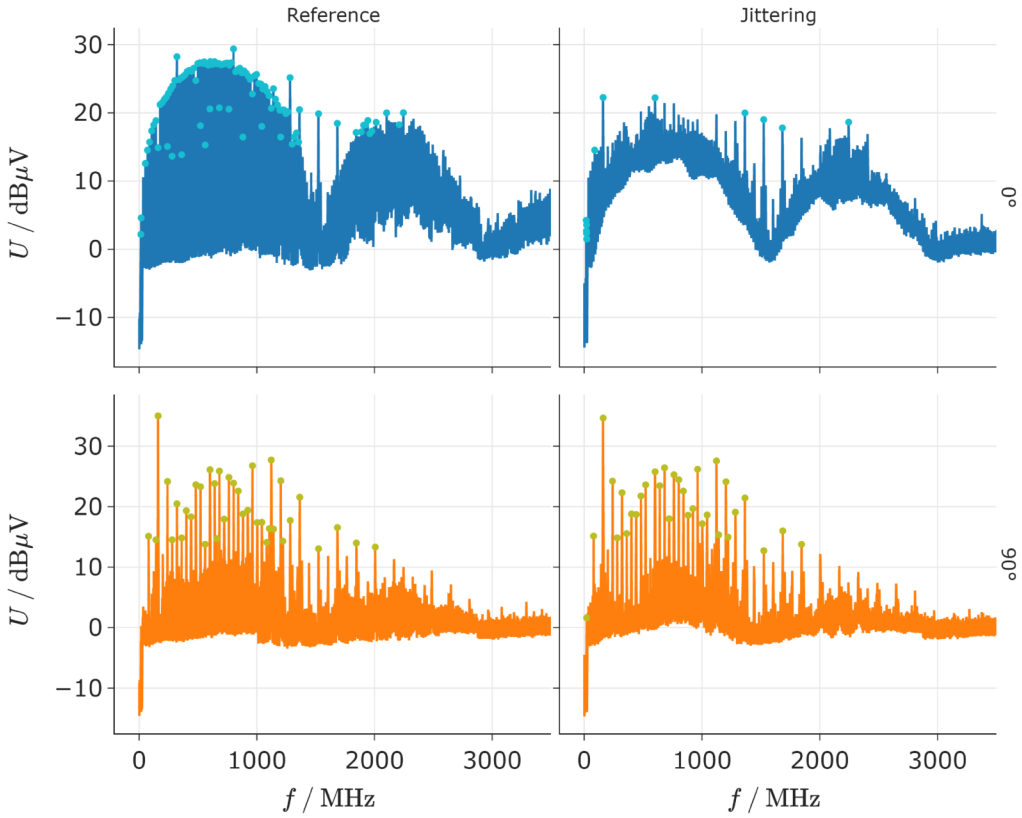


**Figure 3.19:** TEM cell spectra of the reference and the jittered TOF sensor.

## 3.7 Summary

First, the TOF sensor was shielded with a 35 µm thick copper tape in different configurations, the devices measured in the TEM cell and the resulting spectra compared via their envelopes in fig. 3.12. These observations are also reflected by the equivalent voltages in fig. 3.14, which are calculated according to eq. (3.1) and are a measure for the integral of the EMI spectra. There is a significant variation of the EMI for the two reference devices. In the 0° spectra there are two groups of shielded configurations: Those that don't have a grounding along the short axis of the sensor (the composite structure and the first cutout), and those that do (the copper sheet and the second cutout). The latter group exceptionally reduces the EMI. Notably, the second cutout is better than the copper sheet. On the other hand, in the 90° spectrum, there is a much more gradual reduction, depending on the extent of the grounding.

One core observation we can deduce is that if the grounding is good enough, the EMI is reduced almost completely, even with open apertures. Another is that if the grounding is directional like in the first cutout, only one orientation is shielded well and the other one is performing as if the shield is floating, which is identical to the simulations (see chapter 4). If the grounding is insufficient, e.g. if the copper tape is just connected to the test boards ground via the conductive adhesive, it is again comparable to a floating configuration. Nevertheless, a floating shield also reduces the EMI to small extent. The VIA shield impacts the spectra positively as well, already shielding a significant portion of the EMI, which therefore must be coming from the EMI board. This effect occurs especially in the 90° orientation, where it reduces the largest peak at 160 MHz notably.

Secondly, the coated lids were used as shields. It was determined that there is no meaningful ranking of the different materials and thicknesses possible, apart from the sputtered coating SPUT4, which was significantly worse than the other group. That is likely due to the grounding design of the sensor, as it might set a lower limit of the EMI which we see in the envelope spectra. Future studies, thus, must improve that in order to make more assertions on the impacts of coating material and thickness.

Nevertheless, shielding the TOF sensor with the coating lids, it was possible to reduce the equivalent voltage by as much as 54 % and 71 % for the 0° and 90° orientations respectively.

chapter 5 an argument is made why the grounding quality is mainly affecting the 90° spectrum and why this orientation benefits most from the coated lids.

# Chapter 4

# Simulation

The governing equations for electromagnetic computations are always Maxwell's equations (eq. (1.1)). They are coupled differential equations that create the complexity which makes it impossible to find closed form solutions for all but the simplest geometries and plane waves. E.g. Arnoldus and Berg [1] treat a dipole radiation source in the vicinity of a plane slab of material and find integrals for each point in space. However, numerous integrals must be calculated and the focus of this thesis should not lie on numerics.

Yet, there are theories that apply assumptions and simplifications which allow to calculate at least approximate field values by setting boundary conditions which then enable regions to be excluded from the computation in order to make the task solvable. For good conductors, this approach is called SIBC and is explained in detail in [22].

However, most practice-oriented projects employ simulation suites to avoid these problems and take advantage of the computational power that is commonly available. This is also the tool which I chose to get theoretical values for the shielding. The core strategy in contrast to analytical solutions is outlined in [14] and an overview of the simulation's principle used to solve Maxwell's equations is provided in [16]. A huge advantage is that simulations are geometry-independent and therefore immensely flexible. They employ meshing to discretize space and then step either in time or frequency to solve the required differential or integral equations. I employed "ANSYS® Electromagnetics Suite, Release 2020 R2" (HFSS) for the task of computing the EMI of the TOF sensor. A host of other programs including many open-source codes are applicable. An overview of the ones available and their principle is given in [18, 5].

Unlike in chapter 3, we can now calculate the SE via eq. (1.38) by comparing the spectra of a shielded configuration and a reference without shield. This allows us to investigate the maximum achievable shielding, as well as the impact of the grounding and apertures, like in the trial with the copper tape in section 3.4.

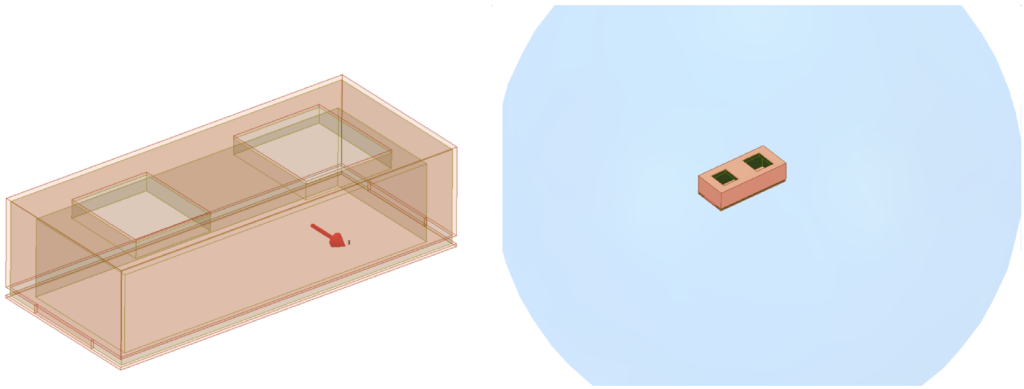

**(a)** Magnetic dipole source **(b)** Evaluation sphere

**Figure 4.1:** Setup for the simulation of the EMI shielding of a TOF sensor in HFSS. The radiation source is a magnetic dipole underneath one of the openings and the red arrow is its magnetic dipole moment. For the shielding, the Poynting vector is evaluated on the surface of a sphere with a radius of 15 mm and compared to a configuration without shield.

## 4.1 Setup

The setup is illustrated in fig. 4.1. A magnetic dipole was used as source and a harmonic behavior was assumed by HFSS to compute the EMR for one frequency at a time. The source is located at the origin and the magnetic dipole moment points in the X direction (see fig. 4.1a). Its amplitude is set to 1 A m, although this cancels in the SE due to the linearity of the system. HFSS calculates the Poynting vector (eq. (1.6)) and averages it over the surface of a sphere with a radius of 15 mm centered at the origin (see fig. 4.1b). A meshing length of 3 mm was forced on this surface which improves the calculation of the fields on it. As for the geometry, only a drastic simplification of the real dimensions of the sensor in general, including its LCP lid, was used. In essence, it was a rectangular box open on the bottom with cutouts on top. No additional interior components were modeled. In the reference configuration, only the LCP lid was assigned a material with typical values for epoxy: non-conductive, non-magnetic, a relative permittivity of 4.2 and a loss tangent of 0.2. The latter is defined as

$$\tan\delta = \frac{\sigma - \omega\Im\epsilon}{\omega\Re\epsilon} \approx \frac{\Im\epsilon}{\Re\epsilon} \tag{4.1}$$

which simplifies to the negative fraction of the imaginary over the real part of the permittivity for non-conductive materials and is a measure for the absorption of the material. The shielding material was copper with a conductivity of $5.8 \times 10^7\,\mathrm{S\,m^{-1}}$ and a slight relative permeability of 0.999 991.

The configurations are depicted in fig. 4.2. The reference configuration (fig. 4.2a) considered only the LCP lid. The shielded configurations (figs. 4.2b to 4.2g) had a copper layer of 35 µm on the outside of the lid. This is supposed to represent the experiments with the copper tape. The ground plane and the shield were still modeled in the reference, but had vacuum assigned to it in order to have HFSS create the same mesh for all configurations.

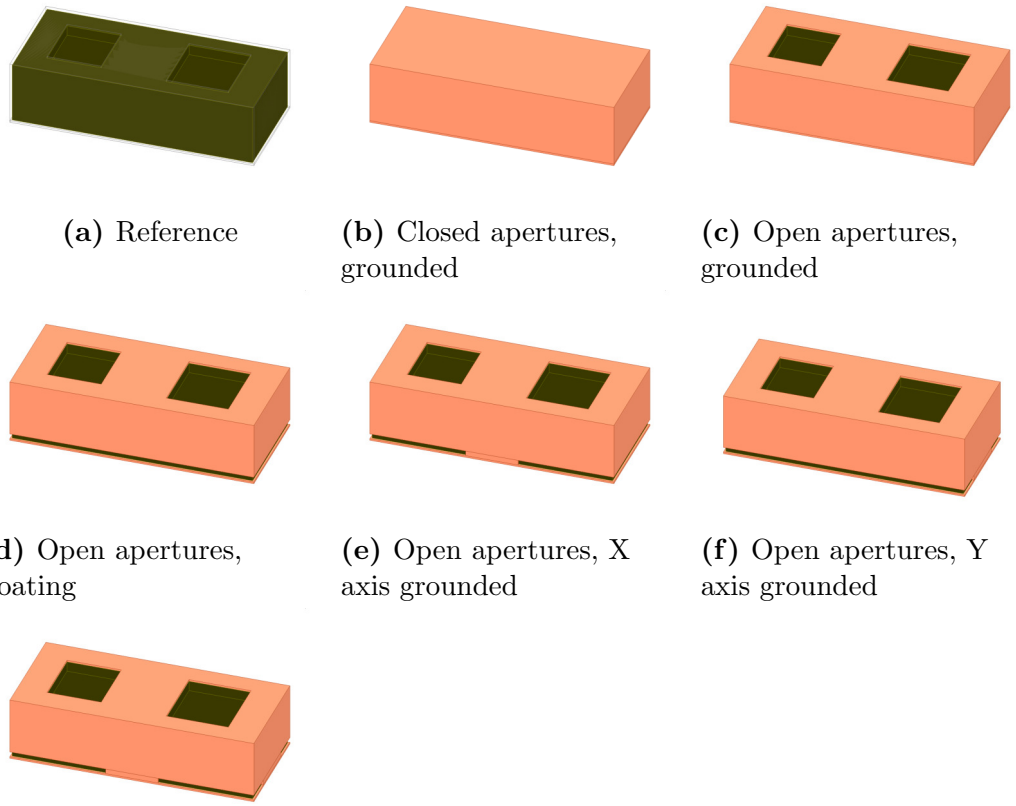

**(a)** Reference

**(b)** Closed apertures, grounded

**(c)** Open apertures, grounded

**(d)** Open apertures, floating

**(e)** Open apertures, X axis grounded

**(f)** Open apertures, Y axis grounded

**(g)** Open apertures, X and Y axis grounded

**Figure 4.2:** Configurations for the simulation of the EMI shielding of a TOF sensor in HFSS. The shield consists of 35 µm thick copper on the outside of a LCP lid and on its ground plane.

The shielded configurations consider the following:

- fig. 4.2b completely encloses the sensor to evaluate the maximum achievable shielding.
- fig. 4.2c spares the apertures, but still is grounded on all sides.
- fig. 4.2d removes the benefit of the grounding.
- fig. 4.2e is only partially grounded along the X axis of the model.
- fig. 4.2f is only partially grounded along the Y axis of the model. This configuration is comparable to the actual sensor, because there the grounding is also along the corresponding (long) axis.
- fig. 4.2g is grounded only partially grounded along both the X and the Y axis of the model.

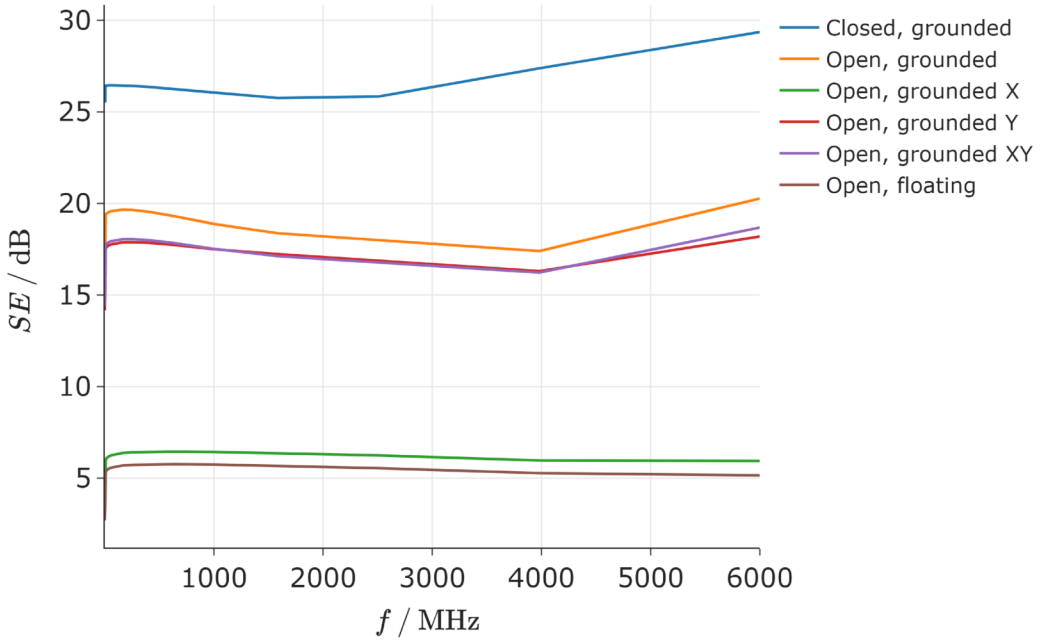


**Figure 4.3:** SE of a copper layer of a thickness of 35 µm on the outside of the TOF sensor simulated in HFSS.

## 4.2 Results

The resulting SE is depicted in fig. 4.3. For all configurations, the SE stays quite flat for the biggest part of the frequency range. Above approximately 2.5 GHz it starts to rise.

The completely grounded and closed model achieves a SE of 25.5 dB to 29.3 dB. By opening the apertures this is reduced by 6.7 dB to 10 dB resulting in 16.6 dB to 20.3 dB in total. If additionally the device is floating, only 2.7 dB to 5.7 dB can be shielded.

The partially shielded configurations show an interesting behavior. The configuration that is grounded along the X axis is barely an improvement compared to the completely floating one. On the other hand, the configurations that are grounded along the Y axis show a SE comparable to the completely grounded one with 14.2 dB to 18.2 dB. Notably, they are practically identical.

As a conclusion, we can say that for shielding EMR due to a magnetic dipole source there needs to be a grounding in the plane perpendicular to its magnetic moment. If that is not the case the grounding is ineffective and the shielding is closer to a floating configuration. One hypothesis, which will be investigated in more detail in the next chapter (chapter 5), is that for effective shielding there needs to be a current loop possible with a corresponding magnetic dipole moment parallel to the magnetic dipole source's. What we consequentially saw in this chapter is that if there is only a single magnetic dipole source as well as a grounding that possesses a direction, e.g. is only along one axis, one combination is much more effective than the other.

Note that in the scope of this short experiment, the shield always was on the

outside of the lid. This was used on purpose, since there is no interior due to the hugely simplified model. Hence, if the shield was on the inside of the lid, there would be nothing that could absorb the EMR that is reflected by the metal but itself. This could lead to some unwanted behavior and could deviate too much from the real setting, since it is expected based on the theory in chapter 1 and the literature that the dominant effect of a metal shield would be the extension of the light path due to multiple reflection and the subsequently increased absorption. This should then not be possible. Nevertheless, it would be interesting to check the SE of the analogous configurations with the shield on the inside, as it is the case in the real sensor. A remedy could be to include some simplified absorber in the simulation or model the sensor in more detail. The latter approach should then include all kinds of materials that absorb EMR, if only by a small amount.

Furthermore, different dipole and grounding orientations could be simulated. Especially, the effect of an electric dipole with its moment in the Z axis (up) should yield worthwhile insights. This is stated in view of the hypothesis developed in chapter 5 based on [12] that only three dipoles produce the measured spectra in the TEM cell: Two magnetic dipoles with moments in the X and Y axes in my simulation model and an electric one in the Z axis. With the help of the simulation here the shielding of the corresponding dipoles could then be investigated in terms of grounding, apertures and total shielding.

Naturally, a simulation enables one to look at many more different aspects, which aren't evaluated in the scope of this thesis, such as the effects of:

- Aperture size, location, and form.
- Seams or openings in the shield, e.g. in the sidewalls of the sensor or in the ground plane for electrical connections.
- Coating thickness. E.g. is there a minimum thickness below which the SE decreases significantly?
- Field propagation inside the shield. It could include the interactions between fields irradiated back at the sensor from the outside (such as is expected in the TEM cell). Of course, for that the whole environment needs to be modeled in the simulation too. Having that, it would be another crucial insight to check if the fields that build up outside of the shield in the TEM cell that are responsible for the measurements are indeed as outlined in [12]. Particularly, the characteristics of the EMR should be investigated, i.e. is it close to dipole radiation in the far field or is there a deviation? If so, up to which order (quadrupole,... ) is it significant?
- The spacial geometry of the sources. All EMR is created by currents in the sensor. The shape of the paths or loops should have an impact, especially in terms of the aforementioned fields in the TEM cell. A worthwhile finding would be how their geometry alters the radiation portions (dipole, quadrupole,...) in the TEM cell and also their corresponding moments. This could open the possibility to predict the SE and the

TEM cell measurements. The basic steps for that would be: First, evaluate the source moments given the current paths. Secondly, compute the SE given the shield and the source moments. Finally, calculate the measurement results in the TEM cell.

- Current paths inside the shield. As mentioned before and hypothesized in chapter 5 the distinct SE of the different grounding directions that we saw here could be due to the necessity of current paths in the shield. Consequentially, it should be investigated in the simulation if this is in fact the correct physical picture. Moreover, it could be examined how openings in the shield, e.g. due to the apertures, that change the possible current paths effect the shielding.

Obviously, knowledge about these effects would be immensely valuable for the development process of electronic devices. EMI measurements in the TEM cell could be evaluated beforehand. Possibly, even design rules can be derived or improved to avoid expensive design changes.

# Chapter 5

# Dipole Model

To find a theoretical model which allows us to calculate the electromagnetic fields inside the TEM cell is, unfortunately, impossible due to the complexity of the measurement system. That would be the best case scenario, since it would enable us to calculate the shielding and the measurement results. Predicting that is, naturally, highly beneficial for electronic design to ensure compliance to EMC standards beforehand. Also, shielding aspects could be evaluated with ease.

To make the description manageable, one approach is to simplify the nature of the measurement system by introducing mutual capacitive and inductive coupling between the device and the transverse electromagnetic (TEM) cell. In this model, the fields are not calculated and the device essentially represents a black box whose transfer function is determined by the coupling coefficients. The values measured in the EMI test receiver are then evaluated in turn via another model for the TEM cell.

A different approach, which in my opinion keeps more to the physical fundamentals, is proposed in [21]. Wilson models the emissions of the device by six harmonic multipoles for each frequency: Three magnetic and three electric. Furthermore, a method to extract their multipole moments is developed by inserting the DUT in different orientations into the TEM cell, where the number of necessary measurements depends upon the knowledge about which emissions dominate. Importantly, he argues that the multipoles can be approximated by dipoles and uses only their *far field*. This is possible, because due to the geometry of the TEM cell, which ideally should be just a flared up transmission line, only TEM modes are able to build up and subsequently to be measured. Therefore, the near field part is filtered out, even though according to eq. (1.34) it still should be included due to the proximity of the measurement system to the radiation source. This is thus limited to measurements in the TEM cell like in chapter 3. Pan et al. [12] build upon this foundation and show that three dipoles are negligible if a large ground plane is present closely below the DUT. This might be due to image charges being able to compensate the radiation belonging to those. Hence, the electric dipoles parallel and the magnetic one perpendicular to the ground plane are omitted. Moreover, the method introduced in [12] reduces the number of measurements in different

orientations in the TEM cell necessary to evaluate the dipole moments by using a hybrid. In this setup, both connections at the TEM cell are connected to the hybrid, i.e. the termination impedance is not used. By evaluating the difference of the two signals, the magnetic dipole moments can be calculated, and by using the sum, we get the electric dipole moment. In total, only two different orientations of the DUT are sufficient. That makes it feasible to use with the TEM cell and EMI test board that was used in the scope of this thesis (see chapter 3).

It is important to stress that, even though only the far field modes are measured in the TEM cell, the other parts also contribute to EMI in a different environment, e.g. in the actual application. Furthermore, it is expected that they cannot be neglected for the shielding mechanism, regardless of the setup. That idea might be conceptualized by considering the device with the shield as a subsystem in which the near field is important. The EMI, which is emitted by it, is filtered according to the properties of the environment.

According to the best my knowledge at the time of writing this thesis, there is no paper available that checks the approximation of neglecting the near field and the multipoles of higher orders inside the TEM cell. Since that is essential to the papers outlined above, it would be highly beneficial to do so, e.g. in a simulation as mentioned before in chapter 4. There, it is possible to look at the fields and compare them to the fields expected according to the equivalent dipoles (see section 1.2.6). Nevertheless, the results and the precision with which they predicted the measured spectra in the TEM cell via the dipole model speak for themselves.

Naturally, the knowledge that this model creates is a crucial improvement. E.g. one could look at the dipoles with the highest moments and possibly trace them back to electrical components, like bond wires which should be akin to magnetic dipoles or capacitors which should be comparable to an electric dipole. In the best case scenario, culprits can be singled out and eliminated. It is important to stress that this model still treats the DUT as a black box. However, the dipole sources are physically motivated, whereas using the inductive and capacitive coupling coefficients is elevated by one layer and completely omits the nature of the EMR sources.

## 5.1 Predicting VCSEL Emissions

An electronic component which is expected to have one of the largest EMI emissions is the VCSEL. It needs a huge current to supply the power necessary for the strong laser light that enables the functionality of the sensor with distant objects and in bright environments. In the following, the corresponding TEM cell measurements are predicted. This process is outlined in fig. 5.1.

First, the VCSEL is modeled as a single bondwire, because those resemble large loops and it is assumed that the VCSEL bondwire is, in combination with the large current flowing through it, the preponderant origin of EMI emissions. In fig. 5.2 a schematic of the bondwires is depicted. Hence, a bondwire on a

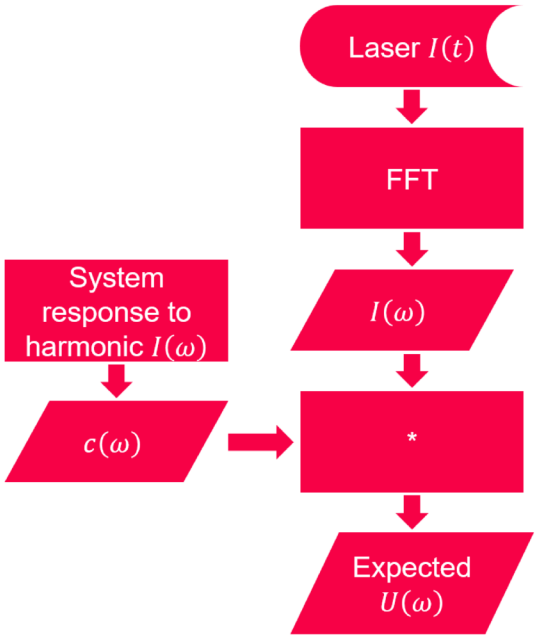


**Figure 5.1:** Process for predicting the VCSEL measurements in the TEM cell with the bondwire antenna.

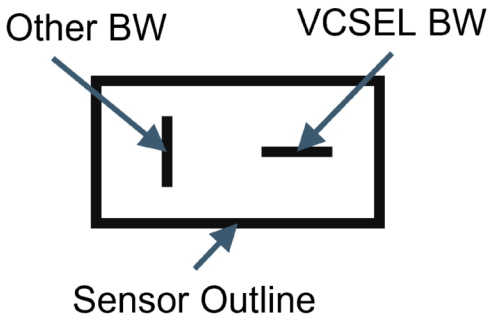


**Figure 5.2:** Schematic of the bondwires in the TOF sensor.

PCB was inserted into the TEM cell and operated with a sinusoidal signal of a single, harmonic frequency at a time (see fig. 5.3). The current through the bondwire antenna was calculated and the measurement system response to the produced EMI emissions was evaluated.

Secondly, the resulting coefficients were used to predict the expected TEM cell measurements by multiplying them with the frequency component of the VCSEL current, or rather its square. The latter was extracted from the VCSEL current as a function time via a FFT whose definition is given in eq. (A.3).

### 5.1.1 TEM Cell Gain

In this section, the response of the measurement system of chapter 3, i.e. the TEM cell, coaxial cable and EMI test receiver, is determined. This was done by coupling a harmonic frequency into the TEM cell. As a source, a single bondwire on a custom PCB similar to the EMI board was used. The bondwire

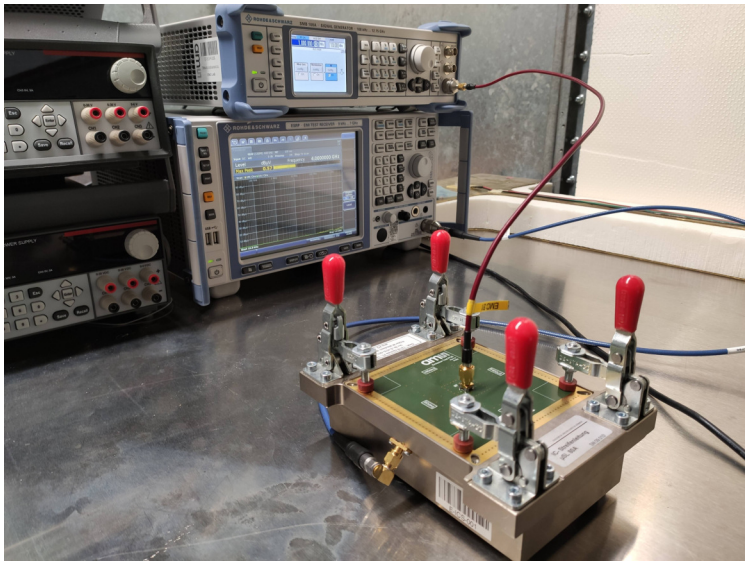

**(a)** Overview

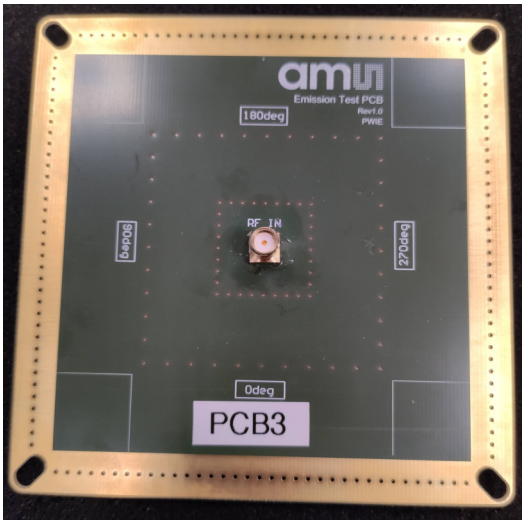


**(b)** Bondwire PCB, top side

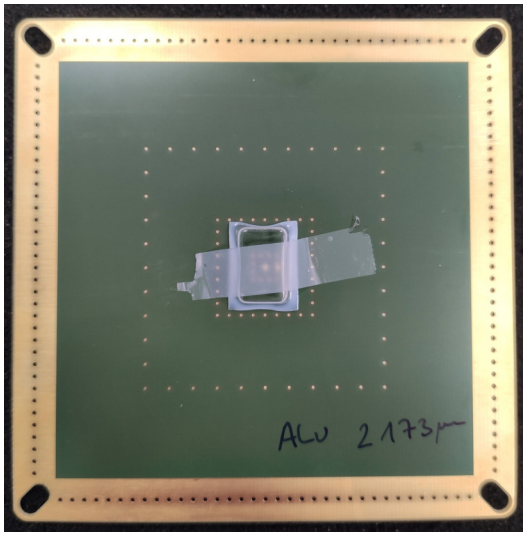

**(c)** Bondwire PCB, bottom side

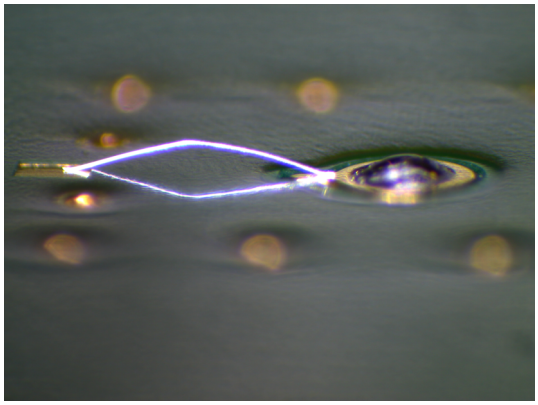

**(d)** Bondwire antenna

**Figure 5.3:** Setup for the measurements of the gain of the TEM cell with the bondwire PCB.

**Table 5.1:** Setup for the measurements of the TEM cell gain.

| Device | Manufacturer | Type | Description |
|---|---|---|---|
| EMI test reciever | Rohde & Schwarz | ESRP7 | Frequency range: 9 kHz to 7 GHz |
| TEM cell | Ingenieur-Dienstleister Körber | $\mu$SL 80A | Terminated with a 50 Ω impedance. |
| Signal generator | Rohde & Schwarz | SMB 100A | Frequency range: 100 kHz to 12.75 GHz |
| Bondwire PCB | ams-OSRAM AG | | Bondwire material: Al bondwire length: 2173 µm |
| Input coaxial cable | | | Internal number: EMC 31 |

forms a loop in a plane perpendicular to the PCB. It is aluminum and has a bonding length of 2173 µm. The setup is depicted in fig. 5.3 and summarized in table 5.1. The bondwire antenna was driven by a signal generator which was connected to the bondwire via a coaxial cable. The measurements were taken again with the EMI test receiver, which recorded the spectrum in the same range as before (1 MHz to 3500 MHz). The peaks in this spectrum were then detected, where the largest one was used for the evaluation here and the harmonics that arose due to the imperfection of the sinusoidal signal were neglected (they are many orders of magnitude lower). The peak voltage was recorded and the procedure was then repeated for each frequency of interest. Here, frequencies ranging from 1 MHz to 3500 MHz were scanned in (mostly) 200 MHz intervals. Afterwards, the bondwire was rotated in the TEM cell, which yielded different measurements depending on the orientation. Again, 0°, 90°, 180° and 270° are possible. At 0° and 180° the bondwire was perpendicular to the stripline and its equivalent magnetic dipole moment was parallel to it. At 90° and 270° this was inverse. The total system, consisting of the bondwire source and the measurement subsystem of the TEM cell and test receiver, was analyzed by relating the input (current amplitude) to the output (peak voltage) for each frequency and orientation.

This evaluation is based upon two fundamental assumptions: First, the power which is radiated by the bondwire is proportional to the square of the current amplitude:

$$P_{rad}(\omega) \propto I^2(\omega) \tag{5.1}$$

Secondly, the square of the measured voltage is proportional to power radiated by the bondwire:

$$U^2(\omega) \propto P_{rad}(\omega) \tag{5.2}$$

They can be chained together and the coupling coefficients between the source and the measurement system $c(\omega)$ are introduced:

$$U^2(\omega) = c(\omega) I^2(\omega) \tag{5.3}$$

Initially, it was the purpose of this experiment to simply check whether

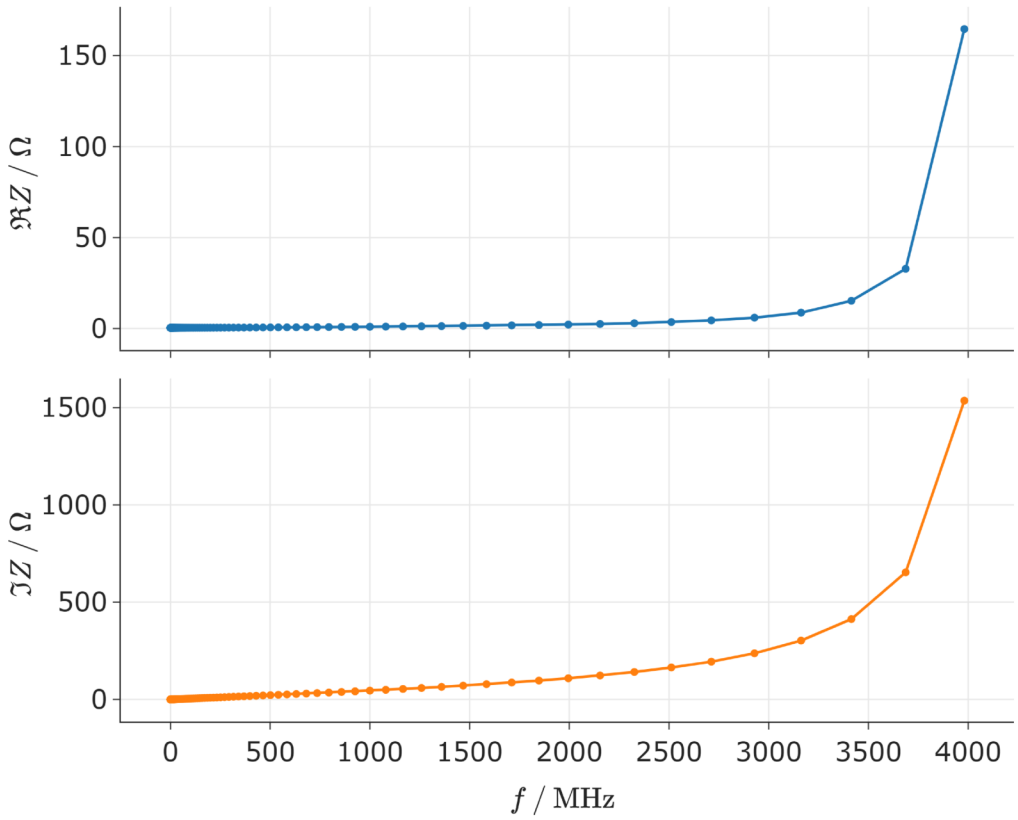


**Figure 5.4:** Impedance of the bondwire used as source for the TEM cell gain study. Top: real part. Bottom: imaginary part.

the system is indeed linear. But, since the harmonics measured for a single driving frequency was negligible, this was confirmed, at least in the sense that no additional frequencies arose. A meticulous continuation could review this by recording the signal, applying a FFT to get the frequency components and comparing them to the measured peaks here. Furthermore, one should investigate how the output scales with the input, e.g. half the current and observe how the measured voltage behaves. Theoretically, any linear system possesses the superposition property, but the inverse conclusion is not necessarily true.

To evaluate the coefficients which relate the output (measured peak voltage at the test receiver) to the input (amplitude of the sinusoidal current through the bondwire) for each frequency, both need to be known, of course. Unfortunately, the signal generator did not offer the possibility to act as a current source with a set amplitude. Instead, a fixed (apparent) power of 10 dBm was applied. Hence, the current through the bondwire antenna was calculated from the power via the impedance. The impedance was simulated in the TEM cell by ams-OSRAM AG and the values are plotted in fig. 5.4. With the impedance and the apparent power $S$, the current is calculated according to

$$I(\omega) = \frac{2S}{|Z(\omega)|} \tag{5.4}$$

where the factor of two allows us to immediately get the amplitude instead of the RMS.

Now everything is in place to compute the coupling coefficients. The result is depicted in fig. 5.5. An obvious property they exhibit is that they are identical for the 0° and 180° as well as for the 90° and 270° orientations respectively, which is what we saw before in chapter 3 for the spectra. Moreover, we recognize that the coefficients for the 90° orientation are much higher than those for 0°, where the ratio of their maxima is more than 17. This is a crucial observation, because we thus can conclude that the TEM cell receives a much higher signal when the bondwire is orientated such that its magnetic dipole moment is perpendicular to the stripline. In these orientations, the maxima of the far field dipole radiation pattern point towards the connectors of the TEM cell (see section 1.2.6). This is a clue that the far field dipole model is indeed the right picture. It also tells us that if we insert an actual electrical component with an array of bondwires in perpendicular orientations as in fig. 5.2 into the TEM cell, the ones with a magnetic dipole moment parallel to the stripline contribute negligibly to the measured voltage. If they are arranged such that their magnetic dipole moment is either parallel or perpendicular to it, like it is the case in fig. 5.8, one set is selected for a given orientation of the DUT in the TEM cell. That is of course only true if the actual bondwires, which can have different geometries and lengths, have comparable coupling coefficients as the one used here.

In a next step, one could try to model the coupling coefficients in a simulation of a perfect dipole source in the far field with the dipole moments extracted from TEM cell measurements with a hybrid, as mentioned above. Thus, it could be investigated if a bondwire indeed behaves like a dipole in the far field, as discussed in [21, 12].

### 5.1.2 VCSEL Current

Here, the remaining steps of fig. 5.1 are conducted, i.e. using the VCSEL current in combination with the coupling coefficients from the previous section to predict the TEM cell measurements.

The VCSEL driver current was again provided by ams-OSRAM AG from a simulation of the sensor's IC. One pulse is depicted in fig. 5.6. A FFT (according to eq. (A.3)) was applied to extract the frequency coefficients, i.e. to map the current into the frequency domain, and the magnitude of them are plotted in the same figure. As mentioned in section 1.1, it operates with a fundamental frequency of 17.7 MHz. Hence, the current has only non-zero values at multiples of it. We recognize that it decreases with frequency approximately linearly until 3000 MHz, where it has a smaller bump.

According to the procedure outlined above, we can now multiply the square of the current's frequency component with the coupling coefficients in fig. 5.5. We need to use the 90° coefficients, because there the bondwire is appropriately orientated. The coefficients are linearly interpolated in order to get values for multiples of 17.7 MHz. The result is depicted in fig. 5.7, where it is compared with the 0° TEM cell spectrum of an unmodified TOF sensor. It is necessary to use the 0° spectrum, because we know from section 3.6 that the EMI due

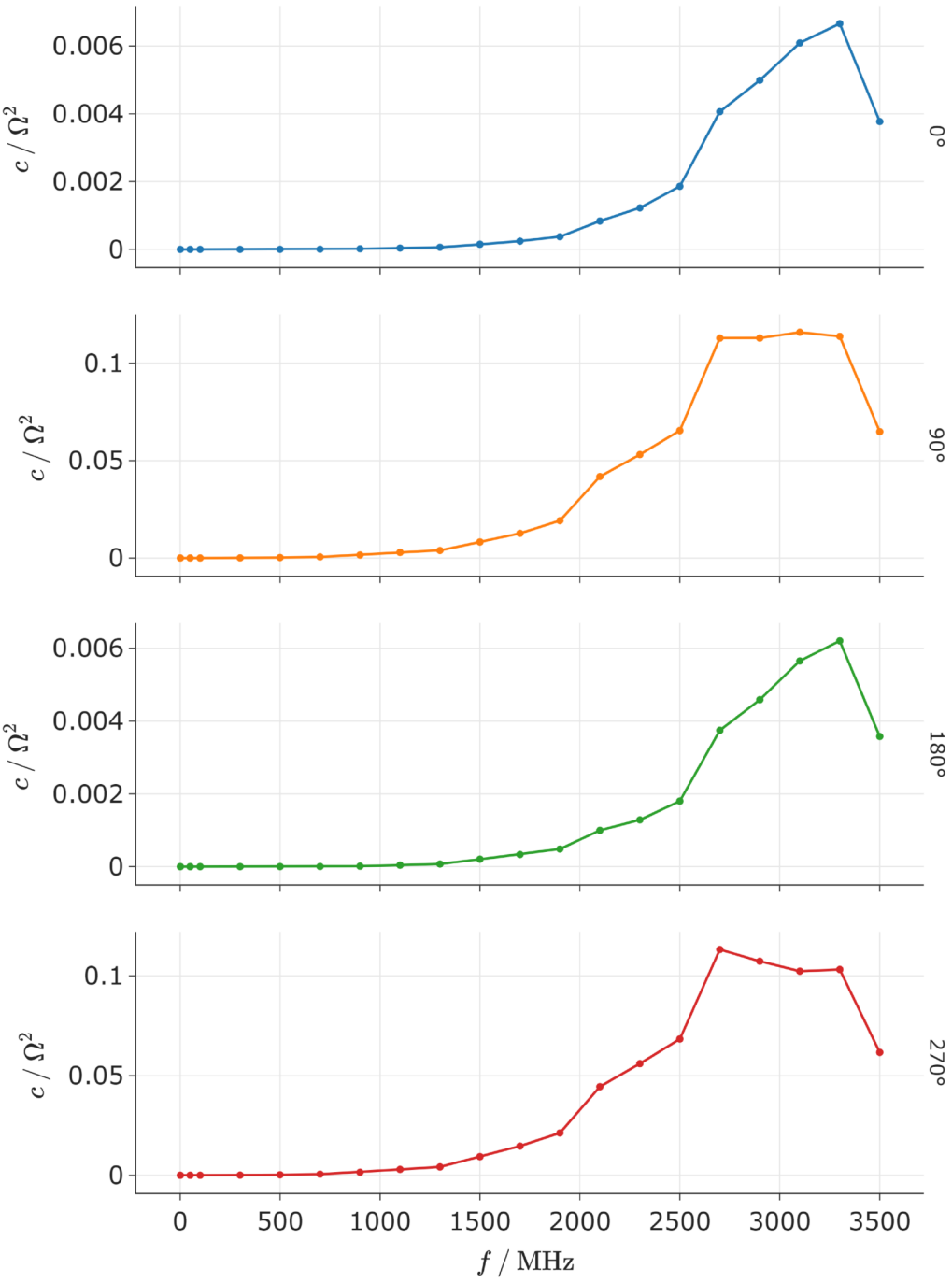


**Figure 5.5:** Coupling coefficients between the measurement system (TEM cell and EMI test receiver) and the bondwire antenna.

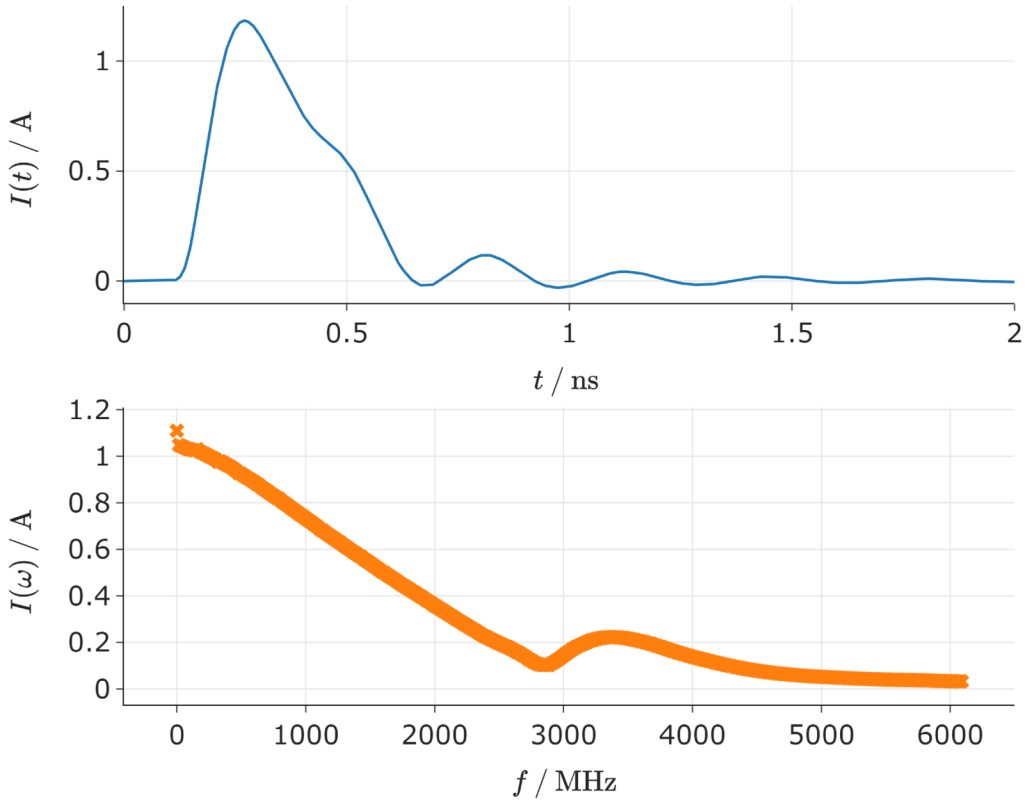


**Figure 5.6:** Fourier analysis of the VCSEL driver current.

to the VCSEL is appearing in it and not in the 90° orientation.

It is apparent that the prediction is not convincing. At the lower frequencies the values are underestimated by approximately 5 dB. At the higher frequencies they do not capture the decrease of the peaks with a local minimum at approximately 1600 MHz and instead increase. Nevertheless, at 700 MHz there is a range in which the predictions align. Naturally, there is also a frequency shift of the peaks, because the device is not operating exactly at the nominal fundamental frequency.

One possible explanation for the substantial deviation could be that the effect of the filters, which are used by the EMI test receiver to get the measurement value at each frequency, was not considered. The test receiver uses a filter with a certain bandwidth which broadens any peak. However, the impact should cancel out since it occurred both in the measurement of the actual sensor EMI and of the bondwire emissions. Another potential error could be coming from the simulations. Both the simulation of the VCSEL current and the bondwire resistance were simplified and thus can deviate from the actual situation.

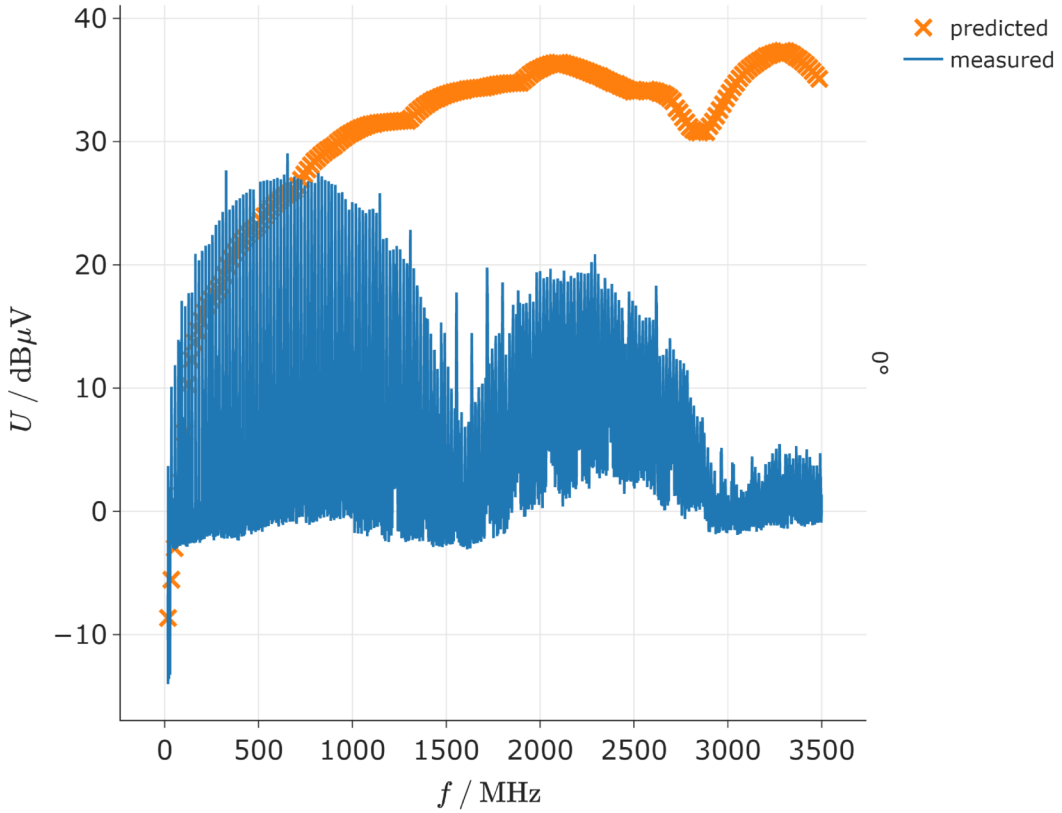


**Figure 5.7:** Comparison of the measured 0° TEM cell spectrum of the TOF sensor and the predicted VCSEL current peaks.

## 5.2 Shielding Hypothesis

The observations made in the TEM cell measurements, the simulation and the bondwire experiment suggest two main conclusions: First, the EMI measured in the TEM cell seems to be very similar to the radiation emitted by a superposition of dipoles in the far field. This is suggested because we saw by jittering the VCSEL current in section 3.6 that only the 0° orientation is affected. Since the radiation caused by the VCSEL current is only measured in this spectrum, it appears that the TEM cell suppresses all fields but the dipole radiation which then is only radiated into the proper direction, i.e. to the connection of coaxial cable, in one orientation. If the equivalent dipole moment of the electric component points there, it is not coupling and thus not measured. This is illustrated in fig. 1.6.

Secondly, we observed that the shielding was highly dependent on the direction and quality of the grounding. This occurred in the TEM cell measurements with the high resistance sensors and the simulation. The TEM cell spectra in the two orientations were reduced differently, because the coated lids are only grounded along the long axis of the sensor. Furthermore, once there was a soldered grounding contact along the short axis in the copper tape configurations, the 0° spectra were shielded enormously.

Combining both observations, it stands to reason that the TEM cell selects the dipoles with the correct direction depending on the orientation of the sensor in it, and that for a well performing shield a current loop with an equivalent dipole moment in the opposing direction must be possible. This mechanism is illustrated in fig. 5.8. That condition was fulfilled in the sensors with the coated lids for the 90° orientation, where subsequently the shielding depended on the grounding quality. In the 0° orientation, no appropriate current loop was possible and only the copper tape configurations with a contact along the short axis improved the situation. If the proper grounding was not available in the given orientation, the shields performed as if they were floating. Hence, the shielding effectiveness of the coated lids in the 0° orientation did not depend on the resistance.

In the simulation, this selection which the TEM cell executes, was included innately in the setup, since only one fixed dipole was used and the direction of its moment was not changed. Therefore, the partially grounded devices showed the exact same finding, i.e. that only the grounding along the long axis showed improved shielding compared to the floating configuration.

Whether the current loop analogy with the appropriate equivalent dipole moment is physically correct was not checked. A current loop would undoubtedly be induced in such a way, that the fields caused by it oppose the driving ones. Hence, EMI could be reduced and the device is shielded. The exact mechanism should be more complex, however, since the shield is larger than the sources and has a different geometry. It is unexpected, therefore, that the opposing field mimic the dipole far field exactly. This, as mentioned in chapter 4, can be investigated there in the simulation, since HFSS is able to compute the currents in the devices.

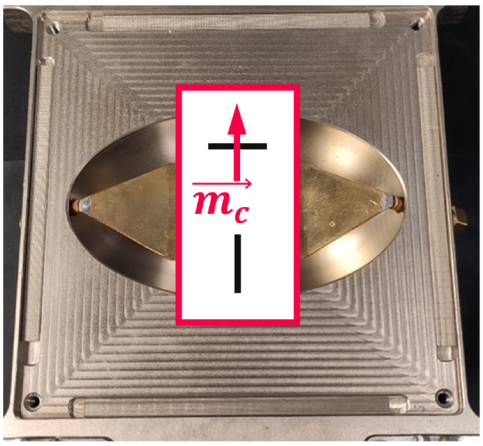


**(a)** TEM cell coupling 0°

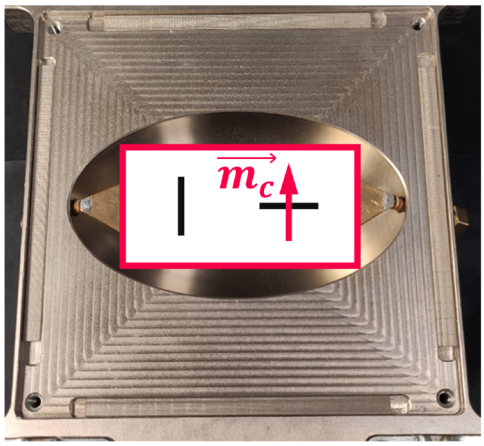


**(b)** TEM cell coupling 90°

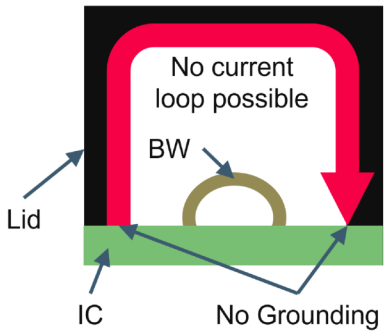


**(c)** Shielding mechanism 0°

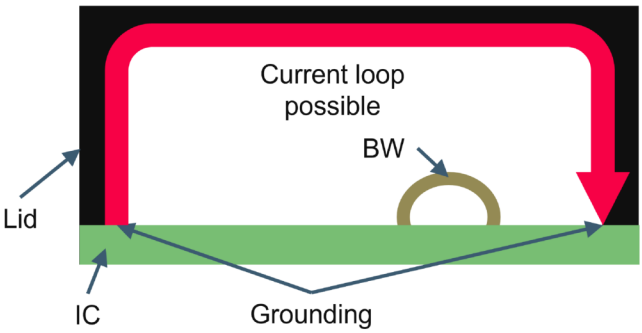


**(d)** Shielding mechanism 90°

**Figure 5.8:** Shielding hypothesis of the TOF sensor with sketched bondwires. (a) and (b): Dipole moments of the bondwires (black lines) that are coupling to the TEM cell. (c) and (d): Cross section of the TOF sensor and shielding mechanism. Due to the directional grounding only one appropriate current loop is possible and only the EMI caused by the bondwire (BW) that is sketched in (d) is shielded effectively. This leads to a disparity in the TEM cell measurements.

Additionally, this conception may be translated to a simplified shield which is only a wire in a loop over the device that is to be shielded. It could be arranged in different planes, e.g. along the short and long axes of the TOF sensor at hand. Based on the observations of the impacts of the grounding made in chapters 3 and 4, it is expected that these configurations mainly affect one orientation in the TEM cell and, hence, mainly shield a subset of the EMI sources.

Pan et al. [12] included also an electronic dipole in the description of the EMI of an arbitrary IC. Thus, it would be interesting to see how an electric dipole can be shielded in this context. Especially, if the grounding has the same impact as on magnetic dipoles with respect to quality and direction.

# Chapter 6

# Transmission Line

By placing a sample between one emitting and one receiving antenna and comparing the strength of the signal to before the insertion, a simple measurement setup for the material characterization with respect to EMI shielding was built. The intent was to extract the shielding capabilities of the coating by eliminating the system influences of the TOF sensor. The same coatings that were defined in chapter 2 and measured in the TEM cell in chapter 3 were investigated here. The 30 mm × 30 mm LCP plates were coated for this purpose. This study was done at and in corporation with the Institute of Electronics at the Graz University of Technology.

## 6.1 Setup

The setup is depicted in fig. 6.1. The emitting and receiving antennas were near field probes mounted on the outside and on the inside of a shielded chamber, respectively. Therefore, there couldn't be transmission of EMR that is not going through the opening. Naturally, there are always seams that allow some EMR to pass through. To reduce this, EMI seals were used onto which the metallic coating was pressed. The LCP sample was fixed with plexiglas that was mounted onto the wall of the chamber below the opening. Then a force was applied by hand which pressed the plates onto the seals. Inside the chamber, an amplifier was joined up in circuit. A spectrum analyzer (Rigol, DSA832) scanned the frequency range and recorded the transmission spectrum in dBm for each coating. It was operated as a network analyzer and therefore immediately showed the desired spectrum.

An uncoated LCP plate was used as reference. Additionally, a copper tape as in fig. 3.11a was measured. Using both measurements as upper and lower bounds respectively, the dynamic range was evaluated, i.e. the measurement values that can be assumed by the system. Below it, the coupling, e.g. through the seams, dominates and only 'noise' is measured. Since the signal cannot be amplified without supplying additional power, there should be no results above it. Because it was assumed that the measurement values quickly reach the lower bounds, only the thinner coatings of each material were used. Fur-

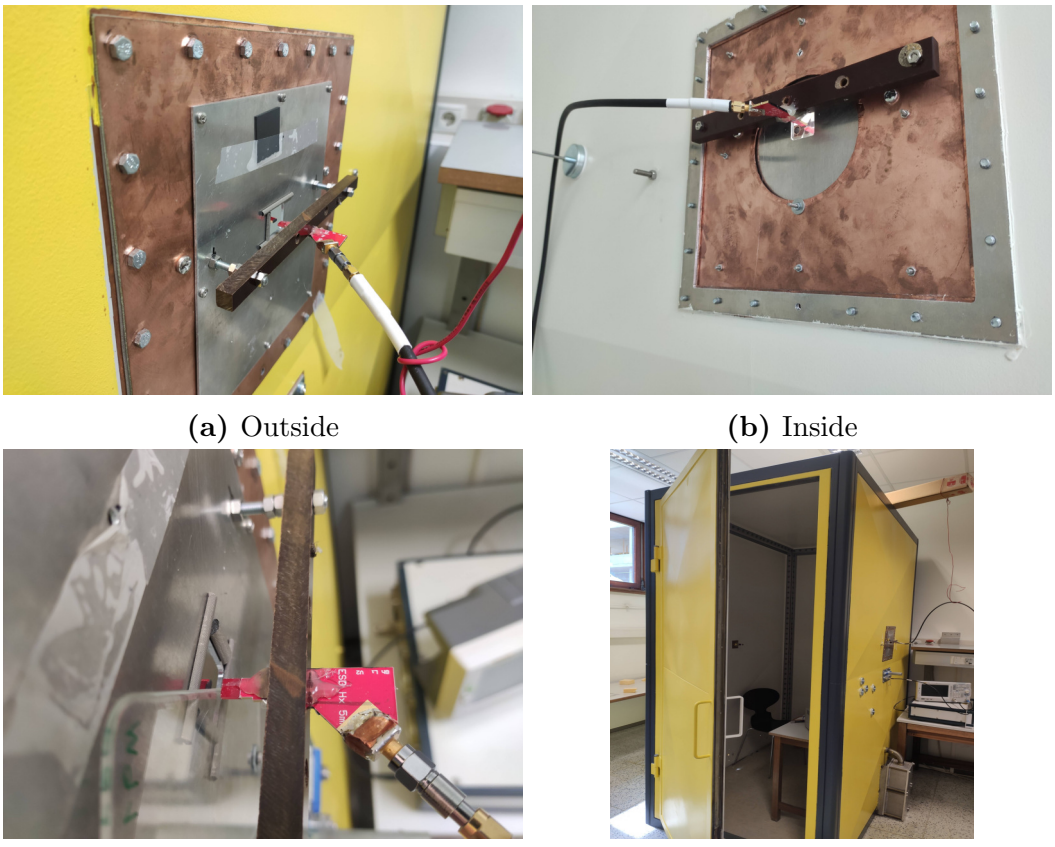

**(a)** Outside **(b)** Inside

**(c)** Probe **(d)** Chamber

**Figure 6.1:** Setup for the transmission line measurements of the coatings' shielding capabilities.

thermore, also a B6x2 sample was tested, which was coated on both sides of the plate with a nominal thickness of 6 µm.

## 6.2 Results

The resulting spectra are depicted in fig. 6.2. Most of the samples reach the lower bounds of the dynamic range, which is represented by the copper tape. We can see that the dynamic range appears to decrease with frequency: While up to 2000 MHz power levels as low as approximately −85 dBm could be measured, that increased to approximately −80 dBm at 3000 MHz. Those values can be mapped to the SE by subtracting the reference spectrum. Furthermore, there is an oscillation in the spectra which is due to multiple reflection in the measurement system, likely inside the chamber.

The sputtered coating is evidently barely shielding, compared to the other ones. The 2nd worst performing ones are B3 and B6, for which the thicker one did not yield a significant increase. B6x2 with a film on both sides of the plate is shielding much better, but has a dip at 1500 MHz to 2100 MHz possibly due to a resonance. However, it is unexpected to occur between both sides of the LCP, because the wavelength is not of the right order: Assuming the real part

of the relative permittivity to be approximately 4, the wavelength at 1800 MHz is 167 mm and the LCP thickness is 1 mm. Hence, it is not clear what causes the dip. Some measurements have a similar dip at the same frequency. Others have one at approximately 1400 MHz. C3 shows a definite improvement over B3, but being inferior to A5. However, that coating is thicker and thus a one-to-one comparison is not possible. The coating which is clearly the best is SGP15, but similarly it is much thicker than the others.

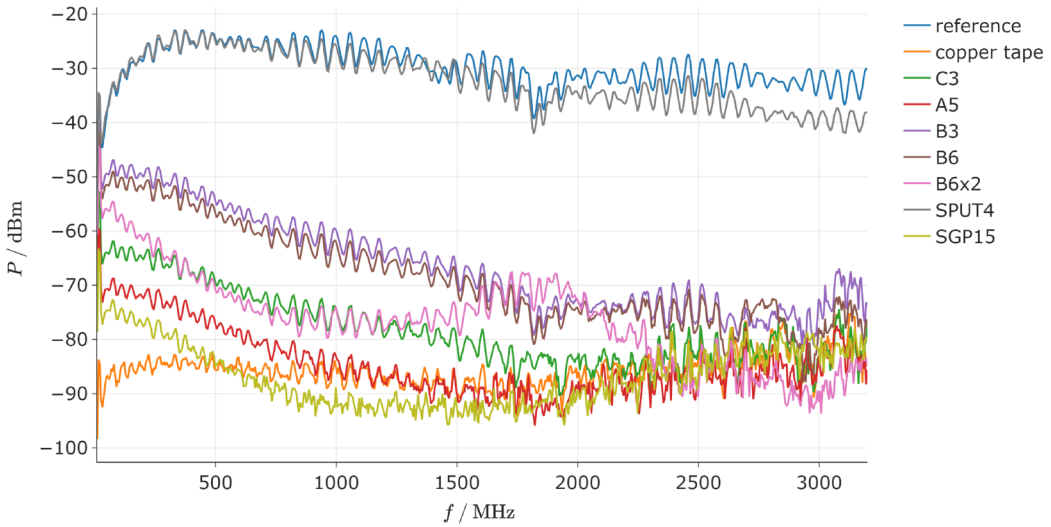


**(a)** Transmission spectrum

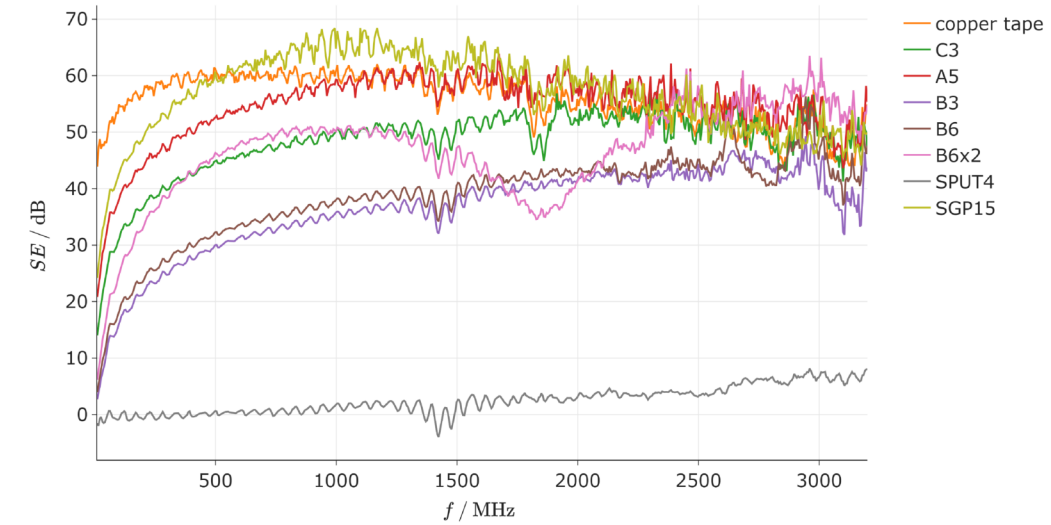


**(b)** SE

**Figure 6.2:** Results of the transmission line measurements of the coating's shielding capabilities. In order to calculate the SE, the reference spectrum was subtracted.

## 6.3 Summary

In summary, we observed that the coating SGP15 performed best and reached a SE above the dynamic range, which we considered to be approximately 60 dB. The second was A5, the third C3 and the coating B performed worst, apart from the sputtered one. The latter showed practically no shielding.

A similar ranking was reached in section 2.2, where we investigated the conductivity of the coatings by measuring the resistance between the two ground pins of the assembled TOF sensor. Unfortunately, coating C was not included there, since no devices with it were yet assembled. Nevertheless, there we observed coating A being slightly better than SGP, but we also recognized that a definite ranking between those was not possible due to outliers in the measurements. All in all, however, these transmission line measurements are a valuable confirmation of the ranking we deduced before and an indication that the conductivity of a material can, in fact, be translated to resulting SE.

However, there are serious flaws in the measurement setup: First, the mechanism with which the sample plates are pressed onto the EMI seals around the opening is too frail, because a force is applied manually. This inevitably varies from measurement to measurement and slight shortfalls of contact pressure shift the spectra several tens of dB, which is unacceptable. Moreover, the opening was too large and the coated plates did not have enough overlap over the seals, possibly creating more gaps. Furthermore, one seal was lost and a shorter one was used out of despair, which resulted in gaps around the opening.

As it is evident, future trials need to improve the setup, which surely will increase precision. Additionally, the thicknesses of the coatings should be adjusted to make the SE comparable. For the SGP coating that means ordering more plates with lower thicknesses, as most of the other deposition processes couldn't produce thicker ones than those already at hand. It is advisable to make two sets of measurements with coating thickness of approx 3 µm and 5 µm to 6 µm respectively.

# Chapter 7

# Conclusion

In this work, different conductive coatings for EMI shielding of a TOF sensor were investigated. For this purpose, outsourced depositions and an internally sputtered one were deposited onto the device's LCP lid and onto plates of the same material. That is documented in chapter 2 and an overview of the coatings is given in table 2.1. The sensor design allows for grounding along the long axis of the sensor. The lid is depicted in fig. 1.1 and the resulting electrical diagram of the coating in fig. 2.3. The frequency range that was considered is 1 MHz to 3500 MHz.

The theory was summarized in chapter 1, where we learned that the conductivity of the coating should be the only relevant material parameter for the shielding performance. A thicker deposition subsequently also lowers the resulting resistance and was advantageous for the experiments.

The sputtering process (section 2.1) encountered many problems due to the strong impact of small variations of the process parameters onto the deposition rate. Nevertheless, lids and plates with a 4 µm thick film were fabricated.
Between the two ground pins of the assembled sensors a resistance can be measured, because the IC's ground is split into two corresponding parts. They are connected by the coating and the conductive adhesive, which glues the lid onto the substrate, in parallel. Thus, the measured total resistance is correlated to the conductivity of the coating material. This was conducted in section 2.2 with a 4-wire resistance measurement setup. In this way, a first ranking of the expected shielding capabilities was achieved. Here, coatings A and SGP had a lower resistance than B and SPUT, where the latter showed practically no improvement compared to the uncoated sensor. C couldn't be measured, since there were no devices assembled yet.
Furthermore, we observed that many devices were not properly grounded and thus their resistance was much larger than that of the uncoated sensors. This can only happen if the conductive adhesive is not properly applied or later removed. Therefore, it is an assembly issue, which introduces a big variance of the resistances, since it cannot ad hoc be distinguished between well and poorly assembled devices.

In chapter 3 the EMI of the TOF sensor was measured in a transverse electromagnetic (TEM) cell, which is a common compliance test for electronic

devices. A EMI test receiver captured the EMI spectra. Naturally, the shielded devices should show lower values. Because there always was a frequency shift even between identical measurements due to the test receiver and an additional one between different devices due to variations of the fundamental frequencies of the electronic components, the shielding effectiveness could not be computed. To retain the frequency information, the envelope of the measurements was visually compared. An objective, overall ranking was extracted via the integral of the spectra.
First, multiple shielding aspects were investigated by manually applying a 35 µm thick copper tape in various configurations on the outside of the lid. It was observed that the grounding is crucial. Furthermore, if the grounding is only along one direction, the spectra of different orientations (of the sensor in the TEM cell) were affected differently. Importantly, devices that were completely enclosed by the copper tape were also compared to ones with cutouts for the apertures. It was found that the open configurations show an increase of the EMI, but a significant shielding is retained. This property is, of course, essential for the feasibility of these coatings for such TOF sensors.
Secondly, the devices with deposited coatings were investigated. It was not possible to unambiguously rank the coatings, that is apart from SPUT which is again not showing a significant improvement over the uncoated lids. It was argued that the grounding design of the sensor is possibly setting a lower limit for the spectra. Hence, that must be improved before a meaningful comparison can be extracted.
Finally, more devices with the SGP coating were studied where also poorly grounded sensors with a high resistance were used. Here, there is a clear differentiation apparent, but only in the 90° spectra. The EMI in these was even amplified by the poorly grounded shield and only the properly grounded ones showed shielding. That was not the case in the 0° orientation, where no correlation with grounding was found and all devices shielded approximately equally.

A simulation was conducted in chapter 4 with Ansys HFSS, which aimed to replicate the study with the copper tape. As source, a single, harmonic, magnetic dipole was used. Around it the lid is modeled in a much simplified way. On its outside a 35 µm thick copper film was added in similar configurations as before. On the bottom there is a copper sheet of the same thickness which emulates the ground planes in the IC. For the evaluation, the magnitude of the Poynting vector was averaged over a sphere with a radius of 15 mm. A spectrum was then built by repeating that for multiple frequencies in the range set above. This time, the shielding effectiveness could be calculated according to eq. (1.38) by always using the sensor without the copper shield as reference. It is plotted in fig. 4.3. Again, the completely enclosed sensor was shielded best and the open, but completely grounded one was second. Another important finding is that configurations which have a partial grounding are either almost as effective as the completely grounded one, or as bad as the completely floating one. This is likely due to the combination of a directional source (a magnetic dipole with a fixed dipole moment vector) and a directional grounding of the shield.

In chapter 1 we also recognized that the shielding takes place in the near field. Unfortunately, this makes the theoretical calculation of the fields impossible. By extension, also the measurements in the TEM cell should be in the near field. However, we discussed in chapter 5 that the theory developed by Wilson [21] and Pan et al. [12] is an interesting prospect. Pan et al. modeled the complete IC as three dipoles in the far field. By treating it in the far field the theoretical situation is immensely simplified. This approximation can be justified by the geometry of the TEM cell. As the name suggests, it is built in a way that only allows TEM modes to build up to a significant magnitude. Those are inherently far field. They also propose a method with a hybrid that enables one to extract the dipole moments from TEM cell measurements. Hence, the fields in the TEM cell could now be calculated easier. Because of the complex geometry, however, a further investigation is necessary to determine the feasibility of this theoretical description. Yet, it is still expected that the shielding takes place in the near field. Further, it could be investigated via the simulation whether there are indeed only far field dipole modes present inside the TEM cell.

The coated LCP plates were measured in a transmission line setup with a network analyzer in chapter 6. This approach eliminates all the system influences of the complete sensor where numerous currents cause EMI that superposes. This was conducted at the Institute of Electronics of the Graz University of Technology. One emitting and one receiving near field probe were connected to the network analyzer. A metal chamber was shielding as much radiation from coupling as possible and only the opening onto which the samples were placed allowed for transmission. These spectra were again compared and the shielding effectiveness was evaluated by referring them to the uncoated plate. The result is depicted in fig. 6.2. Just as before, the coatings SGP and A performed best. However, the different thicknesses of the coatings made a one-to-one comparison impractical. But the general trend to all the other experiments was confirmed. Also, the sputtered coating shielded the least amount of EMI. Here the coating C3 was available and it performed as good as the coating B6, with only half the thickness.

It is, naturally, vital to confirm the linearity and superposition of the TEM cell measurement system. This was conducted by using a single bondwire as EMR source. It was driven by a signal generator at one harmonic frequency at a time and the resulting spectra was recorded. By repetition the frequency range was scanned. In order to compute coupling coefficients, the current through the bondwire was calculated and related to the measured voltage. They are plotted in fig. 5.5. It was observed that no additional frequencies appear. The linearity of the system, unfortunately, was not tested in the scope of this thesis. This could be done by modifying the output power of the signal generator.
With the coupling coefficients available, a prediction for the measured EMI caused by the VCSEL current was computed. The necessary frequency components were computed via a FFT of a simulation of the current. Multiplying them with the coefficients of the bondwire yielded the spectrum depicted in fig. 5.7. However, it does not agree satisfyingly with the real spectrum of the

TOF sensor, indicating that either the underlying assumptions or the used resources were incorrect.

A shielding model was developed in section 5.2 by combining the observations made in all experiments. First, it was argued that the EMI sources in the IC act like three dipoles in the far field as described by Pan et al. [12]. The TEM cell then selects the dipoles which radiate towards the connectors and the coaxial cable (see section 1.2.6). Hence, the dipole sources are only appearing in one orientation. This is consistent with the bondwire experiment, which had vastly different coupling coefficients for the orientations with a factor larger than 17 between them.
Secondly, it was hypothesized that for good shielding to occur a closed current loop through the shield must be possible whose equivalent dipole moment is in the same direction as that of the source (so far, only magnetic dipoles where considered). This reasoning agrees with the measurements in the TEM cell with the copper tape, where only the appropriate grounding which enabled the closed loop showed significant shielding. Furthermore, the sensors with different grounding quality (resistance) exhibited different shielding only in the 90° orientation. The simulation also agrees, since there a fixed magnetic dipole was used as source and thus only one grounding direction was effective while the other performed as if it was floating. There, also the near field was considered. The hypothesis for the shielding mechanism is illustrated in fig. 5.8.

## 7.1 Outlook

In this section, a possible continuation of valuable experiments is proposed. Sensors shielded with coating C weren't yet available. Hence, it should be measured and included in the shielding evaluation in the TEM cell. Furthermore, it would be ideal to standardize the coating thicknesses to make them easier comparable. There will always be a variation due to the coating process, but that can be kept in the ranking to assess the combination of material and process.

Most importantly, the grounding design must be adapted. It should be grounded on as many places as possible in a reliable way. It would be also worthwhile to investigate possible improvements regarding the conductive adhesive. At least its deposition must be made more reliable. Subsequently, the evaluation in the TEM cell should be repeated. It is expected that with the better grounding it will be able to reach lower EMI levels which then allow to rank the materials.

The simulation, too, offers the possibility to investigate a host of configurations. It would be interesting to model the shield on the inside of the lid with a lower thickness, such that it is more comparable to the coated lids. Other sources can be simulated. Especially, the same set as in [12] should be evaluated, i.e. one more magnetic dipole and one electric dipole whose moment is perpendicular to the ground plane.
Above, it was mentioned that the simulation allows to look at the fields. Hence,

it could be checked if inside the TEM cell there are indeed only TEM modes and dipole radiation in the far field. Naturally, for this the whole TEM cell with the coaxial cable needs to be modeled. The cable should be included, because it could be that they will filter out other modes and in the TEM cell there is not as much of a selection.
It must also be confirmed if the shielding hypothesis with the current loop captures the right physics, i.e. whether there is, first, a closed current loop in the shield, and secondly, an opposing equivalent dipole in the far field.

Furthermore, a simplified shield that is only a wire in a loop over the device could be tested. It can be assumed, based on the observation that a directional grounding shields just a subset of appropriately oriented sources, that this attenuates only one of the TEM cell spectra. With this design, devices, where neither a bent sheet nor a coated lid are applicable, could be shielded.

# Appendix A

# Definitions

## A.1 Fourier Transform

### A.1.1 Continuous Fourier Transform

For evaluating the D-field for dispersive materials the following definition of the Fourier Transform and its inverse was used:

$$\boldsymbol{D}(\boldsymbol{r},\omega) \coloneqq (\mathcal{F}\boldsymbol{D})(\boldsymbol{r},\omega) = \int_{-\infty}^{\infty} \boldsymbol{D}(\boldsymbol{r},t) e^{-\mathrm{i}\omega t} dt \tag{A.1a}$$

$$\boldsymbol{D}(\boldsymbol{r},t) \coloneqq \left(\mathcal{F}^{-1}\mathcal{F}\boldsymbol{D}\right)(\boldsymbol{r},t) = \frac{1}{2\pi}\int_{-\infty}^{\infty} \boldsymbol{D}(\boldsymbol{r},\omega) e^{\mathrm{i}\omega t} dt \tag{A.1b}$$

Inserting the definition of D eq. (1.9) yields

$$\begin{aligned}
\boldsymbol{D}(\boldsymbol{r},\omega) &\coloneqq \int_{-\infty}^{\infty}\int_{-\infty}^{t} \epsilon(t-t')\boldsymbol{E}(\boldsymbol{r},t') e^{-\mathrm{i}\omega t} dt' dt \\
&= \int_{-\infty}^{\infty}\int_{-\infty}^{\infty} \epsilon(t-t') e^{-\mathrm{i}\omega(t-t')} \boldsymbol{E}(\boldsymbol{r},t') e^{-\mathrm{i}\omega t'} dt' dt \\
&= \int_{-\infty}^{\infty}\int_{-\infty}^{\infty} \epsilon(t-t') e^{-\mathrm{i}\omega(t-t')} \boldsymbol{E}(\boldsymbol{r},t') e^{-\mathrm{i}\omega t'} dt' dt \\
&= \int_{-\infty}^{\infty}\int_{-\infty}^{\infty} \epsilon(t'') e^{-\mathrm{i}\omega t''} \boldsymbol{E}(\boldsymbol{r},t') e^{-\mathrm{i}\omega t'} dt' dt'' \\
&= \int_{-\infty}^{\infty} \epsilon(t'') e^{-\mathrm{i}\omega t''} dt'' \int_{-\infty}^{\infty} \boldsymbol{E}(\boldsymbol{r},t') e^{-\mathrm{i}\omega t'} dt' \\
&= \epsilon(\omega)\boldsymbol{E}(\boldsymbol{r},\omega)
\end{aligned} \tag{A.2}$$

where in the second line the integration limits may be extended, since $\epsilon(t)$ is 0 for negative arguments. That is because future events do not contribute.

### A.1.2 Discrete Fourier Transform

For computing the frequency components $y$ of the VCSEL current which was initially given as a sequence of numbers $x$ for each time step the following

definition of the discrete Fourier transform and its inverse was used:

$$y[k] = \frac{1}{\sqrt{N}} \sum_{n=0}^{N-1} e^{-2\pi \mathrm{i} \frac{kn}{N}} x[n] \tag{A.3a}$$

$$x[n] = \frac{1}{\sqrt{N}} \sum_{k=0}^{N-1} e^{2\pi \mathrm{i} \frac{kn}{N}} y[k] \tag{A.3b}$$

# Appendix B

# Cross Sections

The cross sections were conducted by fixing the samples inside a cylindrical mold. Epoxy resin was poured over them in order to facilitate grinding without deterioration of the coating. Cross sections of the lids were made on a disc sanding machine with progressively increasing granularity of the paper and finally observed in an optical microscope. The coatings are defined in chapter 2.

## B.1 Lids and Plates

The LCP lids and plates of the TOF sensors were sanded before assembly in order to determine the thickness of their coatings. A statistical evaluation of the coatings A, SGP and SPUT was conducted by measuring the thickness on the lid at its different surfaces multiple times in the microscope images. The results are listed in table B.1.

**Table B.1:** Coating thickness of the LCP lids of the TOF sensor determined by mechanical cross-sectioning.

| Coating | Bottom / µm | Left / µm | Right / µm | Top / µm |
|---|---|---|---|---|
| A5 | $6 \pm 2$ | $3 \pm 2$ | $2.4 \pm 0.8$ | |
| A10 | $5 \pm 3$ | $5 \pm 3$ | $3 \pm 2$ | $10 \pm 2$ |
| SGP15 | $16 \pm 3$ | $4 \pm 3$ | $20 \pm 30$ | $22 \pm 4$ |
| SPUT4 | $3.1 \pm 0.7$ | $1.6 \pm 0.7$ | $1.6 \pm 0.3$ | $3.9 \pm 0.3$ |

It is evident, that there is a huge discrepancy between the thickness on sidewalls and the other two surfaces. Therefore, the nominal thicknesses of the manufacturers cannot be interpreted in the straight forward way, but a more detailed consideration is necessary. The sputtered coating has the smallest spread, and thus a good quality deposition was fabricated, be it thin.

It is important to note, however, that also the measurement process is not optimal. By setting the lines between which the thickness is then determined slightly different, the value is affected significantly. That is because the magnification in the optical microscope is barely sufficient.

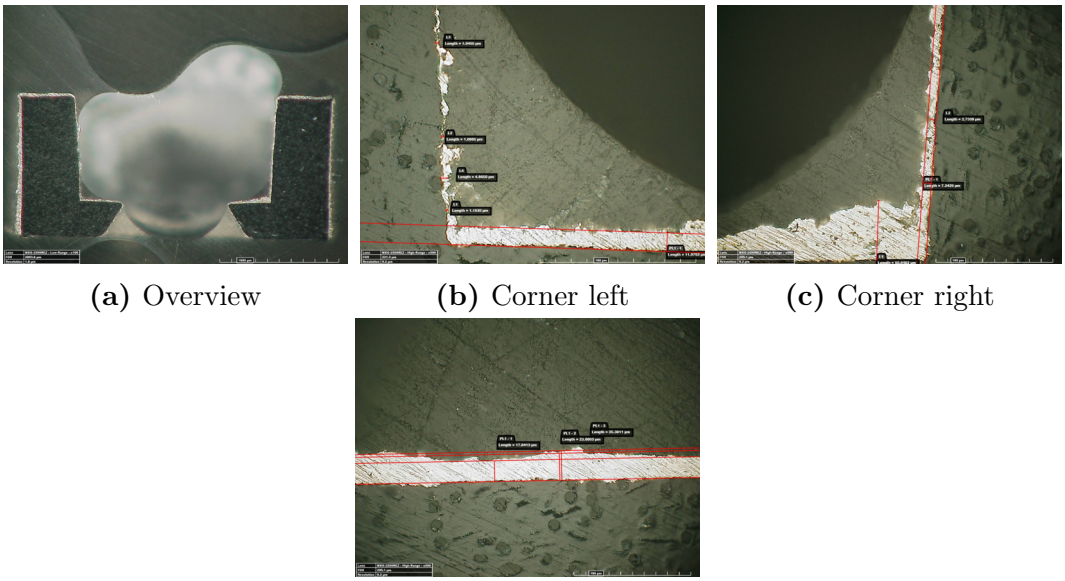

**(a)** Overview **(b)** Corner left **(c)** Corner right

**(d)** Top left

**Figure B.1:** Mechanical cross section of the LCP lid of the TOF sensor coated with SGP15. Nominal thickness: 15 µm.

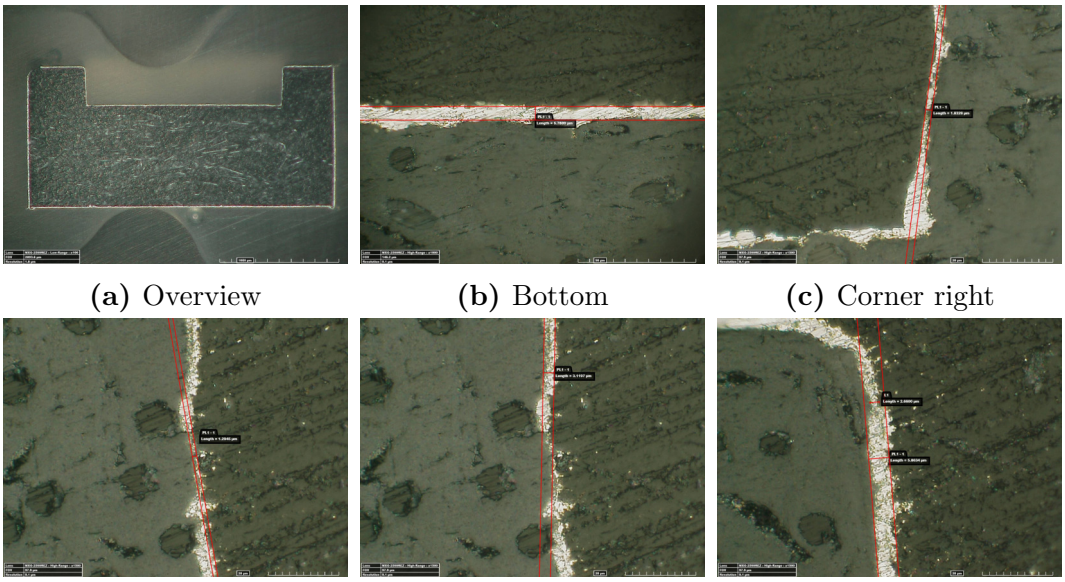

**(a)** Overview **(b)** Bottom **(c)** Corner right

**(d)** Left 1 **(e)** Left 2 **(f)** Left 3

**Figure B.2:** Mechanical cross section of the LCP lid of the TOF sensor coated with A5. Nominal thickness: 5 µm.

**(a)** Bottom 1 **(b)** Bottom 2 **(c)** Left 1

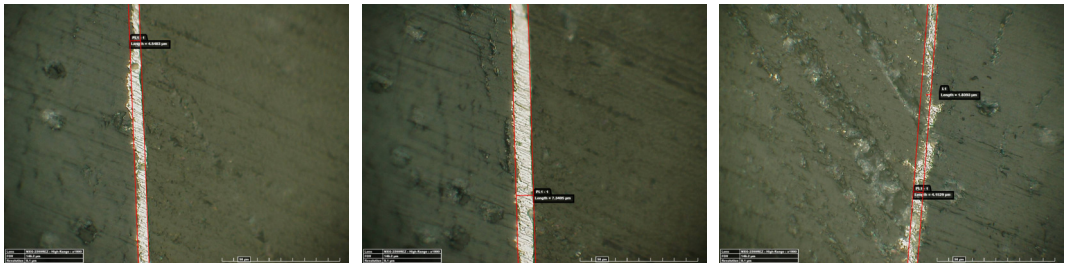

**(d)** Left 2 **(e)** Left 3 **(f)** Right

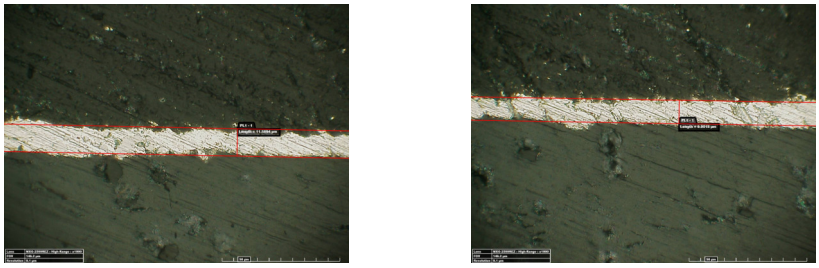

**(g)** Top left **(h)** Top right

**Figure B.3:** Mechanical cross section of the LCP lid of the TOF sensor coated with A10. Nominal thickness: 10 µm.

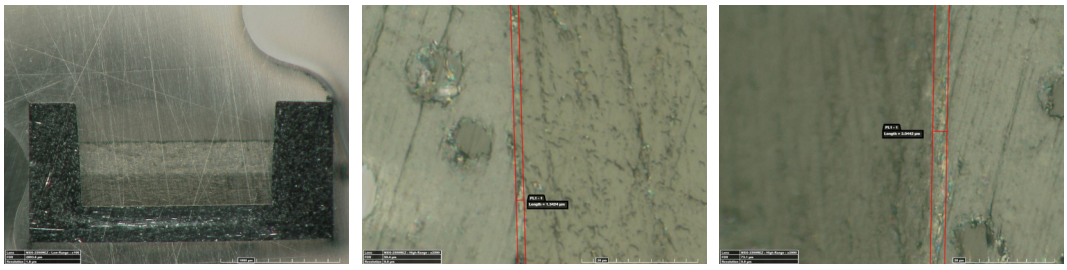

**(a)** Overview **(b)** Left flank **(c)** Right flank

**(d)** Left corner **(e)** Bottom **(f)** Right corner

**Figure B.4:** Mechanical cross section of the sputtered LCP lid of the TOF sensor (SPUT4). Coating: Sputtered Pt-Pd. Nominal thickness: 4 µm.

## B.2 Assembled Devices

The assembled devices were also cross-sectioned in order to investigate why the sensors have such different resistances between their ground pins. That evaluation was conducted in section 2.2. We saw an increase in resistance for some devices, which must be an assembly related issue that effects the conductive adhesive which electrically connects the coated lids to the two ground pins, but simultaneously "shorts" them.

The devices listed in table B.2 were chosen for this study. The cross sections are imaged in fig. B.5. For the uncoated sensors one with a rather high resistance was investigated. It shows a gap between the coating and the right pad, but because of the order of its resistance, it is likely that there is an electrical connection in another plane. SGP15-0A4 has one of the lowest resistance of all devices and shows a good connection at the two pads. The other two devices have a gap over the left pad, into which the epoxy material used for the cross-sectioning poured. Hence, it is clear that the coating is not grounded and the parallel resistance due to it cannot impact the total resistance. However, it is not that obvious why the parallel resistance of the conductive adhesive is increased. Likely, it was simply spread unevenly during the assembly and missed the pad. Then the two pins would not be connected at all and it would be an open circuit causing the huge resistance.

**Table B.2:** Evaluation of the cross sections of the assembled TOF sensors.

| Coating | Device | Resistance / Ω | Observation |
|---|---|---|---|
| U | 015 | 1.6 | Small gap over the right pad. Possibly a connection in another plane. |
| SGP15 | 0A4 | 0.08 | Good connection |
| SGP15 | 0FF | 4.14 | Large gap over the left pad. |
| SGP15 | 0DP | 1096000 | Large gap over the left pad. |

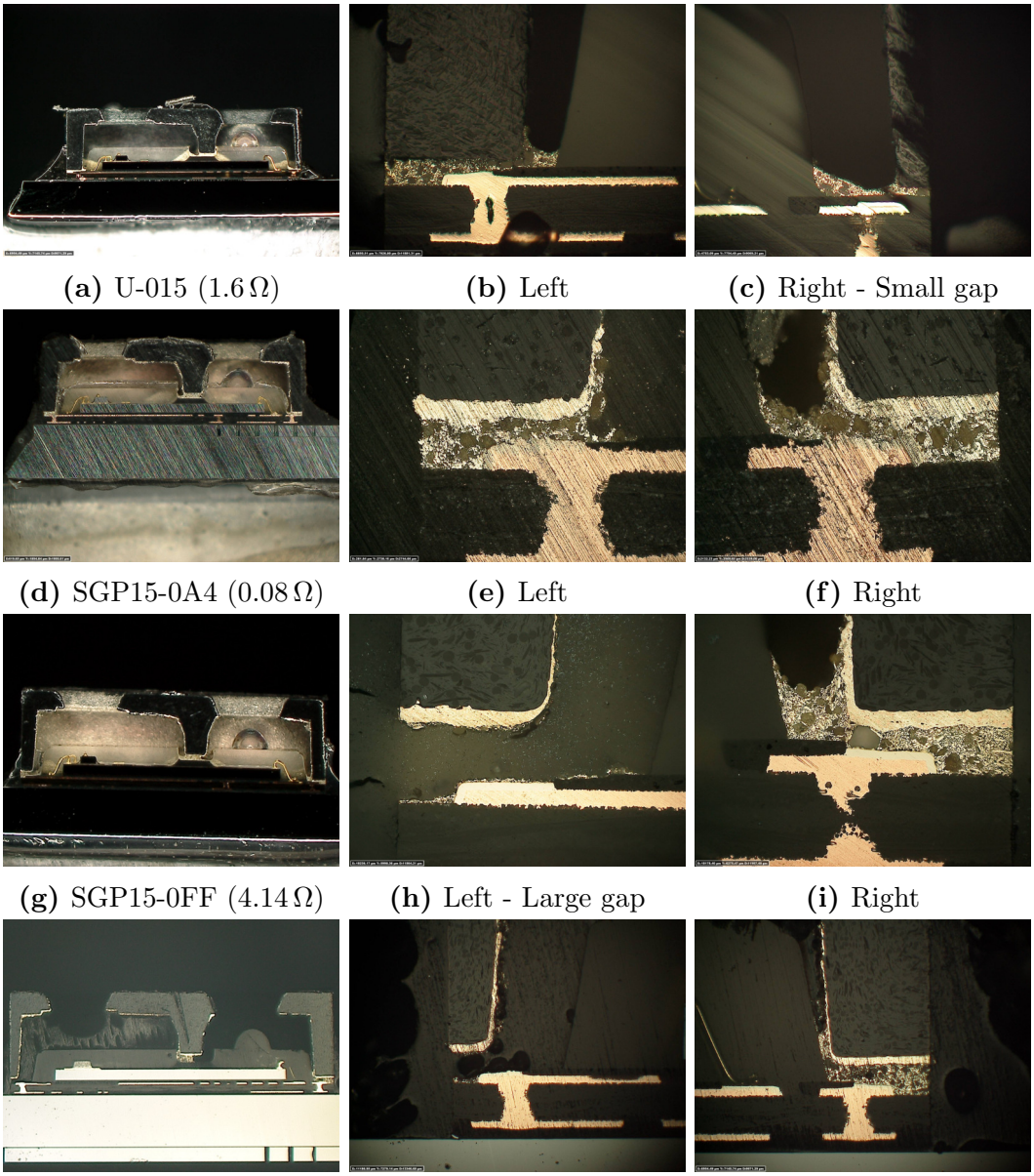

**(a)** U-015 (1.6 Ω) **(b)** Left **(c)** Right - Small gap

**(d)** SGP15-0A4 (0.08 Ω) **(e)** Left **(f)** Right

**(g)** SGP15-0FF (4.14 Ω) **(h)** Left - Large gap **(i)** Right

**(j)** SGP15-0DP (1.096 MΩ) **(k)** Left - Large gap **(l)** Right

**Figure B.5:** Mechanical cross section of the assembled TOF sensors.

# Appendix C

# Software

## C.1 ALS Algorithm

This asymmetric least squares algorithm developed in [2] and its optimized version taken from [15] allow to fit the baseline of spectra with the parameters `lam, p, n_iter` which are the smoothing length, the precision and the maximum number of iterations respectively. Note that convergence is not guaranteed in this implementation. In this thesis, the default parameters `lam=1e6, p=1e-5, n_iter=50` are used to compute the envelope of the peaks.

```
import numpy as np
from scipy import sparse
from scipy.sparse.linalg import spsolve

def baseline_als_opt(y, lam, p, n_iter=10):
    L = len(y)
    D = sparse.diags([1, -2, 1], [0, -1, -2],
            shape=(L, L - 2))
    D = lam * D.dot(D.transpose())
    w = np.ones(L)
    W = sparse.spdiags(w, 0, L, L)
    for i in np.arange(n_iter):
        W.setdiag(w)
        Z = W + D
        z = spsolve(Z, w * y)
        w = p * (y > z) + (1 - p) * (y < z)
    return z
```

# Bibliography


[1] Henk F. Arnoldus and Matthew J. Berg. "Energy transport in the near field of an electric dipole near a layer of material". In: *Journal of Modern Optics* 62.3 (2015), pp. 218–228. DOI: 10.1080/09500340.2014.971896. eprint: https://doi.org/10.1080/09500340.2014.971896. URL: https://doi.org/10.1080/09500340.2014.971896.

[2] Hans Boelens, Paul Eilers, and Thomas Hankemeier. "Sign Constraints Improve the Detection of Differences between Complex Spectral Data Sets: LC-IR As an Example". In: *Analytical chemistry* 77 (Jan. 2006), pp. 7998–8007. DOI: 10.1021/ac051370e.

[3] International Electrotechnical Committee. "INTEGRATED CIRCUITS - MEASUREMENT OF ELECTROMAGNETIC EMISSIONS, 150 KHZ TO 1 GHZ - PART 2: MEASUREMENT OF RADIATED EMISSIONS - TEM CELL AND WIDEBAND TEM CELL METHOD". In: IEC 61967-2 (Sept. 2005).

[4] Romain Dezert. "Theoretical study of isotropic Huygens particles for metasurfaces". PhD thesis. Dec. 2019.

[5] Alessandro Fedeli, Claudio Montecucco, and Gian Luigi Gragnani. "Open-Source Software for Electromagnetic Scattering Simulation: The Case of Antenna Design". In: *Electronics* 8.12 (2019). ISSN: 2079-9292. DOI: 10.3390/electronics8121506. URL: https://www.mdpi.com/2079-9292/8/12/1506.

[6] David J Griffiths. *Introduction to electrodynamics*. eng. 3. ed., internat. ed.. 2008. ISBN: 0139199608.

[7] Idza Riati Ibrahim et al. "A Study on Microwave Absorption Properties of Carbon Black and Ni0.6Zn0.4Fe2O4 Nanocomposites by Tuning the Matching-Absorbing Layer Structures". In: *Scientific Reports* 10.1 (2020), p. 3135. ISSN: 2045-2322. DOI: 10.1038/s41598-020-60107-1. URL: https://doi.org/10.1038/s41598-020-60107-1.

[8] Aamir Iqbal, Pradeep Sambyal, and Chong Min Koo. "2D MXenes for Electromagnetic Shielding: A Review". In: *Advanced Functional Materials* 30.47 (2020), p. 2000883. DOI: https://doi.org/10.1002/adfm.202000883. eprint: https://onlinelibrary.wiley.com/doi/pdf/10.1002/adfm.202000883. URL: https://onlinelibrary.wiley.com/doi/abs/10.1002/adfm.202000883.

[9] Matthias Keller. *Comparison of Time Domain Scans and Stepped Frequency Scans in EMI Test Receivers*. 2013.

[10] Phalguni Mathur and Sujith Raman. "Electromagnetic Interference (EMI): Measurement and Reduction Techniques". In: *Journal of Electronic Materials* 49.5 (2020), pp. 2975–2998. ISSN: 1543-186X. DOI: 10.1007/s11664-020-07979-1. URL: https://doi.org/10.1007/s11664-020-07979-1.

[11] S.J. Orfanidis. *Electromagnetic Waves and Antennas*. Sophocles J. Orfanidis, 2016. URL: https://books.google.at/books?id=4n5ezQEACAAJ.

[12] Siming Pan et al. "An equivalent three-dipole model for IC radiated emissions based on TEM cell measurements". In: *2010 IEEE International Symposium on Electromagnetic Compatibility*. 2010, pp. 652–656. DOI: 10.1109/ISEMC.2010.5711354.

[13] International Special Committee on Radio Interference. "CISPR 16-1-1". In: (June 2014).

[14] Levent Sevgi. "Electromagnetic Modeling and Simulation". In: *ICCEM 2015 - 2015 IEEE International Conference on Computational Electromagnetics* (Mar. 2015), pp. 13–15. DOI: 10.1109/COMPEM.2015.7052538.

[15] *Stackoverflow - Python baseline correction library*. 2019. URL: https://stackoverflow.com/questions/29156532/python-baseline-correction-library.

[16] Changyi Su, Haixin Ke, and Todd Hubing. "Overview of electromagnetic modeling software". In: *Proc. of the 25th International Review of Progress in Applied Computational Electromagnetics*. 2009, pp. 736–741.

[17] Dimuthu Wanasinghe and Farhad Aslani. "A review on recent advancement of electromagnetic interference shielding novel metallic materials and processes". In: *Composites Part B: Engineering* 176 (2019), p. 107207. ISSN: 1359-8368. DOI: https://doi.org/10.1016/j.compositesb.2019.107207. URL: http://www.sciencedirect.com/science/article/pii/S1359836819312569.

[18] Craig Warren et al. "Comparison of time-domain finite-difference, finite-integration, and integral-equation methods for dipole radiation in half-space environments". In: *Progress In Electromagnetics Research M* 57 (Jan. 2017), pp. 175–183. DOI: 10.2528/PIERM17021602.

[19] Atom O. Watanabe et al. "Multilayered Electromagnetic Interference Shielding Structures for Suppressing Magnetic Field Coupling". In: *Journal of Electronic Materials* 47.9 (2018), pp. 5243–5250. ISSN: 1543-186X. DOI: 10.1007/s11664-018-6387-2. URL: https://doi.org/10.1007/s11664-018-6387-2.

[20] Tim Williams. *EMC for Product Designers (Fifth Edition)*. Fifth Edition. Newnes, 2017. ISBN: 978-0-08-101016-7. DOI: https://doi.org/10.1016/B978-0-08-101016-7.50018-3. URL: http://www.sciencedirect.com/science/article/pii/B9780081010167500183.

[21] P. Wilson. "On correlating TEM cell and OATS emission measurements". In: *IEEE Transactions on Electromagnetic Compatibility* 37.1 (1995), pp. 1–16. DOI: 10.1109/15.350235.

[22] Sergey Yuferev. *Surface Impedance Boundary Conditions: A Comprehensive Approach*. Sept. 2009. ISBN: 9781315219929. DOI: 10.1201/9781315219929.

[23] Zhimin Zhang, Shan Chen, and Yi-Zeng Liang. "Baseline correction using adaptive iteratively reweighted penalized least squares". In: *The Analyst* 135 (May 2010), pp. 1138–46. DOI: 10.1039/b922045c.